CENTRO DE INVESTIGACIONES EN ÓPTICA A.C.

Spectroscopic Characterization of Yb³⁺ doped Barium Zirconate

THESIS SUBMITTED IN PARTIAL FULFILLMENT OF THE
REQUIREMENTS FOR THE DEGREE OF MASTER IN SCIENCE
(OPTICS) AT CENTRO DE INVESTIGACIONES EN OPTICA

I.F. JORGE ROBERTO OLIVA UC

For the Degree of

Master in Science (Optics)

Advised by

Dr. Luis Armando Diaz Torres

And

Dr. Elder De la Rosa Cruz

León Guanajuato, México

May 2008

Research Advisor:

Dr. Luis Armando Díaz-Torres

(DEPARTMENT OF PHOTONICS, CIO)

Dr. Elder de la Rosa Cruz

(DEPARTMENT OF PHOTONICS, CIO)

Reviewers:

Dr. Marco Antonio Meneses Nava

(DEPARTMENT OF PHOTONICS, CIO)

Dr. Pedro Salas Castillo

(CFATA, Universidad Nacional Autónoma de México)

Acknowledges

Abstract

We present our research on visible upconversion luminescence in Yb^{3+} doped Barium Zirconate ($BaZrO_3$, BZO) under NIR excitation. Barium Zirconate was synthesized by hydrothermal method. The visible luminescence is attributed to both, Yb^{3+} cooperative emission and rare earth impurity upconversion emissions. Since the presence of Tm^{3+} and Er^{3+} impurities was not detected by absorption spectra, it has to be very low concentration. The strong intensity of all peaks is interesting considering the very small concentration. This fact suggests very efficient upconversion processes involving traces of Tm^{3+} and Er^{3+} ions having the Yb^{3+} ions as sensitizers. The emission band centered at 504 nm is twice the energy of the normal luminescence of a single ion, suggesting that it is the result of the radiative relaxation of an excited Yb^{3+}-Yb^{3+} pair. For all Yb^{3+} concentrations, the lifetime for the Yb^{3+} cooperative emission is nearly half of the lifetime of single Yb^{3+} ion emission, suggesting the upconversion mechanisms are two photon uponversion processes. FTIR Spectra was recorded to indentify hydroxil groups, residual H_2O and ionic bonds for the cubic crystalline structure of BZO.

In addition, we present the thermodarkening effect in 0.5 at% Yb^{3+}:$BaZrO_3$ microcrystal (an increase of the UV-VIS edge band with annealing temperature). Both, the cooperative up-conversion emission under NIR excitation and fluorescence lifetimes of cooperative emission, increase with annealing temperature. Under UV and VIS excitation no emission of Yb^{2+} ions could be observed. This suggests that the broad band absorption in the UV-VIS region that increase with annealing temperature might be related to F color centers and oxygen vacancies which are responsible for the inhibition of the Yb^{2+} ion emission.

Contents

Chapter 1: A General Overview

Chapter 2: Synthesis, Structure and Morphology of BaZrO$_3$:Yb^{3+} Microcrystals

Chapter 3: Optical Spectroscopy

Chapter 4: Annealing Effect

Chapter 1: A General Overview

1.1. Introduction

There is a continuous technological interest in the design of efficient and durable luminescent materials. The range of applications is extremely broad. Such materials are required in various lightning and display devices (fluorescent lamps, cathode-ray tubes, plasma display cells) as well as other photonic devices (light emitters, amplifiers, and lasers), and detectors (X-ray screens, scintillators) [1,2]. Prospective applications also include fluorescence-based chemical sensors. Most luminescent materials presently in use are based on the emission of some intentionally incorporated impurities. Impurity activation of transparent crystalline materials is a powerful method for designing phosphors for specific needs. Transition metals and rare earths are two broad classes of impurities that have found widespread use. In this thesis we confine our attention to Rare Earths. Rare earth based luminescent materials are being continually developed for a range of applications including lasers [3], displays [2,4,5], scintillators, etc. As specific examples of widely used rare earth phosphors, one could mention $Y_2O_2S:Eu^{3+}$ that is the common red phosphor in cathode ray tubes [6], $Gd_2O_2S:Tb^{3+}$ is used in X-ray intensifying screens [6], $Y_2O_3:Eu^{3+}$ is responsible for the red emission component in fluorescent lamps and plasma display panels [6], Er^{3+}-doped silica fiber amplifiers are used in optical communication [6], Nd^{3+}: YAG has become a very popular laser host [1]. The two basic requirements for any phosphor material are the high luminescence yield and long-term stability [6].

From the point of view of luminescence applications in visible and UV spectral ranges, wide band gap materials are attractive hosts for optical activation with impurities (like rare earths). In these materials the impurity can emit within the optical window of the host material. Wide-gap materials are also attractive for applications under UV, VUV, or X-ray excitation. Within the wide-gap materials our major attention has been focused on $BaZrO_3$ (BZO) perovskite since it is generally less sensitive to oxygen surface contamination and also the preparation route of the material is relatively simple [6]. And other

important reason is that it has been the subject of current research of the Spectroscopy and Photonics Material Group here at the Centro de Investigaciones en Optica.

1.2 The Ytterbium Ion

Regarding the Yb-doped materials, several investigations have revealed the technological potentiality of these systems since they may generate tunable lasers in the infrared region from 920 to 1060 nm and visible emission at 500 nm by cooperative effect. The cooperative luminescence is an upconversion process in which two interacting ions in the excited state decay simultaneously to the ground state, emitting one photon at twice the energy of single ion transition. 3D displays, intrinsic bistability for optical switching, and planar lasers for optical devices in telecommunications are some applications for cooperative emission in systems doped with Yb^{3+} ions.

The Yb^{3+} ion gives a laser emission around 1030 nm, such wavelength is near that of Nd^{3+} emission in 1060 nm. Nowadays, many works propose the Yb^{3+} ion as a replacement of Nd^{3+} ion for some applications, where Yb^{3+} ion will be better in the sense of luminescence properties. In the early of 90's, the laser diodes of InGaAs emitting around 950 nm appeared, leading to the study of new Yb^{3+} doped hosts. Also, new sources of pumping are adjusted with the excitation wavelength of Ytterbium, which present an absorption band between 900-980 nm. Yb^{3+} ion has many advantages in comparison with the Nd^{3+} ion [7]:

1.- There are only two manifolds in the Yb^{3+} energy level scheme in the $4f^n$ configuration, the $^2F_{7/2}$ ground state and the $^2F_{5/2}$ excited state. The lack of intermediate levels and the large separation between the excited state and the ground state manifolds reduces nonradiative decay (Figure 1.2.1). There is no excited state absorption since any high energy excitation such as 4f-5d transition or a charge transfer (CT) process are not accesible at high energies ($\lambda < 260nm$).

2.- The configuration of two manifolds in the Yb^{3+} energy level scheme, eliminates the energy transfer by cross relaxation which limits the lasers performance.

E (cm^{-1})

Charge Transfer Band

37000

4f-5d

25000 (400 nm)

There is no absorption

13333 (750 nm)

$^2F_{5/2}$ $\tau \sim$ ms

10000 (1 µm)

Low Quantum defect

Laser Emission ~1030 nm

~ 400-600 cm^{-1}
quasi 4- level

$^2F_{7/2}$

0
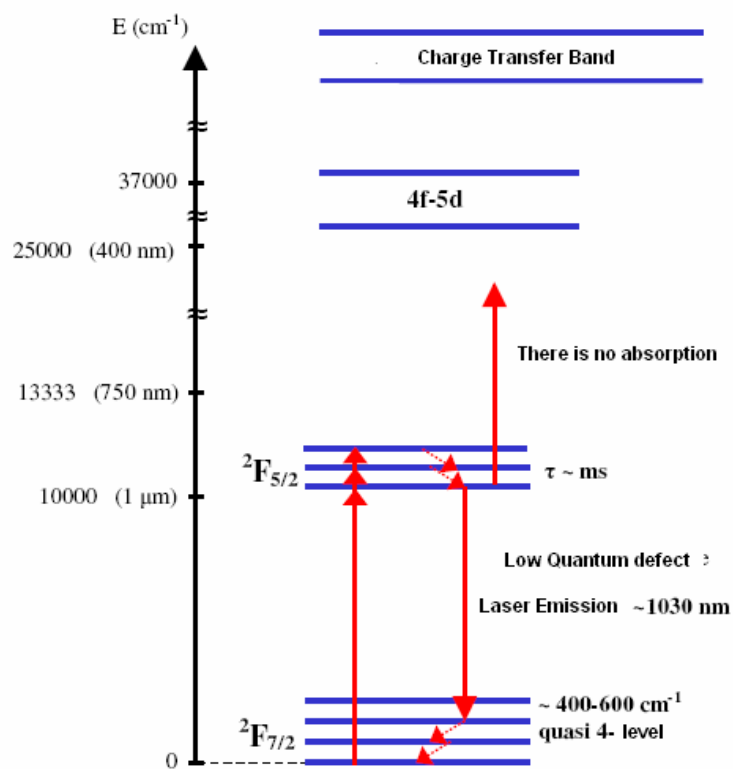
Figure 1.2.1: Energy levels of Yb^{3+} ion [7].

3. - The lifetime of excited state is 4 times higher than lifetime in others rare earths, this fact makes possible an efficient energy storage.

4.-Yb has a small quantum defect (10% below, in contrast with the 20- 25% for the neodymium ions), this reduces thermal charge.

In the case of lasers systems, ytterbium ion presents the following inconvenients: the laser emission remains in the excited state manifold (figure 1.2.2), but the energy level do not exceed 10 000 cm^{-1} and could be thermically populated. The reabsorption of emission increases during the laser threshold. Thus, choice of matrix is important for the behavior of a quasi-four-level laser system since the electric field sets the energy difference between the ground state and the excited state of the laser transition.
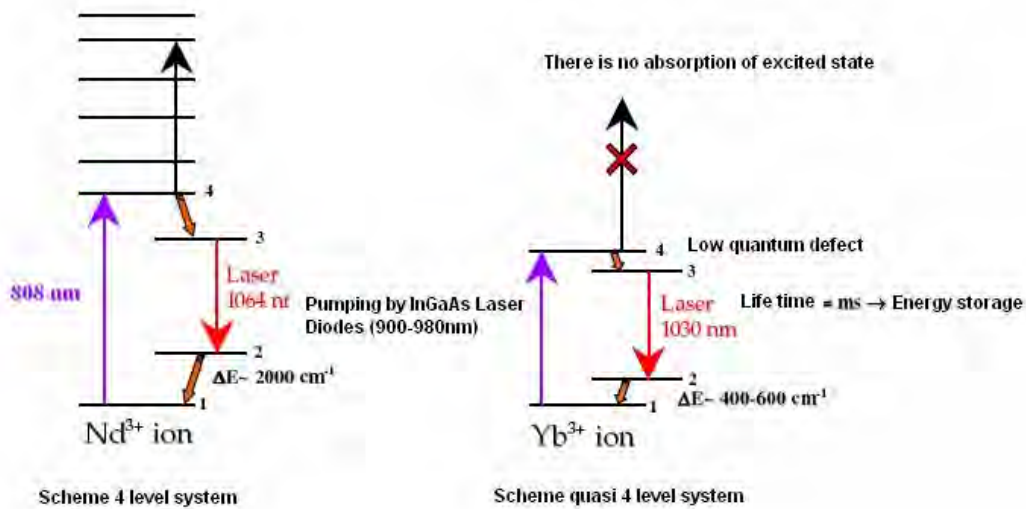
Figure 1.2.2: Quasi-four-level laser Scheme [7].

1.3 Barium Zirconate (BaZrO₃, BZO) Generalities

Dielectric materials are important for wireless communications technology. These devices require a high dielectric constant, ε, and low dielectric loss. BZO, is one of the constituent materials in electroceramic capacitors used in wireless communications. BZO is a dielectric material, chemically and mechanically stable.

Barium zirconate is a promising refractory ceramic material with a high melting point (2920°C) and low chemical reactivity towards corrosive compounds. It belongs to the $A^{2+} B^{4+} O_3$ perovskite family. BZO is a cubic oxide perovskite that does not follow phase transitions within the range between 4K and 1600K [8]. Thus, BZO has been used in high temperature superconductor applications [9]. Electroceramic applications have been done with BZO [10]. The crystalline space group of BZO perovskite is Pm-3m and the ideal unit cell is shown in Figure 1.3.1:
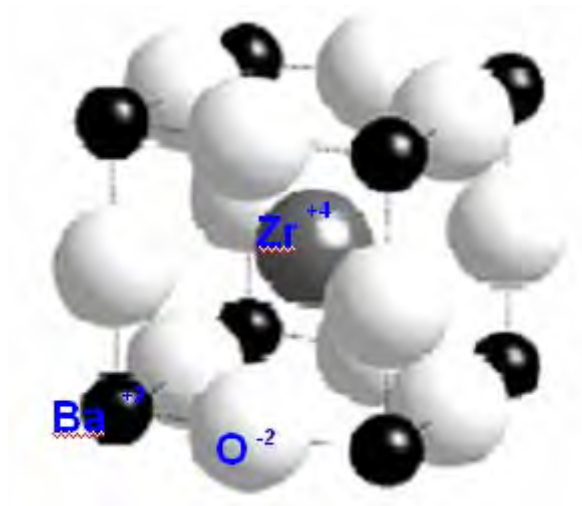
Figure 1.3.1: A cubic perovskite BaZrO₃ unit cell.

BZO matrix shows a great potential for several technological applications in electro-optic, waveguides, laser frequency doubling and high capacity memory cells [11]. There are a lot of studies about the chemical, physical, mechanical properties and crystalline structure of BZO, among the most relevant are:

1. Ahmed and collaborators have carried out studies about the structure and proton conductivity in Yb-doped BaZrO₃ [12]. Protons conducting solid electrolytes have got significant attention due to their wide range of technological applications, especially in fuel cells, batteries, gas sensors, hydrogenation/ dehydrogenation of hydrocarbons and electrolysers. In this work, a comparative analysis of X-ray and Neutron difraction data indicates that the structure of all Yb concentrations shows cubic symmetry (space group Pm-3m). Proton conduction in this material was mainly dominating in the temperature range (150–550 °C) while at higher temperature holes or oxygen ions transport seem to govern the conduction. Therefore Yb-doped BZO is presented as a very good candidate for high protonic conductivity .

2.- Khenata et al. have reported a theoretical study of structural, electronic and optical properties of cubic BaZrO₃ perovskites. The full-potential linear augmented plane wave (FP-LAPW) method as been implemented in the WIENK code [13]. Results for lattice constant, bulk modulus, band structure,

density of states, and refractive indices are given. These results are in agreement with the experimental data obtained by themeselves.

In the following table, we present the Thermophysical properties of BZO that have been studied and reported so far.

Table 1: Thermophysical properties of the BZO Perovskite.

Crystal system		
Lattice parameters(nm)	a	0.4192
	b	0.4192
	c	0.4192
Linear thermal expasion coefficient (K^{-1})	α	7.13E-6
Melting temperature (K)	T_m	2978
Shear modulus(Gpa)	G	103
Young's modulus (Gpa)	E	242
Comprenssibility (Gpa^{-1})	β	0.00786
Debye temperature (K)	θ_0	544
Vicker's hardness(Gpa)	H_V	4.95

Table 1 shows the high hardness and low compressibility of BZO, it is very important for protonic applications. The low linear thermal expansion coefficient is comparable with that of other ceramics. In addition, BZO can support high temperatures as we observe in melting temperature, that is critical for High power laser host applications.

There are some publications about luminescent properties of BZO: Zhang et al. have studied europium doped $BaZrO_3$ prepared by Pechini-type complex sol-gel method and reported weak orange luminescence of Eu^{3+} under UV excitation [14]. L. He et al. show strong red luminescence of $BaZr(BO_3)_2$:Eu,Si synthesized by sol-gel reaction where the Si^{4+} acts as sensitizer of luminescence [15]. Hence, the literature about the optical properties of bulk, micro or nano-sized BZO is reduced or non existent. On the

contrary, there is a lot of literature about the isomorphic $BaTiO_3$ which presents well known nonlinear optical properties in spite of the host undergoes phase transitions in temperature and imputity concentration [7].

To the best of our knowledge, no report about the luminescent properties of $BaZrO_3$:Yb^{3+} has been done up to now. With the Yb^{3+} ion as dopant, we expect an efficient luminescence of this perovskite. Since BZO is structurally more stable than ZrO_2, we suppose similar or even better luminescent properties for Yb doped BZO than for Yb doped ZrO_2. In addition, BZO presents cubic structure which should lead to low nonlinear optical properties.

1.4 Rare Earths Generalities

1.4.1 Single Rare-Earth Ions

The term rare-earth (RE) usually refers to the elements lanthanum (Atomic No. 57) through lutetium (Atomic No. 71) also known as lanthanides and the chemically similar elements scandium (Atomic No. 21) and yttrium (Atomic No. 39) [16]. The following discussion however will only address the lanthanides.

The electron configuration of the lanthanides is $[Xe]1(4f)^n(5d)^x(6s)^2$ with x = 1 in the case of lanthanum (n = 0), gadolinium (n = 7), and lutetium (n = 14) and x = 0 and n = 2 through n = 14 for cerium through ytterbium. In ionic crystals the rare-earths are usually incorporated as stable trivalent ions. The electron configuration for the trivalent lanthanides is $[Xe](4f)^{n+x-1}$. Divalent rare-earths can appear in crystals with divalent lattice sites. They can also appear if local charge compensation is provided by crystal defects such as F-centers in the sesquioxides and garnets or by the presence of quadrivalent co-dopants in the crystal [17, 18].

The spectroscopic properties of the trivalent rare-earths are dominated by transitions from $4f$ states to $4f$ and $5d$ states. Due to the completely filled $5s$

and 5*p* shell the 4*f* states are well shielded from influences of the crystal field [19, 20, 21]. These results in a low variation of the 4*f*-states in different local environments and narrow transition line-widths compared to those observed in transition metals, divalent rare-earths with 5*d*-states [22]. The strength of the shielding decreases with rising atomic numbers [23, 24].

The radius of the 4*f* wave-function and the radius of the trivalent ion decreases throughout the lanthanide row due to the stronger attraction of the electrons by the nucleus [25]. This lanthanide contraction has some effects when the ion is located in a crystal-field. Smaller ions generally are less affected by the crystalfield of a host material than larger ions in the same host due to the larger distance of the main part of the 4*f*-wave-function to the electrostatic field of the neighboring ions [26, 27, 28, 29].

The 4*f*-shielding and the lanthanide contraction influence the strength of the electron-phonon-coupling in the rare-earths. The strength of the electron-phonon-coupling for several rare-earths has been determined by Ellens by measuring the linewidths of electronic transitions and the intensities of vibronic sidebands [30, 31, 32]. It is rather strong for the elements in the beginning and the end of the lanthanide row and weaker for those in the middle. Furthermore the effects of hydrostatic pressure decrease through the lanthanide row due to the lanthanide contraction.

1.4.2 Rare-Earth Ions in a Crystal Field

When an ion is incorporated into a crystal lattice it is subject to the electrostatic field of the neighboring ions, also called ligands. The crystal-field potential can be introduced as an additional perturbation term to the free-ion Hamiltonian. In the one-electron approximation the potential can be written as:

$$H_{CF} = \sum_{k,q} B_q^k C_q^{(k)}$$

(1.1)

Table 2 Term-splitting of 4f-electrons in rare earths.

	Hamiltonian	Interaction	Quantum numbers	Energy splitting	Degeneracy	Term denotation	ΔE (cm^{-1})
Free-ion	H_0	Eff centr. field potential	$n,l,m_l,$ m_s	n,l	$2(2l+1)$	$n,l,(s,p,d,f)$	10^4-10^5
	H_{ee}	Coulomb repulsion Of 4f elec	$n,L,S,$ M_L,M	$L(S)$	$(2L+1)x$ $(2S+1)$	^{2S+1}L	10^4
	H_{so}	Spin-orbit coupling	$n,L,S,$ J,M_J	J	$(2J+1)$	$^{2S+1}L_J$	10^3
Crystal-ion	H_{cf}	Electrostatic field of the ligands	$n,L,S,$ J,M_J	M_J	2-fold Kramers	-	10^2

The $C_q^{(k)}$ are tensor operators, whose matrix elements can be calculated exactly, and the crystal-field parameters B_q^k are adjustable parameters [33]. The crystal-field has two effects on the energy-level structure of the free-ion: It induces a red-shift on the free-ion levels, which is called nephelauxetic effect and can be explained by a reduction of the free-ion parameters [34]. The second effect of the crystal-field on the free-ion is the lifting of the M_j-degeneracy of the $^{2S+1}L_J$ -manifolds. This Stark-splitting of the manifolds is usually in the order of some 100 cm^{-1}. According to the Kramers-theorem all levels of every ion with an uneven number of electrons have to be twofold-degenerate. This Kramers-degeneracy is a consequence of the time-reversal invariance and causes the $^{2S+1}L_J$ -manifolds of ions with an uneven number of electrons to split only into (2J + 1)/2 Stark-levels (Table 2), whereas the manifolds of ions with an even number of electrons are split into (2J + 1) levels [35].

The crystal-field parameters B_q^k include all the structural information of

the local environment of an ion. The superposition model [36] makes an attempt to separate intrinsic parameters from the geometrical factors. The one-electron crystal-field parameters are written as:

$$B_q^k = \sum_j \overline{B}_k(R_j) K_{kq}(\vartheta_j, \varphi_j)$$
(1.2)

$\overline{B}_k$ is an intrinsic parameter and depends only on the distance R_j and the type of ligand located at ($R_j, \vartheta_j, \varphi_j$). K_{kq} is a geometrical factor that includes the information about the local environment. Usually only the first ligand shell is used for the calculations, while the influence of higher ligand shells is neglected. This model allows an analysis and easier comparison of the crystal-field in similar host materials or monotonically changing local environments, such as crystals under hydrostatic pressure.

1.4.3 Dimer Systems

If two ions are placed close to each other in a crystal, additional effects on the spectroscopic properties occur. Due to the overlap of the electron-wave functions of the optically active electron shells the two ions form a pair that needs to be treated as a single dimer system or molecule in terms of quantum mechanics. The main cause for this behaviour is the Coulomb-interaction of the electrons of the two ions, referred to as exchange interaction. A theoretical and experimental study of dimer systems can be found in [37].

1.4.4 Cooperative Optical Transitions

A second impact of exchange-coupling on ion-spectra is the existence of cooperative optical transitions. That is, simultaneous absorption or emission of one photon by two coupled ions, see Figure 1.4.4.1.
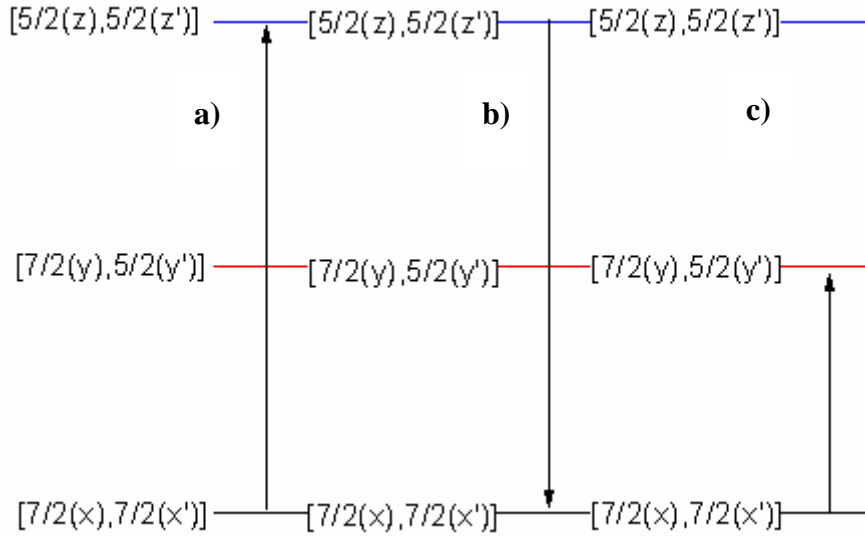
Figure 1.4.4.1 : a) Cooperative absorption, b) Cooperative emission of Ytterbium, c) Vibronic excitation of a Yb pair.

The resulting absorption and emission energies are the added energy differences of the two single ions. The first report of cooperative transitions has been published by Varsanyi and Dieke in Pr:LaCl3 [38]. Cooperative emission of Yb-dimers in the green spectral range was first observed by Nakazawa in YbPO4 [39]. Since then, cooperative processes have been studied in numerous Yb-compounds [40, 41, 42, 43] and transition-metal systems [44, 45, 46].

Cooperative transitions in ytterbium systems are mainly observable as a weak emission in the green spectral range at half the emission wavelength of the infrared emission. In this case both ions of the dimer are in their excited state and emit one photon while simultaneously changing to the ground state: $\left[\frac{5}{2}(x'),\frac{5}{2}(x)\right] \rightarrow \left[\frac{7}{2}(y'),\frac{7}{2}(y)\right]$ (x, x', y, and y' denote an arbitrary Stark-level of the manifold,). The same process appears in absorption when the dimer absorbs one high energetic photon and both coupled ions are switched to their excited state. The cooperative transitions are weaker than the infrared transitions by a factor of $10^3 - 10^4$, depending on the material. Furthermore, cooperative emission in the infrared has also been observed [47]. Here one of the ions is in its excited state and the other is in a higher Stark-level of the

ground state . This can create slightly shifted, weak mirror images of the infrared emission $\left[\frac{7}{2}(x'),\frac{5}{2}(x)\right]\rightarrow\left[\frac{7}{2}(y'),\frac{7}{2}(y)\right]$ The oscillator strength of the cooperative transitions is proportional to the exchange- and super-exchange-interaction of the coupled ions. Theoretical calculations of the oscillator strengths have only been published for Yb:CsCdBr$_3$ [48]. Here, ytterbium ions can only fit into the CsCdBr$_3$ lattice if two ytterbium ions replace three cadmium ions. Therefore all Yb-ions in the crystal form pairs of well defined nearest neighbor distances. Calculations for other materials with statistical dopant distributions would involve the calculation of all possible nearest neighbor combinations, numbers, interaction distances, and statistical probabilities, which has not been accomplished up to now.

Notable is also that the intensity of vibronic sidebands is reduced by a factor of up to 20 in the cooperative ytterbium transitions compared to the sidebands of single-ion transitions at low temperatures. Hehlen et al. have offered an explanation for this phonon selection effect [41]: A vibronic excitation of a pair $\left[\frac{7}{2}(0),\frac{7}{2}(0')\right]\rightarrow\left[\frac{5}{2}(y),\frac{7}{2}(y')\right]$ is immediately followed by a non-radiative transfer to the lowest Stark-level of the $\left[\frac{5}{2},\frac{7}{2}\right]$ (multiplet $\left[\frac{5}{2}(0'),\frac{7}{2}(0)\right]$). Due to the slightly different vibrational energies in the ground and excited-state a different excitation energy would be needed to excite the analogous vibronic excitation for the second ion $\left[\frac{5}{2}(0),\frac{7}{2}(0')\right]\rightarrow\left[\frac{5}{2}(y),\frac{5}{2}(y')\right]$ and therefore the rate of vibronic pair transitions is lowered.

1.5 Interaction with Lattice

As mentioned earlier, the electron-phonon-coupling in ytterbium is one of the strongest in the lanthanide series. Therefore, the strength an influence of phononic features in the optical spectra is very high compared to other rare-earths. The effects of the electron-phonon-coupling will be introduced in this section.

1.5.1 Line-Broadening

Several mechanisms lead to a line-broadening of the rare-earth transitions. The broadening of an energy level can be written as:

$$\Delta E_{phon} = \Delta E^D(T) + \Delta E^R(T) + \Delta E^{Orb}(T) + \Delta E^{MR}(T) + \Delta E^{Rad}(T) \qquad (1.3)$$

The natural linewidth ΔE^{RAD}, the broadening by multi-phonon-relaxation ΔE^{MR}, and the broadening by the Orbach-process ΔE^{Orb} a resonant two phonon process can usually be neglected [49,50,51,52]. Furthermore the temperature dependent inhomogeneous line-broadening as well as the broadening by local distortions of the crystal lattice are not taken into account.

The two remaining terms are mainly responsible for the temperature dependence of the linewidth: ΔE^D describes the influence of the direct single-phonon absorption and emission. ΔE^R is due to the two-phonon Raman-process. First the i state absorbs a phonon and reaches a virtual state j'. Then a phonon of different energy is emitted and the atom reaches the state j. The energy of the absorbed and emitted phonons is considered to be large compared to the energy difference between the states i and j, see Figure 1.5.1.1.
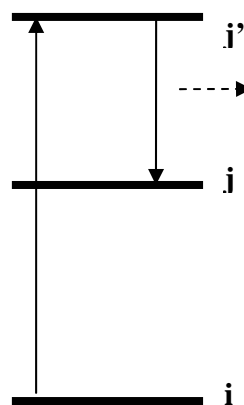

Figure 1.5.1.1: The two-phonon Raman process.

1.5.2 Vibronic Sidebands

Most trivalent rare-earths show nearly exclusively pure electronic to electronic transitions. Transitions of coupled electronic and vibrational states (vibronic states) are usually very weak. Some rare-earth ions, like the ytterbium ion, however, show a stronger coupling between electronic and phononic states which leads to the formation of vibronic sidebands with transition strengths comparable to those of purely electronic transitions. A detailed theoretical analysis of electron-phonon interaction in rare-earths can be found in [53]. Since the electron-phonon coupling can still be considered small, the interaction of an ion with lattice phonons can be described by a perturbation term to the free-ion Hamiltonian [54]:

$$ HE_{el-ph} = \sum_{\alpha,\overline{q},\xi} e \Big[V(\overline{r}_\alpha,\overline{q},\xi) \cdot a_{\overline{q}\xi} + V^*(\overline{r}_\alpha,\overline{q},\xi) \cdot a^t{}_{\overline{q}\xi} \Big] \qquad (1.4) $$

with the wave-vector $\overline{q}$ and branch ξ of the phonon and the construction and destruction operator of the phonons a and $a^t \cdot \overline{r}_\alpha$ is the position of the 4*f* electron.

1.5.3 Coupling of Vibronic and Electronic Levels

Most studies treat vibronic sidebands of transitions as isolated from other electronic levels. If vibronic sidebands overlap with neighboring electronic levels, the coupling between the sideband and the level can lead to a deformation or splitting of the transition [55, 56, 57, 58]. Figure 1.5.3.1 shows the shape of a transition from an electronic level to a coupled electronic-vibronic state for several energy differences between the coupled lines [59]. The larger the energy difference, the smaller the effect of the coupling. In the case that the coupling electronic and vibronic states have the same energy, the transition takes the shape of a symmetric double structure with no peak at the position of the original electronic line.

In case of ytterbium a coupling between the vibronic sidebands and electronic transitions is very probable. The impact on the Yb^{3+}-spectrum can be modeled if the complete phonon dispersion curves are known and the vibronic sidebands can be calculated. Lupei et al. have modeled the coupled electronic-vibronic spectra for ytterbium-doped YAG, $LiNbO_3$, and YLF with the success of being able to unambiguously identify the electronic Stark-levels of the $^2F_{5/2}$ state [60] In Figure 1.5.3.2 the coupling between an electronic level at 420 cm^{-1} and three vibronic levels is displayed. It is notable that the strongest peak does not appear at the position of either of the levels but shifted away from the coupled levels. Features like this can be seen in many low temperature spectra of the ytterbium-doped sesquioxides. The data on vibronic transitions in the sesquioxides is unfortunately not sufficient for quantitative modelling of the actual structures found in the spectra [61].
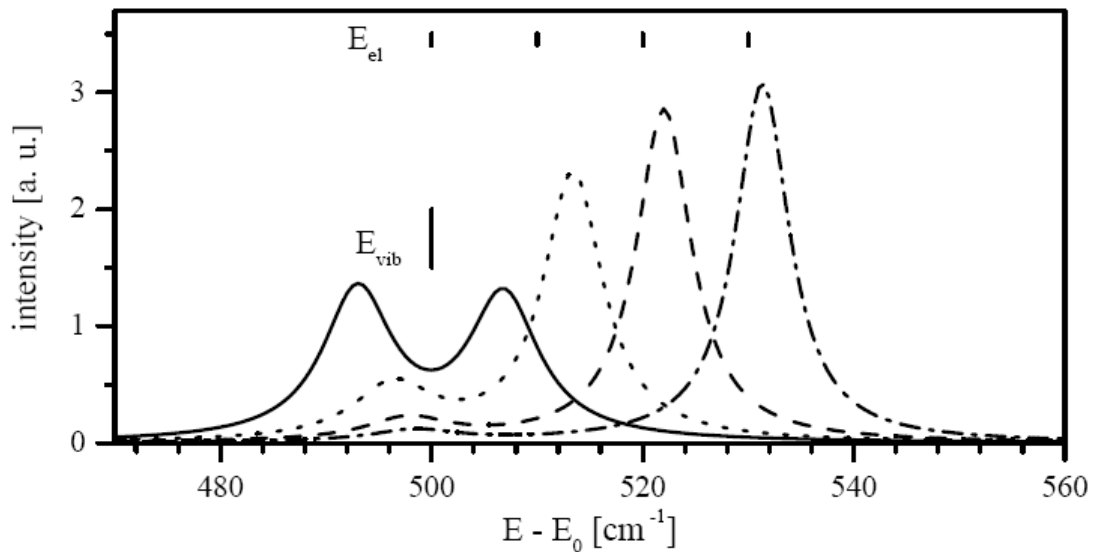
Figure 1.5.3.1: Calculation of the coupling between a vibronic sideband at 500 cm^{-1} and an electronic line. The shape of transitions from another level to the coupled electronicvibronic- state depends on the energy separation between the vibronic and electronic line $\Delta E = E_{vib} - E_{el}$. The symmetric double structure appears for $\Delta E = 0$. For larger ΔE the influence of the coupling between the electronic- and vibronic-line becomes weaker and the lines show as separated features.
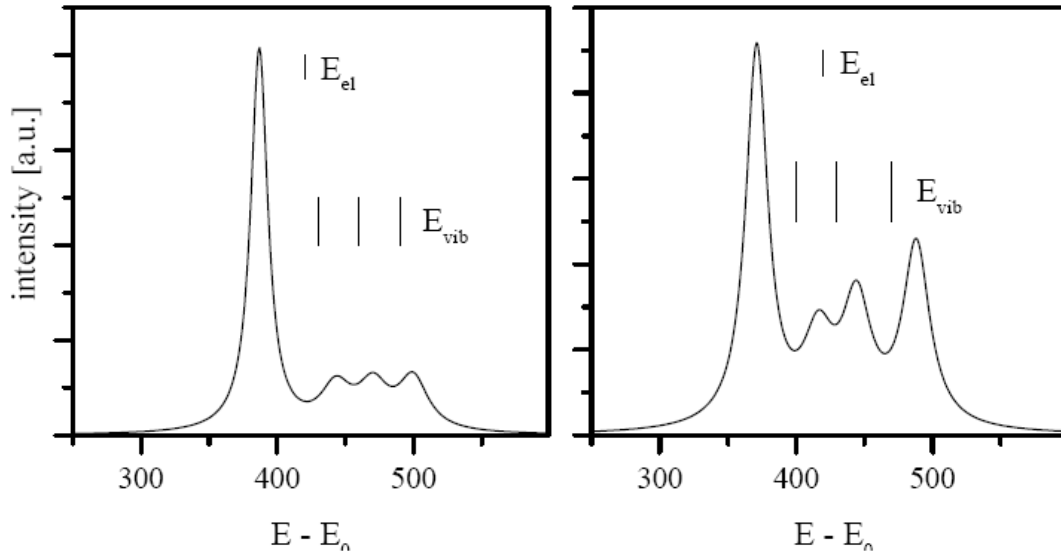
Figure 1.5.3.2: Calculation of the coupling between an electronic level at 420 cm^{-1} and three vibronic sidebands.

1.6 Energy Transfer

1.6.1 Intraionic Processes

Intraionic processes are those in which one ion or a coupled ion-pair interacts with photons or phonons. Interactions with photons are called radiative transitions, those with phonons non-radiative transitions.

1.6.2 Radiative Transitions

Absorption, stimulated and spontaneous emission: The basic radiative transitions are ground-state absorption (GSA), stimulated emission, and spontaneous emission. They were described by Einstein using the coefficients B_{ji} (absorption), B_{ij} (emission), and A_{ij} (spontaneous emission) [62, 63]. In thermal equilibrium the population of the energy levels of a system follows the Boltzmann statistics:

$$N_j = N_i e^{\frac{E_i - E_j}{kT}} \tag{1.5}$$

with the temperature T and the population densities $N_{i,j}$ and the energies $E_{i,j}$ of the levels i and j. By comparing coefficients to Planck's radiation law:

$$E(\nu) = \frac{8\pi h \nu^3}{c^3} \cdot \frac{1}{e^{\frac{h\nu}{kT}} - 1}$$

(1.6)

the Einstein-relations can be deduced:

$$B_{ij} = \frac{g_j}{g_i} B_{ji}$$

(1.7)

with the degeneracy level $g_{i/j}$ of the state $|i/j\rangle$ and

$$\frac{A_{ij}}{B_{ij}} = \frac{8\pi h n^3 \nu^3}{C_0^3}$$

(1.8)

with the frequency:

$$\nu = \frac{E_i - E_j}{h}$$

(1.9)

n is the refractive index of the material and $E_{i/j}$ is the energy of the state $|i/j\rangle$. The transition cross section σ_{ij} is given by:

$$\sigma_{ij} = \frac{2\pi^2 \nu}{3n\varepsilon_0 C_0} \cdot |\mu_{ji}|^2 = B_{ji} \cdot \frac{nh\nu}{C}$$

(1.10)

with the dipole-matrix element μ_{ji} and the speed of light within the material c [64]. The radiative lifetime τ_{rad} of an excited state $|i\rangle$ is defined as the reciprocal of the sum of the spontaneous radiative transition rates to all energetically lower levels $|j\rangle$:

$$\tau_{rad}(|i\rangle) = \frac{1}{\sum_j A_{ij}}$$

(1.11)

The branching ratio β_{ij} determines the percentage, that one transition $|i\rangle \rightarrow |j\rangle$ takes up of the entire transition rate from a state $|i\rangle$:

$$\beta_{ij} = \frac{A_{ij}}{\sum_k A_{ik}}$$

(1.12)

1.6.3 Excited State Absorption (ESA)

Absorption from excited states is analogous to the ground state absorption. ESA can be positive or negative for the laser properties of a system. Excited state absorption from the upper laser level can lead to a depopulation of this level and therefore lower the laser efficiency. On the other hand ESA can be used to populate energy levels of higher energy than the pump light and allow laser operation from those levels. In the ytterbium-system ESA can only occur to the conduction band, to charge transfer states, or in coupled ytterbium-impurity pairs. Strong 4f-4f ESA as in other rare-earths cannot occur due to the simple energy level structure.

1.6.4 Reabsorption

If a photon that has been emitted is absorbed again by the same activator type the process is called reabsorption. Reabsorption can become a significant process if the overlap of the absorption and emission is large. In the case of ground state lasers, reabsorption is a well-known loss process. Furthermore it can prolong the measured lifetime of an excited state compared to the real lifetime of the level, the so-called radiation trapping. With ytterbium-doped YAG, lifetimes up to 50% higher than the radiative lifetime could be measured depending on the used setup [65, 66].

1.6.5 Non Radiative Transitions

Multi-phonon-relaxation is the transition of an excited state into a lower one by interaction with one or more lattice phonons. The excitation energy is directly transformed into heat by this process. Multi-phonon relaxation into energetically close levels is very fast and can efficiently depopulate excited states. The temperature dependent non-radiative transition rate W_{nr} is described by [67]:

$$W_{nr}(T) = W_0 \cdot e^{-a\Delta E} \left[1 - e^{\frac{\hbar w_{eff}}{kT}} \right]^{-p}$$

(1.13)

The empirical parameter W_0 depends on the host material and a describes the electron-phonon coupling, which can be considered weak in the case of 4f electrons. ΔE is the energy difference between the two states and $\hbar w_{eff}$ is the effective phonon energy of the host material. The number of phonons needed to bridge the energy gap is given by $p = \dfrac{\Delta E}{\hbar w_{eff}}$. Usually, the temperature dependence of $\hbar w_{eff} > kT$ can be neglected in the case of ytterbium. The non-radiative lifetime of an excited state is defined as:

$$\tau_{nr} = \frac{1}{w_{nr}}$$

(1.14)

The fluorescence lifetime can now be calculated from the radiative and non-radiative lifetime:

$$\frac{1}{\tau} = \frac{1}{\tau_{rad}} + \frac{1}{\tau_{nr}}$$

(1.15)

The fluorescence lifetime can be determined experimentally from the decay of the fluorescence intensity I, which is single exponential in the simplest case:

$$I(t) = I(0)e^{(\frac{-t}{\tau})}$$

<div align="right">(1.16)</div>

1.7 Selection Rules for Radiative Transitions

The radiative transitions in the trivalent lanthanides occur mainly between $4f^n$-$4f^n$ states. Since the start and end-state of these transitions have the same parity, electric-dipole transitions are forbidden by the Laporte selection rule and only magnetic dipole transitions can occur [68]. Magnetic dipole transitions are generally weaker than electric dipole transitions by a factor of 105. Under the influence of a non-inversion-symmetric crystal field, however, configurational mixing between $4f$ and opposite parity states like $4f^{n-1}5d$-states partly allow electric dipole transitions between $4f$-sates in the lanthanides [69]. In the case of crystallographic sites with inversion symmetry the Laporte selection rule can be weakened by non-centric distortions like lattice defects. In general the weakening for sites with inversion symmetry is still considerably smaller than the weakening for non-inversion sites. The general selection rules for electric dipole transitions can be summarized as follows [68, 70]:

1. $\Delta l = \pm 1$

2. $\left| \Delta S \right| = 0$

3. $\left| \Delta J \right| \leq 2l = 6$

4. $\left| \Delta L \right| \leq 2l = 6$

In the case of rare-earth ions with an even number of electrons some additional selection rules apply:

$J = 0 \leftrightarrow J^{'} = 0$ is forbidden

$J = 0 \leftrightarrow J^{'} = 2,4,6$ should be strong

$J = 0 \leftrightarrow J^{'}$ unneven should be weak

The mixing of 4f- and opposite-parity-states and the resulting transition rates have been calculated by Judd and Ofelt [71, 72]. The transitional-matrix elements μ_{ji} and the Judd-Ofelt parameters Ω_{j} can be determined from measurements of the oscillator strengths of several ground state transitions. With these parameters the oscillator strengths of the remaining transitions can be calculated with an accuracy of about 20%. In the case of the Yb-ion this method can not be successfully applied, since the transitions from the only existing excited state are not sufficient to determine all the necessary parameters [73].

1.8 Interionic Processes

Interionic processes involve the direct transfer of excitation energy between two ions without absorption or emission of photons. The involved ions are coupled through multipolar-, exchange-, or super-exchange-interaction.
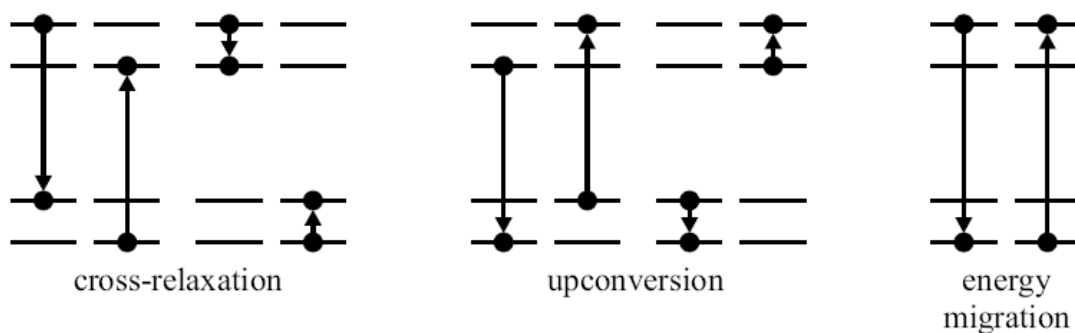

Figure 1.8.1: Interionic processes.

Förster and Dexter have developed a model to describe energy transfer on the basis of multipolar- and exchange-interaction [74, 75]. In the case of low dopant concentrations the transition probability for an electric-dipole-interaction is given by:

$$W_{DA,ed} = \frac{3\hbar^4 c_0^4}{4\pi n^4 R_{DA}^6 \tau_{rad,D}} \cdot \int \sigma_{abs,A}(E) dE \cdot \int \frac{f_{em,D}(E) \cdot f_{abs,A}(E)}{E^4} dE = \frac{C_{DA}}{R_{DA}^6} \qquad (1.17)$$

with the vacuum speed of light C_0, the refractive index n, the distance between donor and acceptor R_{DA}, the radiative lifetime of the donor $\tau_{rad,D}$, the absorption cross section of the acceptor $\sigma_{abs,A}$, and the normalized line shapes of the emission line of the donor $f_{em,D}$ and the absorption line of the acceptor $f_{abs,A}$. The micro-parameter C_{DA} is a measure for the efficiency of the transfer process. More detailed information on energy transfer processes is given in the books of B. Henderson and G. F. Imbusch [70] as well as R. Reisfeld and C. K. Jørgensen [76]. A study of energy transfer processes in ytterbium-doped scandia can be found in the work of A. Bolz [66]. The different types of energy transfer processes (see Figure 1.8.1) will be described in the following:

1.8.1 Cross Relaxation

Cross-relaxation is the full or partial transfer of excitation energy to an acceptor in a lower level. This process can be very efficient, if the energy differences in the participating donor and acceptor levels are resonant or the energy needed to excite the acceptor is slightly smaller than the energy provided by the donor. Cross relaxation is often used to sensitize ions with small absorption cross section by codoping with ions with strong absorption, like ytterbium, to achieve a more efficient excitation.

1.8.2 Upconversion

Upconversion is similar to cross relaxation except that the acceptor is initially in an excited state. The resulting excitation energy of the acceptor is higher than the original excitation energy of the donor. This process allows the realization of lasers with a shorter emission than pump-wavelength [77].

1.8.3 Energy Migration

Energy migration is the resonant energy transfer between two ions of the same species. This process allows the excitation energy to quickly spread out and therefore raises the probability of the other energy transfer processes. Energy migration is described by several models depending on the ratio of transfer rates between two donors C_{DD} and between donor and acceptor C_{DA}. Right after the excitation a fast migration of the excitation energy between donors occurs [78]. After this first, fast migration to neighboring ions, the further spreading of energy can be either described by the diffusion-model in the case that C_{DD} is much smaller than C_{DA} [79] or the hopping-model for C_{DD} larger than C_{DA} [80]. Due to the strong dependence of the transition probabilities on the distance between donor and acceptor, the energy transfer processes become most important at high doping levels. This can be very useful if energy transfer is desired as in sensitized systems or can be harmful if the excitation energy is transferred away from the active ion to unwanted impurities. In the case of highly doped ytterbium systems, energy transfer to such impurities can cause a nearly complete quenching of the excitation energy and therefore make laser operation impossible. The energy quenching of $Yb_3Al_5O_{12}$ and $Yb:RE_2O_3$ has been investigated in the works of V. Müller and A. Bolz [81,66].

1.9 Structural Characterization and Morphology

1.9.1 X-Ray Diffraction (XRD)

In 1912, Max von Laue suggested that the arrangement of the atoms in crystalline solids, that followed a regular pattern, might be used as diffraction gratings for measuring x-ray wavelengths.

When a wave-probe impinges upon a collection of scattering centers, each scattering center generates waves that are radiated outward, in all directions. The resultant wave in one specific direction depends on the interference between all the separate centers. It is a remarkable fact that the

atoms lying on any plane within the crystal, act with respect to the incident wave as a semimirror concerning to visible light; that is, they reflect a portion of the wave whereas allows the rest to pass through. These are the Bragg planes and Bragg reflections that in 1913 W. H. Bragg and W. L. Bragg (father and son, respectively) used to develop the fundamental theory of x-ray diffraction by crystals.

In a crystalline arrangement, if an incident wave at a θ angle hits Bragg parallel planes (not the normal to the reflecting planes), the wave is partially reflected at an angle θ from the Bragg planes. If the reflection of the second plane is taken into account, the two reflected waves will constructively interfere at any distant point, only if they are in phase. The condition for constructive interference between waves reflected from adjacent parallel Bragg planes, which are separated by an interplanar distance *d* is represented as:

$$n\lambda = 2dSin\theta \qquad\qquad\qquad (1.18)$$

where the order of the reflection n takes positive integer values, λ is the wavelength of the incident x-ray. This equation is known as the Bragg's law and is the basis of all coherent x-ray and electron diffraction effect in crystals (De Broglie waves). It is used to measure interatomic distances comparable to wavelength. For instance, if n, λ and θ are known, d can be computed. The angle between the undeviated ray and the reflected ray is 2θ and the Bragg planes are parallel to the bisectrix of this 2θ angle.

An X-ray diffractometer is used to measure interatomic distances and to identify reflection planes. A monochromatic x-ray source impinges on a crystal sample whose structure and interatomic dimensions are unknown. A detector that is sensitive to x-ray ionization effects gets the intensity of the x-rays. Even though the detector and the sample can be rotated, the detector is set at angle 2θ from the forward beam, as is shown in Figure 1.9.1.1 The x-ray intensity in the detector indicates a strong maximum when the Bragg condition is satisfied. Thus, it is possible to determine d.
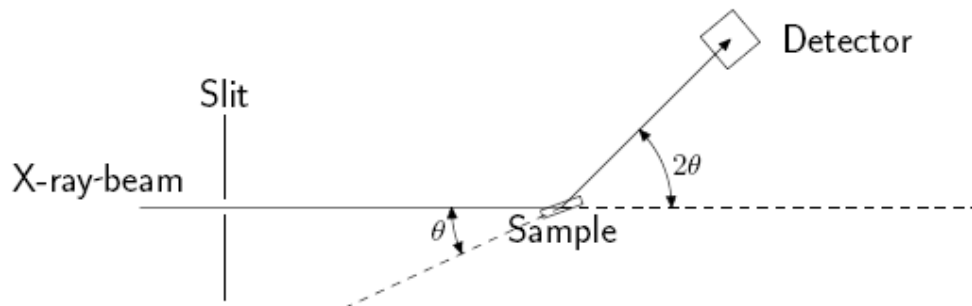
Figure 1.9.1.1: Schematic representation of an X-ray Difractometer.

If the sample used is in a powder form, it consists of a very large number of randomly oriented microcrystallites. Only those particular microcrystallites that are oriented in such way as to satisfy the Bragg condition will produce a strongly diffracted beam (see Figure 1.9.2). The other microcrystals will not diffract the incident beam coherently. Therefore, the emerging beam will consist of two parts: an intense, central undeviated beam and a scattered beam that makes a 2θ angle with respect to the incident beam. The θ angle is uniquely determined, for a given order, by the Bragg relation. When the scattered beam is detected in one plane, an intensity pattern consisting of a strong central spot surrounded by a circle is used -by measuring its radii and the distance between the sample and the plane- to determine the 2θ angle and thus the interplanar distance can be calculated from the Bragg relationship. Actually, there are many sets of planes in any single crystal. A Bragg plane is any plane that contains atoms. So many planes can be defined. It is clear, that the various planes will differ in the values of their interatomic space d, consequently, there will be a number of Bragg angles θ, that satisfy the Bragg relation for a particular set of Bragg planes. The x-ray diffraction pattern will therefore be somehow more complicated than the indicated in Figure 1.9.1.2 It will have a number of concentric circles (called Debye and Scherrer rings). Each one corresponding to a diffraction from a particular set of Bragg planes. The intensities of the reflected beams from the different planes will not be the same, because both the number of atoms per unit area in one plane and the type of atoms, may differ from it in another plane. The effectiveness of an atom to scatter radiation is due to both the number and the distribution of electrons in the atom [82]. So, if thre are different atoms in the lattice, different intensities peaks are expected.

This characteristic is taken into account by the atomic form factor f.
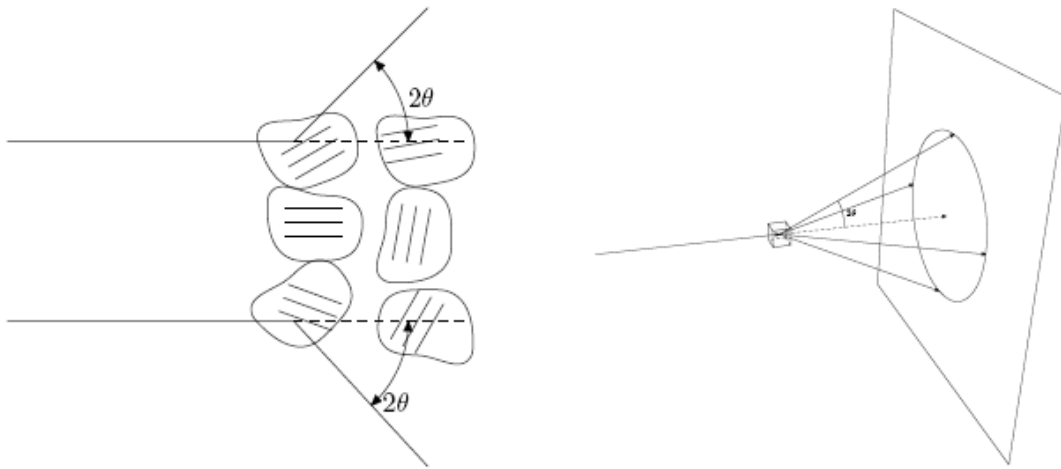
Figure 1.9.1.2: Right, Nanopowder crystallites are scattering the incident x-ray radiation. Those satisfying Bragg condition will interfere constructively and form a circular pattern.

When N atoms are in the base associated with one lattice point, the scattering radiation from these atoms may interfere constructively or destructively depending on the position of the atoms. The arrangement of the atom and their individual atomic form factors are included in the structure factor $S_{h,k,l}$ [83].

$$S_{h,k,l} = \sum_{j=1}^{n} f_j e^{-i(kx+ly+mz)} \qquad (1.19)$$

here x, y, and z are the coordinates of the j_{th}-atom as fractions of the lattice constants. The exponential factor explains the difference in phase of the scattered waves due to their path difference, as they scatter from atoms at different positions in the crystal. Thus, the intensity of the scattered X-Ray is proportional to $|S_{h,k,l}|^2$

1.9.2 Scanning Electron Microscopy (SEM)

In Scanning Electron Microscopy (SEM), electrons are generated from thermionic or field emission cathode and accelerated by a voltage of 1-50 kV between cathode to anode. The electron probe diameter is around 1-10 nm with probe current of 10^{-10}-10^{12} A and impinges over the specimen surface. This focussing is achieved by a pair of electromagnets acting as condenser lenses. A deflection coil system in front of the objective lenses scans the electron probe in a raster across the specimen and in synchronism with the electron beam of a separate cathode-ray tube (CRT). The intensity of the CRT is modulated by one of the signals recorded to form an image.

The magnification can be increased simply by decreasing the scan-coil current and keeping the image size of the CRT constant [84]. When the primary electrons collide with the sample, they lose energy by repeated scattering and absorption within the sample. This interaction between the electron beam and the sample results in the emission of electrons and electromagnetic radiation which can be detected to produce an image by the secondary electrons, see Figure 1.9.2.1. These electrons have energy around 2-5eV. By convention, the limit between secondary electrons and backscattered electrons is 50ev. Secondary electrons are generated by inelastic excitation to high energy levels so the excited electrons can overcome the work function before being decelerated to the Fermi level. Backscattered electrons are between 50eV and the accelerator potential energy $E = eU$. This range is due to deceleration of electrons that have suffered multiple energy losses and multiple scattering through large angles. Auger electron production is an alternative to characteristic x-ray emission after the ionization of an inner shell.The de-excitation energy released when an electron from an upper shell fills the vacancy in the ionized shell can be converted to an x-ray radiation or the energy may be transferred to another atomic electron, which leaves the specimen as an Auger electron.

If the specimen is transparent to the incident electrons, the transmitted electrons can easily be recorded by a scintillation or semiconductor detector situated below the specimen support. A sample that shows sufficiently transmission to 10-50KeV electrons will be an excellent specimen for a 100 keV Transmission electron microscopy (TEM). The recording of transmitted electrons is an additional possibility in SEM.

Secondary electrons are generated within a few nanometers from the sample surface and then they can be detected by using a photomultiplier device and the resulting signal can be put into a two-dimensional array as a digital image or be displayed as already was mentioned. The brightness of the signal is proportional to the number of secondary electrons picked by the detector. When one uniform area is activated, certain number of electrons are emitted from this surface zone. But when this area is nonuniform about the axe beam (oblique incidence), one side of the beam will decrease and more secondary electrons will be detected. Then, edges are brighter than flat surface. This leads to images with three-dimensional appearance. By using SEM a resolution of 1nm can be achieved. However, the imaging of a surface topography by Transmission electron microscope (TEM) is superior by one order of magnitude in resolution [84].
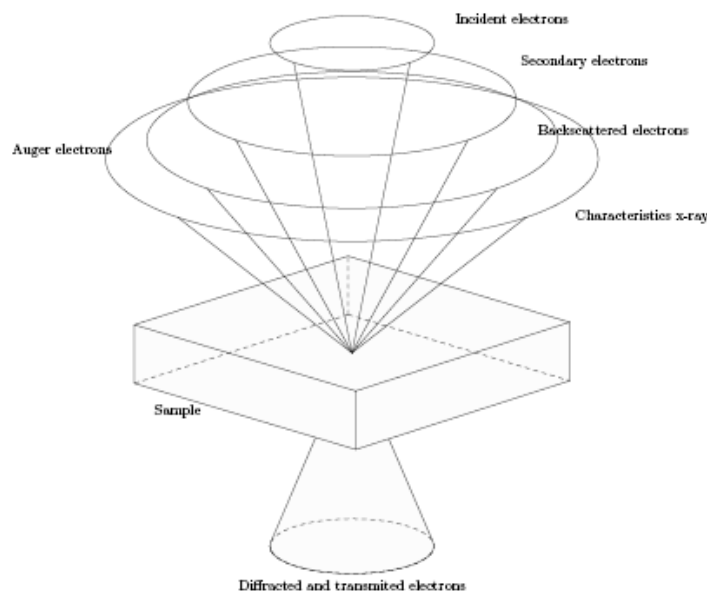

Figure 1.9.2.1: Electron beam is incident on sample, then electrons go under one of the depicted processes.

1.9.3 Infra-Red Fourier Spectroscopy (FTIR)

The movement of the ions in the crystal creates a dynamic field which acts on the doping ion. Strong interactions between the Ytterbium and the phonons of the matrix [85, 86] give place to vibronic effects [87], sometimes intense enough to appear in the spectra absortion spectra. These vibronic effects are regularly spaced electronic lines (mainly the fundamental line) in the spectrum, with a variation in energy corresponding to a whole number of times the energy of the active mode vibration. They have decreasing intensity and normally only the first can be observable.

Another consequence related to these electron-phonon interactions is the resonant coupling between the vibration modes of the matrix and the electronic levels of the Yb ion [88]. In spite of the shielding effect of the external electron shells $5s^2$ and $5p^6$, the couplings take place when energy between two Stark sublevels is in close resonance with the phonon energy of the host matrix. This coupling induces modifications in the optical spectra: broadening of the lines, phonon assisted energy transfer processes, unfoldings or shifts, stokes and antistokes asymmetries, etc. Hence, the objective with the FTIR spectroscopy is to observe the phonon modes and phonon energy that may change with annealing temperature and concentration.

1.10 References

[1] V. Kiisk, I. Soldos, O. Sild, and J. Aarik, *Spectral-spatial redistribution of self-trapped escitonic emission in thin anatase films,*in: 19th Congress of the International Commission for Optics (ICO XIX), "Optics for the Quality of Life", Technical Digest (A. Consortini, G.C. Righini, Eds.) Proc. SPIE 4829. 813 (2002).

[2] V. Kiisk, I. Soldos, O. Sild, and J. Aarik, *The influence of a waveguiding structure on the excitonic luminescence of anatase thin films*, Optical Materials 27, 115 (2004).

[3] V. Reedo, S. Lange, V. Kiisk, A. Lukner, T. Tâtte, and I. Sildos, *Influence of ambient gas on the photoluminescence of sol-gel derived TiO_2:Sm^{3+} films, Optical Materials and Applications* (A. Rosental, ed.), Proc. SPIE 5946. 59460F (2005).

[4] V. Kiisk, I. Soldos, S. Lange, V. Reedo, T. Tâtte, M. Kirm, and J. Aarik, *Photoluminescnece characterization of pure and Sm^{3+}-doped thin metaloxide films*, Appl. Surf. Sci. 247, 412 (2005).

[5] S. Lange, I. Sildos, V. Kiisk, J. Aarik, and M. Kirm, *Photoluminescence of RE-doped thin metal oside fils*, phys.stat. sol. (c) 2, 326 (2005).

[6] Valter Kiisk, work thesis: *Optical investigation of Metal-Oxide Thin films,* Dissertationes Physicae Universitatis Tartuensis (2005).

[7] Elena Canibano Crespo, *Propriétés spectroscopiques de l'ion Yb3+ dans les familles d'oxydes de molybdates $K_5Bi(MO_4)_4$, de grenats $Y_3Al_5O_{12}$, $Gd_3Ga_5O_{12}$, $Lu_3Al_5O_{12}$ et de perovskites $YAlO_3$. Analyse de mécanismes d'extinction par concentration et évaluation de l'émission laser.* Ph.D. thesis, Université Claude Bernaud Lyon, France (2002).

[8] Per G. Sundell, Mrten E. Bjorketun, and Goran Wahnstrom*. Thermodynamics of doping and vacancy formation in $BaZrO_3$ perovskite oxide from density functional calculations*, Physical Review B 73, 104112 (2006).

[9] K.J. Son, R.K. Ko, Y.S. Lee, J.S. Yang, Y.M. Park, Manglesh Dixit, H.S. Kim, H.S. Ha, D.W. Ha, S.S. Oh, D.J. Kim, C. Park and S.-I. Yoo, *The flux pinning enhancement of YBCO film prepared by PLD using composite targets doped with BaZrO$_3$ nanopowder, Physica C 445, 656 (2006).*

[10] Joseph W. Bennett, Ilya Grinberg, and Andrew M. Rappe*, Effect of symmetry lowering on the dielectric response of BaZrO$_3$,* Physical Review B 73, 180102 (2006).

[11] V.E. Henrick, P.A. Cox, The Surface Science of Metal Oxides, Cambridge University Press, New York, 1994.

[12] I. Ahmed , S.-G. Eriksson, E. Ahlberg, C.S. Knee, H. Götlind, L.-G. Johansson,M. Karlsson , A. Matic , L. Börjesson. *Structural study and proton conductivity in Yb-doped BaZrO$_3$.* Solid State Ionics 178, 515 (2007).

[13] R. Khenata, M. Sahnoun, H. Baltache, M Rérat, A.H. Rashek, N. Illes, B. Bouhafs, *First-principle calculation of structural, electronic and optical properties of BaTiO$_3$ and Ba ZrO$_3$ under hydrostatic pressure"*, Solid state communications 136, 120 (2005).

[14] Hongwu Zhang, Xiaoyan Fu, Shuyun Niu, Qin Xin, *Synthesis and photoluminescence properties of Eu^{3+}-doped AZrO$_3$ (A = Ca, Sr, Ba) perovskite.* Journal of Alloys and Compounds, *In Press* (2007).

[15] Ling He, Yuhua Wang and Hui Gao, *Characterization of the VUV excitation spectrum of BaZr(BO$_3$):Eu^{3+}*, Journal of Luminescence 126, 182 (2007).

[16] J. E. Greedan *Rare Earth Elements and Materials* In *Encyclopedia of Physical Science & Technology, Vol. 12*, editor R. A. Meyers, Academic Press Inc., Orlando, chapter 1, pages 18-39 (1987).

[17] A. A. Kaplyanskii and P. P. Feofilov *The spectra of divalent rare earth ions in crystals of alkaline earth fluorides,* Opt. Spect. 13, 129 (1962).

[18] E. Loh, *Ultraviolet-absorption spectra of europium and ytterbium in alkaline earth fluorides* Phys. Rev. 84, 184 (1969).

[19] G. Burns, *Shielding and Crystal Fields at Rare-Earth Ions,* Phys. Rev. 128, 2121 (1962).

[20] D. K. Ray, *Investigations into the Origin of the Crystalline Electric Field Effects on Rare Earth Ions; II. Contributions from the Rare Earth Orbitals,* Proc. Phys. Soc. 82, 47 (1963).

[21] R. M. Sternheimer, *Shielding and Antishielding Effects for Various Ions and Atomic Systems* Phys. Rev. 146, 140 (1966).

[22] B. Henderson and G. Imbusch, *Optical Spectroscopy of Inorganic Solids* Clarendon Press, Oxford (1989).

[23] R. M. Sternheimer, *Shielding and Antishielding Effects for Various Ions and Atomic Systems,* Phys. Rev. 146, 140 (1966).

[24] P. Erdös and J. H. Kang, *Electronic Shielding of Pr^{3+} and Tm^{3+} in Crystals,* Phys. Rev. B 6, 3393 (1972).

[25] A. J. Freeman and R. E. Watson, *Theoretical Investigation of Some Magnetic and Spectroscopic Properties of Rare-Earth Ions,* Phys. Rev. 127, 2058 (1962).

[26] J. Blok and D. A. Shirley, *Systematic Variation of Quadrupole Crystal-Field Shielding in Rare- Earth Ethyl Sulfates, P*hys. Rev. 143, 278 (1965).

[27] D. K. Ray, *Investigations into the Origin of the Crystalline Electric Field Effects on Rare Earth Ions; II. Contributions from the Rare Earth Orbitals,* Proc. Phys. Soc. 82, 47 (1963).

[28] R. M. Sternheimer, *Shielding and Antishielding Effects for Various Ions and Atomic Systems,* Phys. Rev. 146, 140 (1966).

[29] P. Erdös and J. H. Kang, *Electronic Shielding of Pr^{3+} and Tm^{3+} in Crystals, P*hys. Rev. B 6, 3393 (1972).

[30] A. Ellens, *Electron-phonon coupling of lanthanide ions in solids,* Ph.D. thesis, Debye Institute, University of Utrecht (1996).

[31] A. Ellens, H. Andres, A. Meijerink and G. Blasse, *Spectral-line-broadening study of the trivalent lanthanide-ion series I. Line broadening as a probe of the electron-phonon coupling strength,* Phys. Rev. B 55, 173 (1997).

[32] A. Ellens, H. Andres, A. Meijerink and G. Blasse, *Spectral-line-broadening study of the trivalent lanthanide-ion series. II. The variation of the electron-phonon coupling strength through the series,* Phys. Rev. B 55, 180 (1997).

[33] C. Görller-Walrand and K. Binnemans, *Rationalization of crystal-field parametrization* In *Hanbbook on the Physics and Chemistry of Rare-Earths, Vol. 23,* editor K. A. Gschneider Jr. and L. Eyring, North-Holland, Amsterdam, chapter 155, pages 121–283 (1996).

[34] C. K. Jørgensen and R. Reisfeld, *Lasers and Excited States of Rare Earths* Springer, Berlin (1977).

[35] A. Messiah *Quantenmechanik*, Vol 2, Walter de Gruyter & Co., Berlin, third edition (1990).

[36] M. I. Bradbury and D. J. Newman *cited from tro01* Chem. Phys. Lett. 1, 44 (1967).

[37] V. V. Ovsyankin, *Spectroscopy of Collective States and Cooperative Transitions in Disordered Rare-Earth Activated Solids* In *Spectroscopy of Solids Containing Rare Earth Ions*, editor A. A. Kaplyanskii and R. M. Macfarlane, Elsevier Science Publishers B. V., chapter 7, pages 343–480 (1987).

[38] F. Varsanyi and G. H. Dieke, *Ion-pair resonance mechanism of energy transfer in rare earth crystal fluorescence* Phys. Rev. Lett. 7, 442 (1961).

[39] E. Nakazawa and S. Shionoya, *Cooperative Luminescence in YbPO$_4$* Phys. Rev. Lett. 25 (25), 1710 (1970).

[40] H. J. Schugar, E. I. Solomon, W. L. Cleveland and L. Goodman, *Simultaneous Pair Electronic Transitions in Yb$_2$O$_3$,* J. Am. Chem. Soc. 97, 6442 (1975).

[41] M. P. Hehlen and H. U. Güdel, *Optical spectroscopy of the dimer system Cs$_3$Yb$_2$Br$_9$,* J. Chem. Phys. 98, 1768 (1993).

[42] P. Goldner, F. Pellé and F. Auzel, *Theoretical evaluation of cooperative luminescence rate in YB^{3+}:CsCdBr$_3$ and comparison with experiment,* J. Lumin. 72-74, 901 (1997).

[43] P. Goldner, F. Pellé, D. Meichenin and F. Auzel, *Cooperative luminescence in ytterbium-doped CsCdBr$_3$,* J. Lumin. 71, 137 (1997).

[44] P. Kisliuk, N. C. Chang, P. L. Scott and M. H. L. Pryce, *Energy levels of Chromium Ion Pairs in Ruby,* Phys. Rev. 184, 367 (1969).

[45] R. Valiente, O. Wenger and H. U. Güdel, *New photon upconversion processes in Yb3+ doped CsMnCl$_3$ and RbMnCl$_3$,* Chem. Phys. Lett. 320, 639 (2000).

[46] S. Heer, M. Wermuth, K. Krämer and H. U. Güdel, *Upconversion excitation of Cr^{3+} emission in Y$_3$Ga O$_{12}$ codopedwith Cr^{3+} and Yb^{3+},* Chem. Phys. Lett. 334, 293 (2001).

[47] M. P. Hehlen and H. U. Güdel, *Optical spectroscopy of the dimer system Cs3$_3$ Yb$_2$ Br$_9$,* J. Chem. Phys. 98, 1768 (1993).

[48] P. Goldner, F. Pellé, D. Meichenin and F. Auzel, *Cooperative luminescence in ytterbium-doped CsCdBr$_3$,* J. Lumin. 71, 137 (1997).

[49] W. M. Yen, W. C. Scott and A. L. Schawlow, *Phonon-Induced Relaxation in Excited Optical States of Trivalent Praseodymium in LaF$_3$,* Phys. Rev. 136, A271 (1964).

[50] T. Kushida, *Linewidths and Thermal Shifts of Spectral Lines in Neodymium-Doped Yttrium Aluminum Garnet and Calcium Fluorophosphate,* Phys. Rev. 185, 500 (1969).

[51] T. Kushida and M. Kikuchi *R, R', and B Absorption and Phonon-Induced Relaxations in Ruby,* J. Phys. Soc. Japan 23, 1333 (1967).

[52] A. Ellens, H. Andres, A. Meijerink and G. Blasse, *Spectral-line-broadening study of the trivalent lanthanide-ion series I. Line broadening as a probe of the electron-phonon coupling strength,* Phys. Rev. B 55, 173 (1997).

[53] V. V. Ovsyankin, *Spectroscopy of Collective States and Cooperative Transitions in Disordered Rare-Earth Activated Solids* In *Spectroscopy of Solids Containing Rare Earth Ions*, editor A. A.Kaplyanskii and R. M. Macfarlane, Elsevier Science Publishers B. V., chapter 7, pages 343–480 (1987).

[54] H. Haken, *Quanten feld theorie des Festkörpers* Teubner, Stuttgart (1973).

[55] L. D. DeLoach, S. A. Payne, L. K. Smith,W. L. Kway andW. F. Krupke, *Laser and spectroscopic properties of $Sr_5(PO_4)_3F$:Yb,* J. Opt. Soc. Am. B 11, 269 (1994).

[56] Luptn, Schielke, Weigelt, Petermann and Fornasiero, Mix *Deutsche Patentanmeldung Nr. 197024653* (1997).

[57] O. L. Malta, *The Theory of Vibronic Transitions in Rare Earth Compounds,* J. Phys Chem. Solids 56, 1053 (1995).

[58] E. Mix, *Kristallzüchtung, Spektroskopie und Lasereigenschaften Yb-dotierter Sesquioxide,* Ph.D. thesis, Institute of Laser-Physics, University of Hamburg, Germany (1999).

[59] Volker Peter, *Growth and Spectroscopy of Ytterbium-Doped Sesquioxides,* Ph.D thesis, Hamburg, Germany (2001).

[60] A. Lupei, V. Lupei, C. Presura, V. N. Enaki and A. Petraru, *Electron-phonon coupling effects on Yb^{3+} spectra in several laser crystals,* J. Phys. Condens. Matter 11, 3769 (1999).

[61] E. Mix, "Kistallzuchtung*, Specktroskopie und Lasereigenschaften Yb-dotierter Sexquioxide*, Ph.D. Thesis, Institute of Laser Physics, University of Hamburg, Germany (1999).

[62] A. Einstein, *Strahlungs-Emission und -Absorption nach der Quantentheorie* Verhandl. der Deutschen Physikalischen Gesellschaft 13/14, 317 (1916).

[63] A. Einstein, *Zur Quantentheorie der Strahlung* Phys. Z. 18, 121 (1917).

[64] O. Svelto, *Priciples of Lasers,* Plenum Press, New York, third edition (1989).

[65] D. S. Sumida and T. Y. Fan, *Effect of radiation trapping an fluorescence lifetime and emission cross section measurements in solid-state laser media* Opt. Lett. 19, 1343 (1994).

[66] A. Bolz, *Energie transfer in Ytterbium-dotierten Sesquoxiden* Master's thesis, Institute of Laser-Physics, University of Hamburg, Germany (2001).

[67] H. W. Moos, *Spectroscopic relaxation processes of rare earth ions in crystals,* J. Lumin. 1-2, 106 (1970).

[68] B. Henderson and G. Imbusch, *Optical Spectroscopy of Inorganic Solids,* Clarendon Press, Oxford (1989).

[69] J. H. van Vleck, *The Puzzle of Rare Earth Spectra in Solids,* J. Phys. Chem. 41, 67 (1937).

[70] A. A. Kaminskii, *Laser Crystals; Their Physics and Properties,* Springer Verlag, second edition (1990).

[71] B. Judd, *Optical absorption intensities of rare-earth ions,* Phys. Rev. 127, 750 (1962).

[72] G. Ofelt, *Intensities of crystal spectra of rare-earth ions,* J. Chem. Phys. 37, 511 (1962).

[73] E. Mix, *Kristallzüchtung, Spektroskopie und Lasereigenschaften Yb-dotierter Sesquioxide,* Ph.D. thesis, Institute of Laser-Physics, University of Hamburg, Germany (1999).

[74] D. L. Dexter, *A Theory of Sensitized Luminescence in Solids,* J. Chem. Phys. 21, 836 (1953).

[75] T. Förster, *Zwischenmolekulare Energiewanderung und Fluoreszenz,* Annalen d. Phys. 2, 55 (1948).

[76] R. Reisfeld and C. K. Jørgensen, *Lasers and Excited States of Rare Earths* Inorganic Chemistry Concepts, Springer-Verlag (1977).

[77] L. F. Johnson and H. J. Guggenheim, *Infrared-Pumped Visible Laser,* Appl. Phys. Lett. 19, 44 (1971).

[78] Y. K. Voron'ko, V. V. Osiko and I. A. Shcherbakov, *Luminescence of Laser Crystals* Izvestiya Akademii Nuak SSR. Seria Fizicheskaya 46, 970 (1982).

[79] M. Yokota and O. Tanimoto, *Effects of diffusion on energy transfer by resonance,* J. Phys. Soc. Japan 22, 779 (1967).

[80] G. Burns, *Shielding and Crystal Fields at Rare-Earth Ions,* Phys. Rev. 128, 2121 (1962).

[81] V. Müller, *Characterisierung und Optimierung von hochdotierten Yb:YAG Laserkristallen,* Master's thesis, Institute of Laser-Physics, University of Hamburg, Germany (2001).

[82] Richard T. Weidner and Robert L. Sells, *Elementary Modern Physics*, Allyn and Bacon, Third edition, 1980.

[83] Neil W. Ashcroft and N. David Mermin, *Solid State Physics*, Holt Rinehart and Winston, 1976.

[84] Ludwing Reimer, *Scanning Electron Microscopy*, Springer Series in Optical Sciences, 1985.

[85] A. Ellens, H. Andres, A. Meijerink, G. Blasse, *Spectral line broadening study of the trivalent lanthanide ion series. I. Line broadening as a probe of the electron-phonon coupling strengh*, Phys. Rev. B 55, 173 (1997).

[86] P. C. Becker et al., *Observation of strong electron-phonon coupling effects in $YbPO_4$,* Phys. Rev. B 45, 5027 (1992).

[87] L. D. DeLoach, S. A. Payne, W. L. Kway, J. B. Tassano, S. N. Dixit, W. F. Krupke, *Vibrational structure in the emission spectra of Yb^{3+}-doped apatite crystals,* J. of Luminescence 62, 85 (1994).

[88] A. Lupei, G. Aka, E. Antic-Fidancev, B. Viana, D. Vivien, *Phonon effects in Yb^{3+} and Nd^{3+} spectra of GdCOB,* J. of Luminescence 94-95, 691 (2001).

Chapter 2: Synthesis, Structure and Morphology of BaZrO3:Yb^{3+} Microcrystals

2.1 BaZrO$_3$ Synthesis

Barium zirconate microparticles has been obtained by chemical methods such as oxidative precipitation, electrodeposition, hydrothermal, and sol-gel synthesis [1,2]. However, solution-based methods have allowed the synthesis of BZO particles with variations of the particle size that includes crystals from microns to nanometers [3,4,5]. The precipitation in solution and the hydrothermal synthesis has been successful in producing amorphus nanoparticles. During heat treatment, the nanoparticles can grow as microparticles or nanocrystalline agglomerations which produce particles in the range of microns. We carried out the hydrothermal process, since the principal advantage is the utilization of relatively low-cost equipment.

2.1.1 The Hydrothermal Process

The Yb^{3+} doped Barium Zirconate microparticles with concentrations of 0.1 mol%, 0.5 mol %, 1 mol%, 2.5 mol%, 5 mol% and 7.5 mol% were obtained by hydrothermal process. All reagents were analytically pure and used without further purification. Barium nitrate Ba(NO$_3$)$_2$, zirconyl chloride octahydrate $ZrOCl_8 \cdot 8H_2O$ and ytterbium nitrate $Yb(NO_3)_3 \cdot 5H_2O$ were used as the precursors materials. Sodium hydroxide (NaOH) was used as the precipitating agent. Cetyltrimethylammonium bromide (CTAB, CH$_3$(CH$_2$)$_{15}$N(CH$_3$)$_3$Br) was the surfactant and ethanol was the cosurfactant. In a typical procedure, see Figure 2.1.1.1, barium nitrate (4.53g), zirconyl chloride (5.58g), ytterbium nitrate (0.32g) and CTAB (cetyltrimethylammonium bromide) (1.9g) were dissolved in a solution of ethanol-water(CH$_3$CH$_2$OH,H$_2$O) at room temperature applying vigorous stirring for 1 h. Under strong stirring, sodium hydroxide was added and stirred again for 1h at room temperature. The hydrothermal reactions were carried out in a Teflon bottle (250 ml in total capacity) under autogenous

pressure at 100°C for 24h. The precipitate was then washed with distilled water and dried in a furnace at 100°C for 15h. Later, different annealing treatments were done in order to study the annealing temperature effects on the optical and morphological properties of BZO.
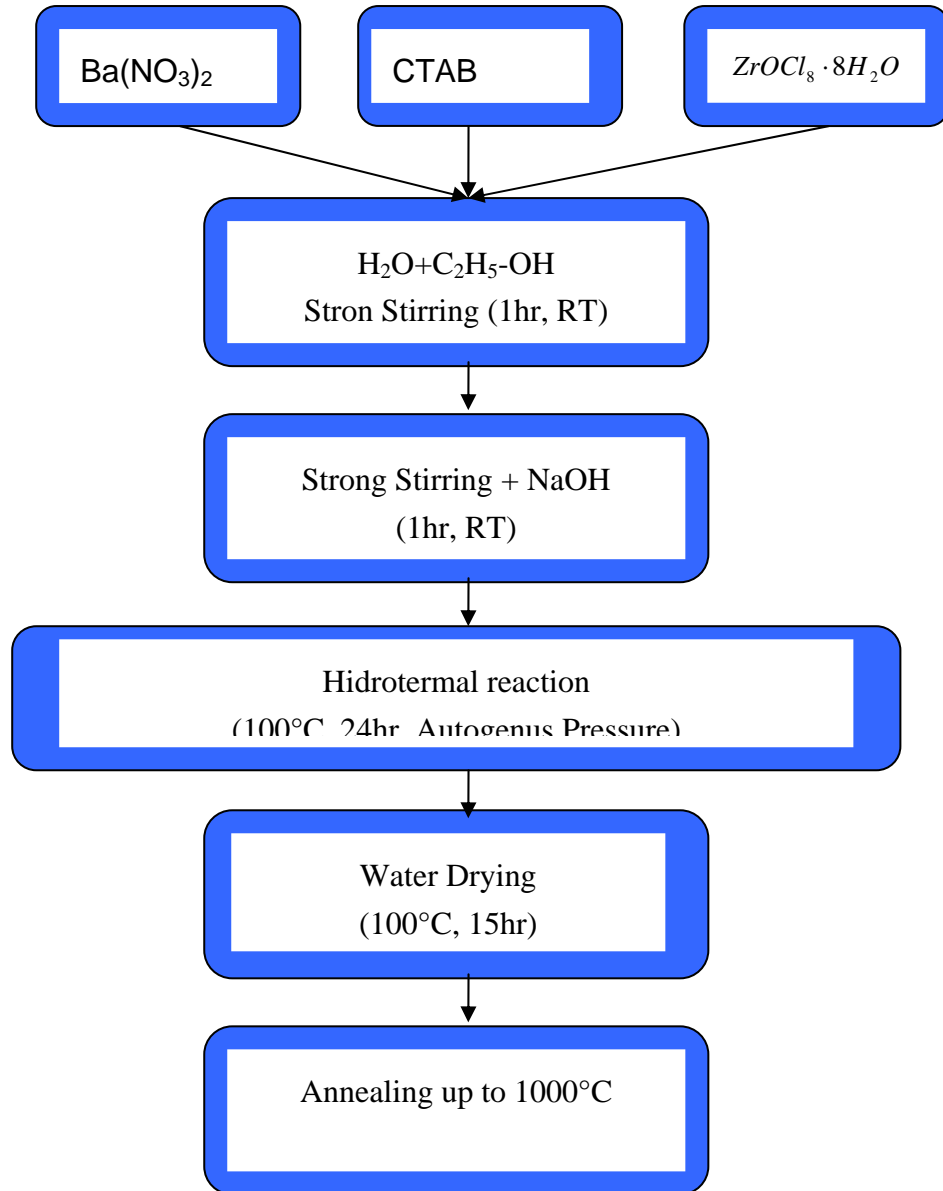

Figure 2.1.1.1: Hydrotermal synthesis to obtain BZO microcrystals.

2.2 Structural Characterization

2.2.1 XRD Measurement

In order to investigate the crystalline structure and the crystallite size of BZO samples, X-Ray Diffraction was obtained with a SIEMENS D-500 diffractometer equipment provided with a Cu-K tube with α radiation at 1.5426 Å, scanning in the interval from 20° to 70° for 2θ with increments of 0.02° and swept time of 8 s.

2.2.2 XRD Results and Discussion

The XRD patterns of BZO samples annealed at 1000°C with concentrations of 0% mol, 0.1% mol, 0.5% mol, 1% mol, 2.5% mol, 5% mol and 7.5% mol are shown in Figure 2.2.2.1. The main characteristic peaks (30.13°, 37.12°, 43.12°, 53.5°, 62.44°) are in correspondence with 6-0399 standard JCPDS for pure cubic perovskite $BaZrO_3$ with a lattice constant of 4.18°A. If the diffraction patterns of each Yb doped $BaZrO_3$ are compared with undoped $BaZrO_3$ annealed at 1000°C, we do not observe measurable changes. This confirms the high structural stability of the cubic phase for BZO with doping concentrations up to 5% mol. However, we observe in Figure 2.2.2.1 additional peaks corresponding to (4,0,0), (4,4,0) and (6,2,2) planes of Yb_2O_3 with cubic structure, according to pdf 41-116 [6]. This phase segregation corresponds to concentration of 7.5% mol as indicated by dash arrows.
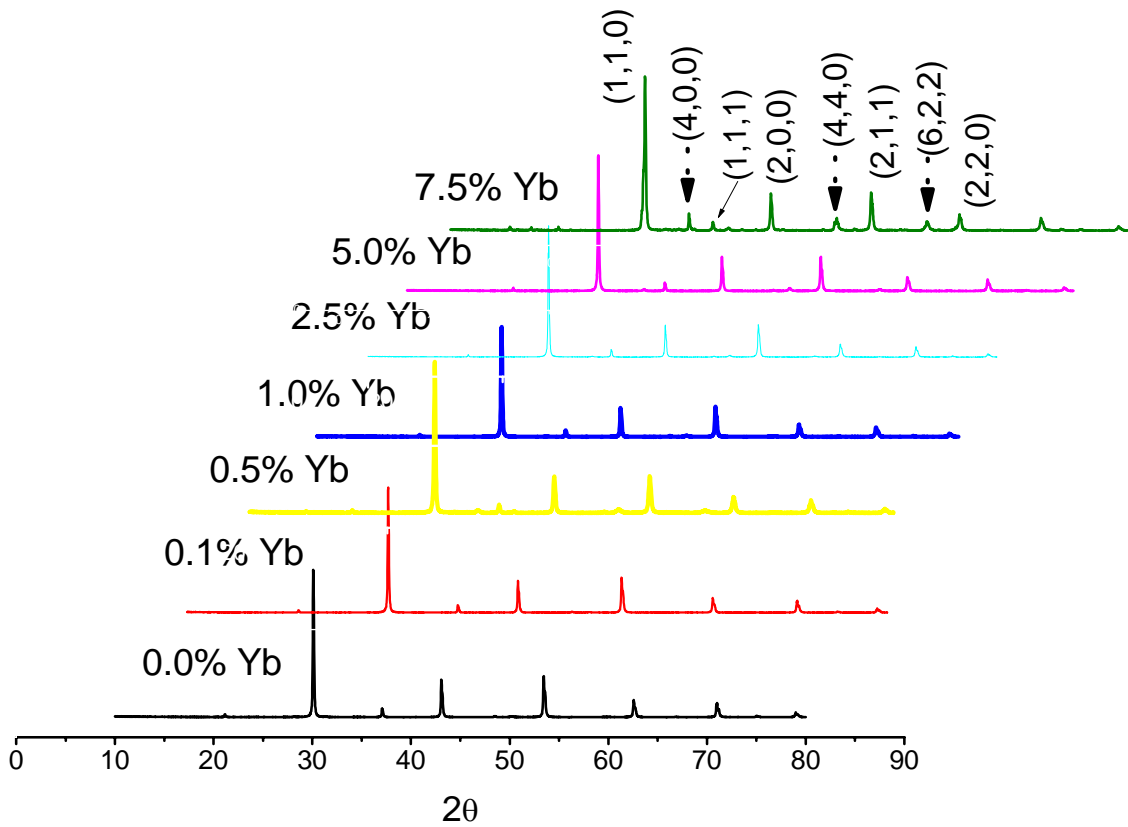
Figure 2.2.2.1: X-Ray Diffraction patterns of Yb³⁺ doped BaZrO₃ samples annealed at 1000°C . The patterns correspond to undoped sample and samples doped with concentration at 0.1% mol, 0.5% mol, 1% mol,2.5% mol 5% mol and 7.5 % mol.

The phase composition for BZO:Yb³⁺ (7.5%) was estimated by using the following equation [7]:

$$C_c = \frac{I_c(1,1,0) + I_c(1,1,1)}{I_c(1,1,0) + I_c(1,1,1) + I_{cYb}(4,0,0)}$$ (2.1)

Where C an CYb refer to the cubic phase for BZO and Yb₂O₃ respectively. *I* indicates the integrated intensity of each peak. Thus, the cubic phase content for BZO is 92% and the remaining 8% is for Yb₂O₃.

If we compare the XRD pattern of undoped BZO sample annealed at 100°C with that of undoped BZO annealed at 1000°C, there is no change in the

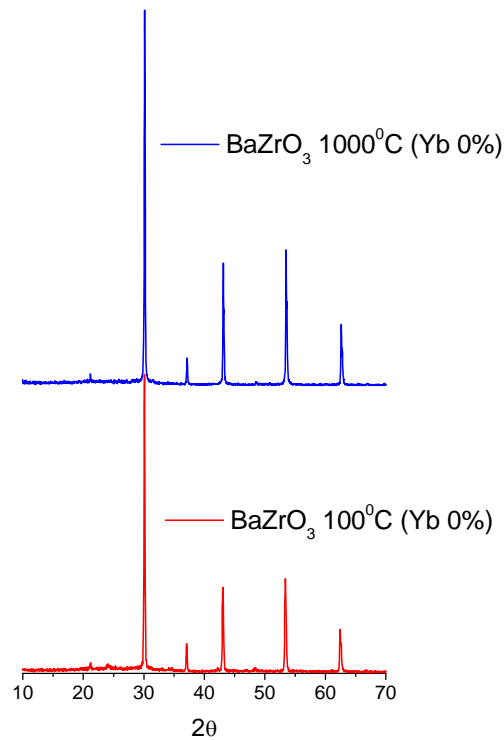peaks, see Figure 2.2.2.2. Hence, the cubic structure is maintained in spite of the increased temperature.

Figure 2.2.2.2: X-Ray Diffraction patterns of undoped BaZrO₃ samples annealed at 100°C and 1000°C .

2.3 Morphology

2.3.1 SEM Measurement

Scanning Electron Microscopy (SEM) was performed in an environmental scanning electron microscope XL30 which has attached a X-ray energy dispersive spectroscope (EDS).

2.3.2 SEM Results and Discussion

SEM images for Yb^{3+} doped Barium Zirconate for all concentrations were obtained and are shown in Figure 2.3.2.1. These images depict BZO:Yb^{3+} well-defined micron sized BZO crystallites with cubic morphology. Detailed analysis

of each single cube indicates the presence of single crystals and crystals composed of several primary particles. This mixture suggests that the growth mechanism is based on the coalescence of individual nanocrystals. When the doping concentration oscilates between 0.1% mol and 1% mol, cubic morphology as well as defined crystallites are observed, see Figure 2.3.2.1 a, b and c. However, from doping concentration between 2.5% mol and 7.5% mol the cubic morphology dissapears and the degradation in crystallites is clear. In addition, it is noticeable how the segregation occurring in crystallites with high doping concentration is detrimental for emission of microcrystallites, as we will see in the next chapter 3.

It is possible to obtain the average size of crystallites showed in Figure 2.3.2.1 taking into account the lateral side length of cubes. The best cubic crystallites are observed in SEM image for the lowest concentration of Yb^{3+} (0.1% mol) and the average computed particle size was $1.6\,\mu m$ for the single isolated particles. In addition, the image of Yb doped BZO crystallites (0.1%mol) annealed at 100°C (Figure 2.3.2.2), was compared with the SEM image of the sample annealed at 1000°C to observe changes in morphology. It was found that the annealing temperature does not affect the structure of BZO perovskite cubes.
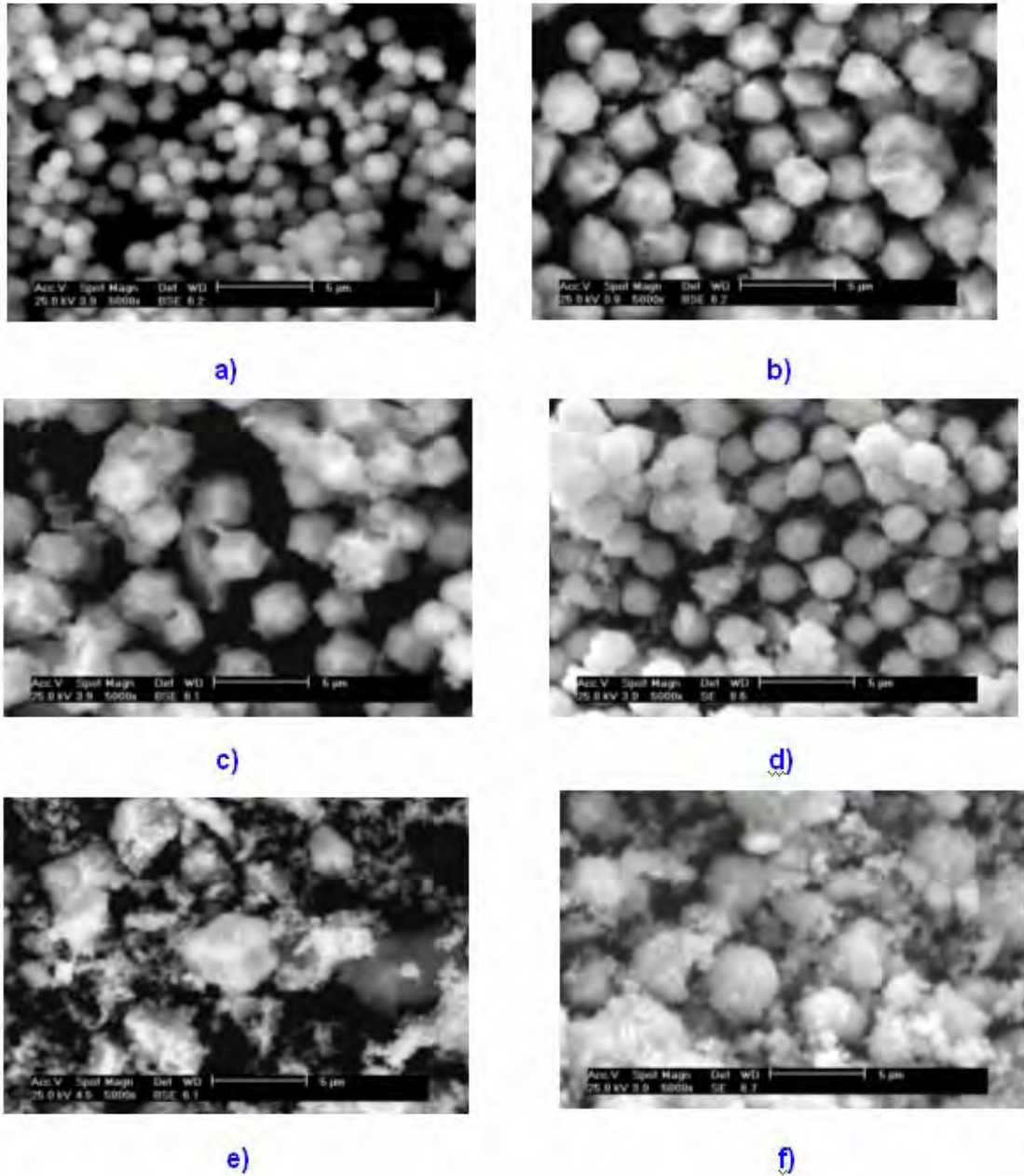
Figure 2.3.2.1: SEM images for Yb doped BaZrO₃ samples annealed at 1000°C; a) on the left top corner BZO:Yb^{3+} (0.1%), b) BZO:Yb^{3+} (0.5%), c) BZO:Yb^{3+} (1%), d) BZO:Yb^{3+} (2.5t%), e) BZO:Yb^{3+} (5%) and f) on the right bottom coner: BZO:Yb^{3+} (7.5%).
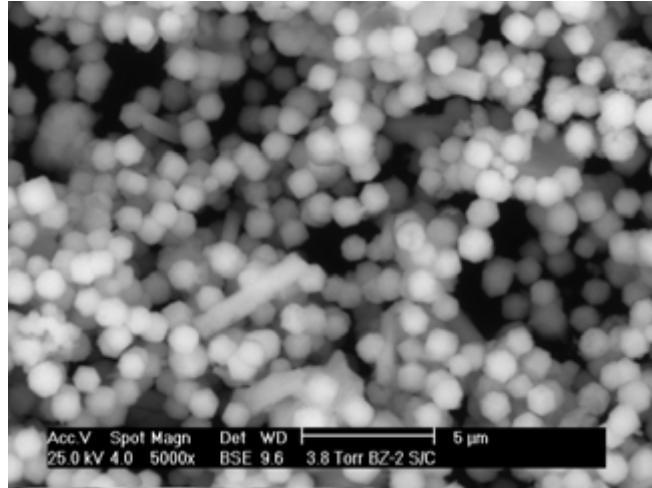
Figure 2.3.2.2: SEM image for BZO:Yb^{3+} 0.1at%. sample annealed at 100°C

2.4 Infra-Red Fourier Spectroscopy

2.4.1 Infra-Red Fourier Spectroscopy Measurement

In order to know the phonon spectrum, Fourier transform spectroscopy was made by means of the Perkin Elmer Spectrum BX FT-IR System in the range of 350 to 1000 cm^{-1}, using the ATR method. The samples (powder) were deposited onto a zinc selenure window (ZnSe) and excited by a laser He-Ne.

2.4.2 Infra-Red Fourier Spectroscopy Results and Discussion

Figure 2.4.2.1 shows the infrared absorption spectra for BZO:Yb^{3+} (2.5%) sample and undoped sample annealed at 1000°C. It is observed that both, the doped and undoped samples present the same absorption peaks. The peak at about 590 cm^{-1} corresponds to the observed maximum phonon energy. Thus, it is believed that phonon energy of BZO might be around 590 cm^{-1} The peak centered at 551cm^{-1} is attributed to the stretching vibration of Zr-O [8]. Vibrational modes corresponding to impurities as OH^{-} and residual H$_2$O were not detected.
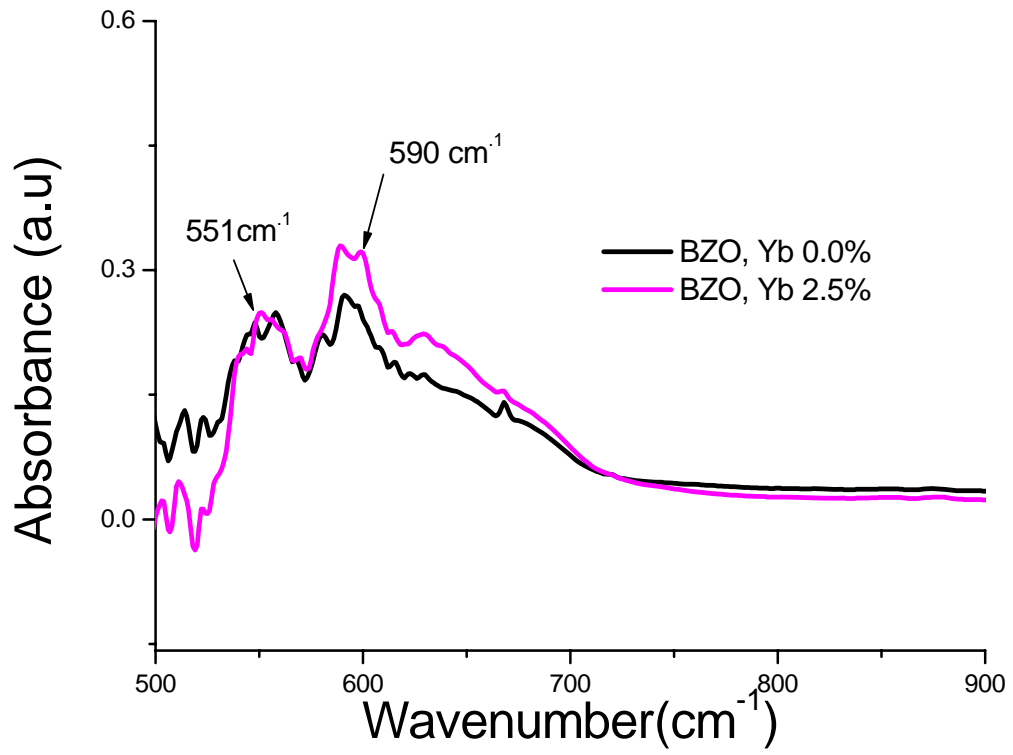
Figure 2.3.3.1: Infrared absorption espectra for BZO:Yb^{3+} doped and undoped sample annealed at 1000°C

2.5 References

[1] F. Boschini, B. Robertz, A. Rulmont, and R. Cloots, *Preparation of nanosized barium zirconate powder by thermal decomposition of urea in an aqueous solution containing barium and zirconium, and by calcination of the precipitate,* Journal of the European Ceramic Society 23, 3035 (2003).

[2] Keith J. Leonard, Srivatsan Sathyamurthy, and M. Parans Paranthaman, *Characterization of BaZrO3 nanoparticles prepared by reverse micelle synthesis,* Chemistry of materials 17, 4010 (2005).

[3] Z. Lu, Y. Tang, L. Chen, and Y. Li, *Shape-controlled synthesis and characterization of BaZrO3 microcrystals*, J. Cryst. Growth 266, 539 (2004).

[4] M. Veith, S. Mathur, N. Lecerf, V. Huch, T. Decker, H. P. Beck, W. Eiser, and Haberkorn, *Sol-gel synthesis of nano-scaled BaTiO3, BaZrO3 and BaTiO.5Zr0.5O3 oxides via single-source alkoxide precursors and semi-alkoxide routes,* J. Sol-Gel Sci. Technol. 15, 145 (2000).

[5] B. Guillaume, F. Boschini, I. Garcia-Cano, A. Rulmont, R. Cloots, and M. Ausloos, *Optimization of BaZrO$_3$ sintering by control of the initial powder size distribution; a factorial design statistical analysis*, Journal of the European Ceramic Society 25, 3593 (2005).

[6] H.M. Wang, M.C. Simmonds, J.M. Rodenburg, *Manufacturing of YbAG coatings and crystallisation of the pure and Li$_2$O-doped Yb$_2$O$_3$–Al$_2$O$_3$ system by a modified sol–gel method,* Materials Chemistry and Physics 77, 802(2002).

[7] R.C. Garvie *Occurrence of Metastable Tetragonal Zirconia as a Crystallite Size Effect, J. Phys. Chem. 69*, 1238 (1965).

[8] A. A. Athawale, A. J. Chandwadkar, P. Karandikar, R. Pasrich, M. S. Bapat, *Radiation assisted synthesis of nanosized barium zirconate*, Radiation Physics and Chemistry 75, 755 (2006).

Chapter 3: Optical Spectroscopy

3.1 Absorption Spectroscopy

3.1.1 Absorption Spectroscopy Procedure

The optical absorption spectra (reflectance mode) were measured with a Perkin-Elmer UV-VIS-NIR Lambda 900 spectrophotometer using a 1.5 in. integrating sphere (Labsphere Co). The measured wavelength range goes from 200 nm to 2000 nm. Since the samples are powder, a reflection spectra directly obtained was converted into absorption spectra using spectrophotometer software.

3.1.2 Absorption Spectroscopy Results For $BaZrO_3$:Yb^{3+} annealed at 100^oC

The difference between doped and undoped BZO absorption espectra for all concentrations of dopant are shown in Figure 3.1.2.1. They correspond to samples annealed at 100°C. The NIR absorption band peaking at 973 nm corresponding to Yb^{3+} ion increases with concentration. This absorption band corresponds to $^2F_{7/2} \rightarrow {}^2F_{5/2}$ transition around 10000 cm^{-1}. All samples present an UV absorption edge with two bands centered at 217 nm and 300 nm. The former corresponds to absorption of lattice, because this band also appears in the undoped sample. The 300 nm band corresponds to the superposition of F color centers (one or two electrons trapped in an oxygen vacancy) and Oxygen vacancies [1]. On the other hand, these bands do not change in position with concentration of Yb ion. This fact is in agreement with the XRD results showed in chapter 2, since the lattice does not show measurable changes despite the increase of Yb concentration. In other words, the structure and symmetry is maintained.
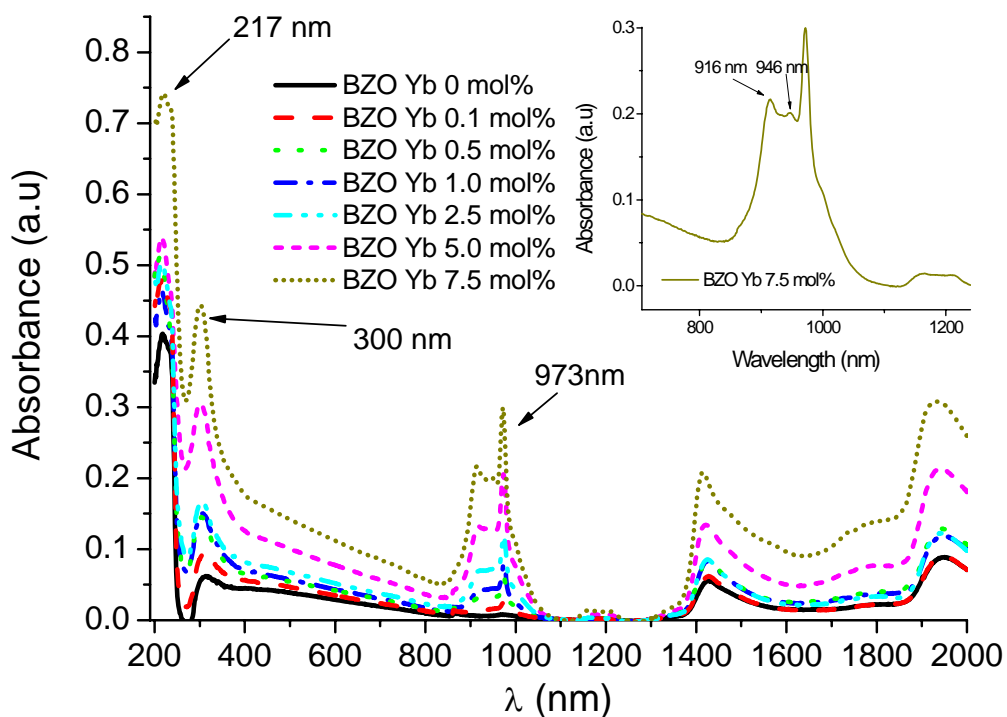
Figure 3.1.2.1: Absorption spectra of BaZrO$_3$:Yb^{+3} annealed at 100 °C.

The broad absorption band with main peaks around 916 nm, 942 nm and 973 nm corresponds to transitions from the lowest stark level of the multiplet $^2F_{7/2}$ to stark levels of the $^2F_{5/2}$ excited state multiplet of Yb^{3+}, see Inset in Figure 3.1.2.1. These peaks are in agreement with previous reported spectra in different host [2,3,4]. These absorption peaks corresponding to single Yb^{3+} were used to obtain the position of the split energy levels as depicted in the classical Dieke diagram, see Figure 3.1.2.2.
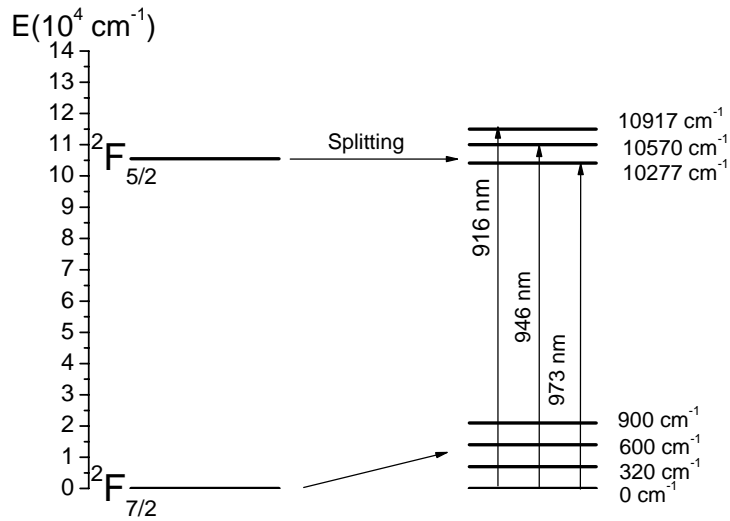
Figure 3.1.2.2: Yb^{3+} Energy diagram for absorption in samples annealed at 100°C. Splitting and wavelength values are aproximates values used for reference.

3.1.3 Absorption Spectroscopy Results For BaZrO$_3$:Yb^{3+} annealed at 1000°C

Figure 3.1.3.1 shows the samples annealed at 1000°C which also present the $^2F_{7/2} \rightarrow {}^2F_{7/2}$ transition. The 973 nm absorption band increases with Yb concentration. In addition, absorption shoulders centered at 423 nm are observed in the region between 400 nm and 800 nm. We suspect that such shoulders are consequence of the annealing treatment and indicate the possible reduction of Yb^{3+} to Yb^{2+}, as will be explained in chapter 4. These shoulders are not present in the samples annealed at 100°C. Furthermore, the doped samples annealed at 1000°C present a particular peak at 239 nm. This peak can be associated to the band gap of BZO, with a value of 5.18 eV. Both, samples annealed at 100°C and samples annealed at 1000°C, present a central peak at 1382 nm, indicating the possible presence of residual H₂O that remains within the BaZrO₃ crystallites.
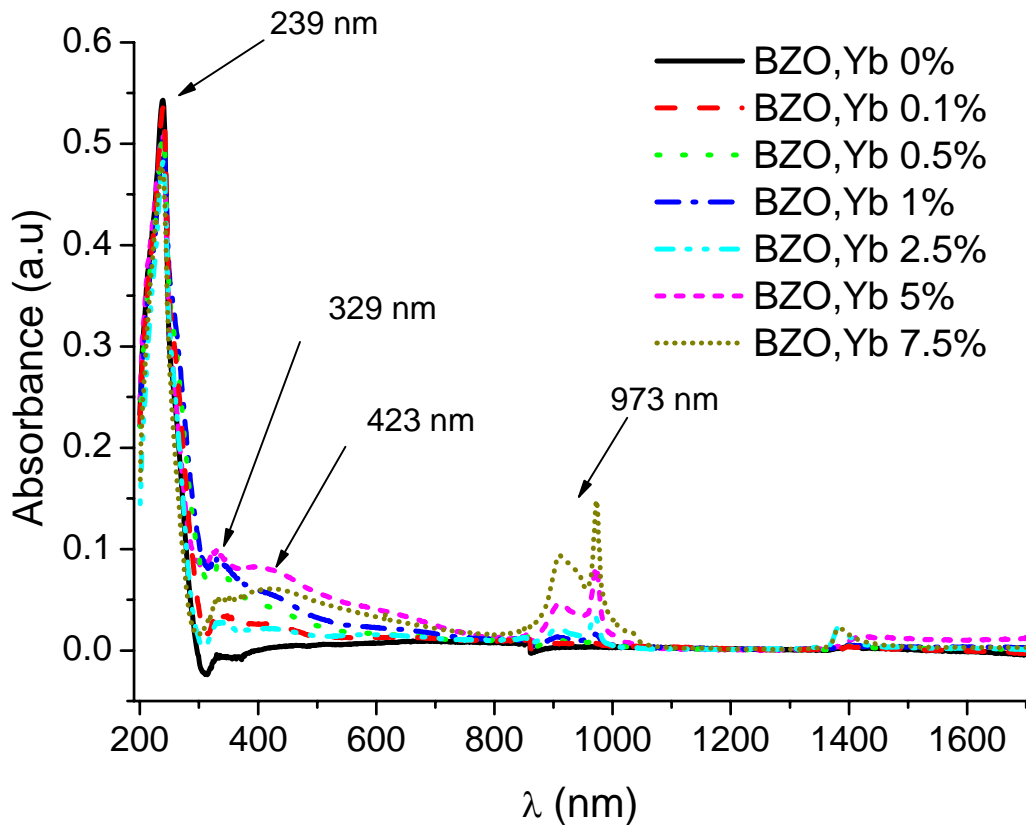
Figure 3.1.3.1: Absorption spectra of BaZrO₃:Yb^{+3} annealed at 1000 °C.

After annealing at 1000°C, it is noticeable that the two bands centered at 217 nm and 300 nm in the UV edge for samples annealed at 100°C undergo a shifting to 239 nm and 329 nm respectively. When the temperature increases, crystallites increase its size, producing an elargement in bondings and cell parameters. Therefore, the host absorption might change.

During the absorption spectroscopy measurements, it was never found the presence of other rare earth impurities. Special attention was dedicated to Er^{3+} absorption bands whose main absorption peaks are located at 522 nm and 653 nm which have been reported in other hosts [5], none of these bands were observed in the absorption spectra. This fact is interesting since the RE elements, in spite of the high purity precursor employed (99.99%), are indeed chemically related. It is difficult to separate them from each other, then, impurities of other RE are inevitable.

3.1.4 Cooperative Absorption in BaZrO$_3$ Matrix

The VIS broad absorption band centered at 423 nm in samples annealed at 1000^{0}C, could be the result of the simultaneous absorption of a pair of Yb ions an is named cooperative absorption. This broad band is nearly the double energy (half-wavelength) of the NIR absorption band.

Figure 3.1.4.1 shows the absorption espectra for the BaZrO$_3$:Yb (7.5%) calcinated sample. Curve (a) corresponding to the VIS absorption, has been scaled by a factor of 2 to make it comparable with the self-convolution of the IR absorption band shown in figure (b). It is observed that the cooperative absorption spectra does not coincide with the self-convolution, $\int f_{IR}(\nu) f_{IR}(E-\nu) d\nu$ of the NIR absorption, $f_{IR}(\nu)$, depicted by curve (b) [6-8].
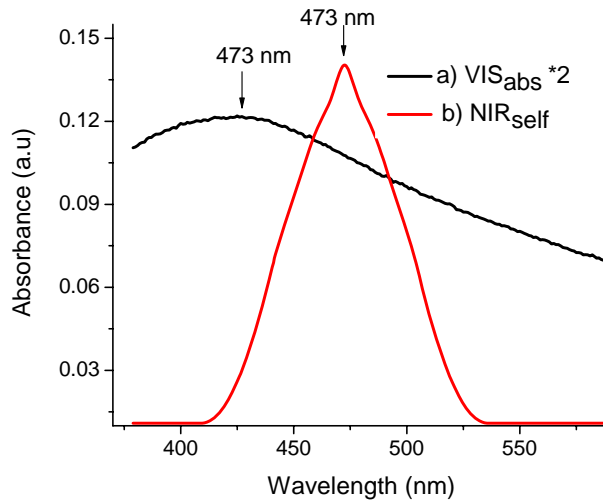
Figure 3.1.4.1: Absorption of Yb^{3+} ions in BaZrO$_3$:Yb^{3+} (7.5%) annealed at 1000^{0}C, (a), cooperative absorption of Yb^{3+} pairs, (b) self-convolution of IR absorption spectrum.

However, cooperative absorption is present because emission of cooperative pairs was observed. Probably, cooperative absorption is masked due to the overlap between the absorption bands of F color centers and Yb^{2+} in the UV-VIS range, as will be explained in chapter 4. It is worth to notice that no other bands related to impurities of RE or transitions metal ions were observed in the visible region.

3.2 Emission Spectroscopy

3.2.1 Emission Spectroscopy Procedure

The upconversion spectra were obtained with a conventional set up [9,10], see Figure 3.2.1.1. The NIR emission spectra were obtained under 920 nm excitation with a 10 ns pulsed tunable Optical Parametric Oscillator (MOPO from Spectra Physics) pumped by the third harmonic of Nd: YAG pulsed laser. The fluorescence emission was analyzed with an Acton Pro 500i monochromator, a R955 Hamamatsu photomultiplier tube for visible emission and InGaAs photodetector for NIR emission connected to SR830 (Stanford Research Systems) mode-locking amplifier. The VIS emission spectra were recorded exciting at 967 nm with a Laser Diode. The system was controlled with a PC where the emission spectra was displayed and recorded. All photoluminescence measurements were done at room temperature, and the samples were put in 1 mm diameter capillary tube to guarantee the same volume of excited material. The alignment of the set up was carefully maintained in order to compare the intensity of the up-converted signal between different samples. The decay time curves were obtained using a Lecroy oscilloscope.
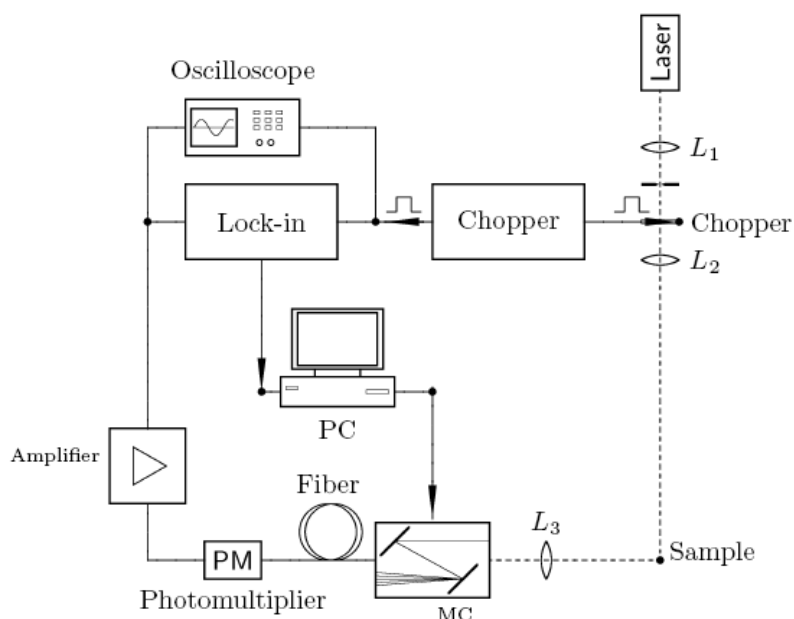

Figure 3.2.1.1: Experimental setup for cooperative up conversion emission spectroscopy.

3.2.2 Emission Spectroscopy Results for BaZrO$_3$:Yb^{3+}

Ytterbium doped BZO samples annealed at 1000°C present visible emission, which has been observed by the naked eye. On the other hand, emission of samples annealed at 100°C was not observed or at least was not detected by our detection system. In this case, it is assumed that the emission is quenched due the high concentration of residual OH$^-$ ions from the synthesis method, as is depicted in the FTIR spectra of sample annealed at 100°C, see Figure 4.3.3.1.

3.2.2.1 Infrared Emision of samples annealed at 1000°C

Figure 3.2.2.1.1 shows the near-infrared emission spectra for all BZO:Yb^{3+} samples under excitation at 920 nm. The spectra illustrates two bands centered at 973 nm and 1038 nm, which are associated with the transitions from the upper Stark energy level of the excited state $^2F_{5/2}$ to the lowest stark levels of the ground state $^2F_{7/2}$.
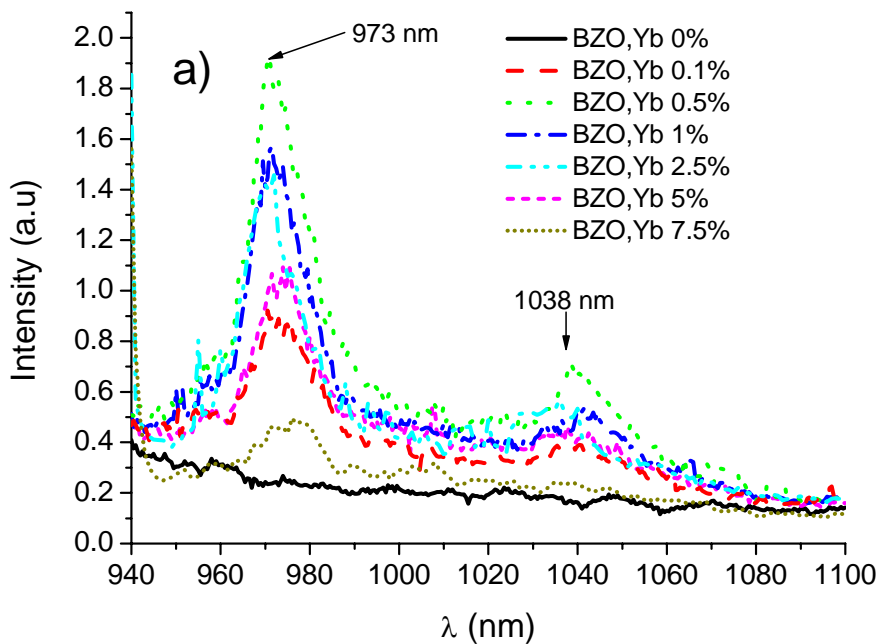

Figure 3.2.2.1.1: a)Near infrared emission Spectrum associated with the $^2F_{5/2} \rightarrow ^2F_{7/2}$ transition of Yb ion (samples annealed at 1000°C).

3.2.2.2 Visible Emision of samples annealed at 1000°C

The emission spectra in the visible range, after excitation at 967 nm and 920 nm of BaZrO$_3$:Yb^{3+} (2.5%) sample are shown in figure 3.2.2.2.1. All emission peaks and Intensity of bands are reproduced despite the different excitation wavelength. However, the emission of samples excited at 920 nm are noisy. Thus, we decided to record VIS espectra under 967 nm as excitation wavelength to obtain a well defined spectra. All VIS emission spectra under 967 nm excitation of several concentrations of Yb are shown in Figure 3.2.2.2.2. A blue-green emission was observed by the naked eye. The best VIS emission was presented by the BZO:Yb (2.5%) sample.
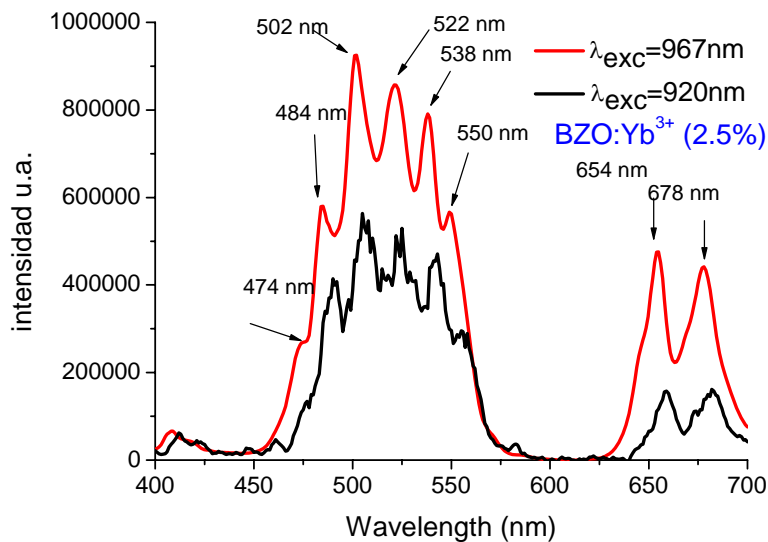

Figure 3.2.2.2.1: Cooperative emission of BaZrO$_3$:Yb^{3+} (2.5%) and up-conversion emission of Er^{3+} and Tm^{3+} traces sensitized with Yb^{3+} ion.
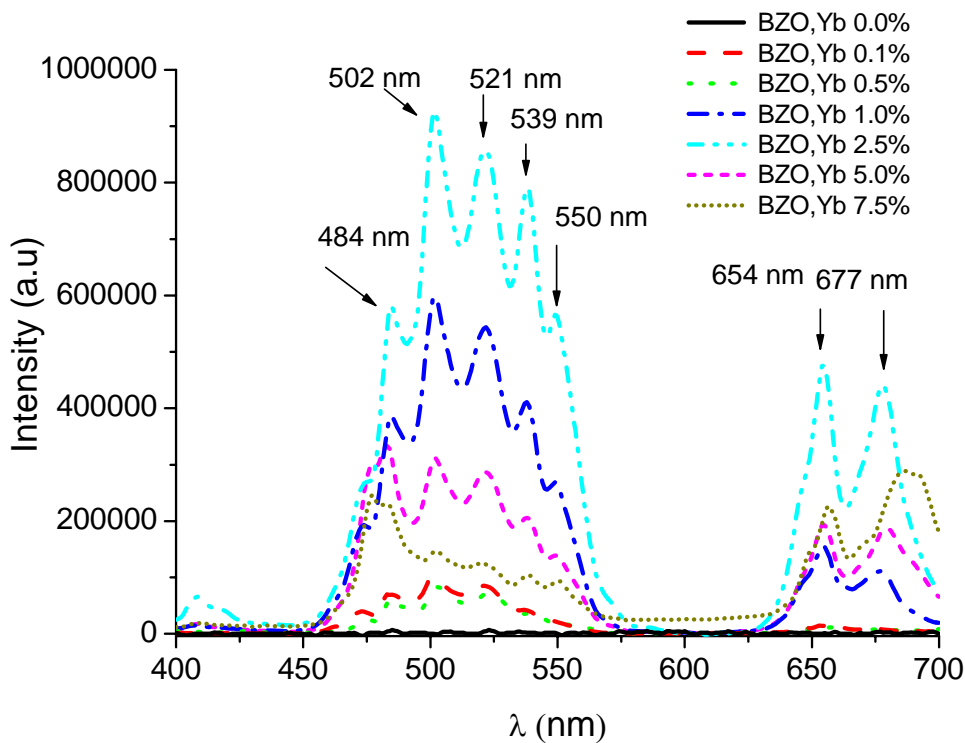
Figure 3.2.2.2.2: Cooperative emission of BaZrO$_3$:Yb^{3+} and up-conversion emission for traces of Er^{3+} and Tm^{3+} (samples annealed at 1000°C).

Eight peaks are observed in the emission spectra of BZO:Yb^{3+} samples annealed at 1000°C, 474 nm (shoulder), 484 nm, 502 nm, 522 nm, 538 nm, 550 nm (shoulder), 654 nm and 678 nm, see Figure 3.2.2.2.2. The peak in 484 nm almost matches at twice the energy of the infrared emission peak at 973 nm and similarly, the peak in 502 nm almost matches at twice the energy of the NIR emission peak at 1038 nm. The rest of peaks correspond to Er^{3+} and Tm^{3+} impurities emissions as we wil discuss later. Thus, these peaks can be in principle, associated with cooperative emission which consists in the simultaneous annihilation of two excited states of two Yb^{3+} interacting ions, resulting in the emission of a single photon with energy equal to the sum of the energies of the excited ions. This kind of emission is also called cooperative up-conversion emission (CUC).

To verify that 484 nm and 502 nm peaks correspond to cooperative emission. It was simulated the self-convolution of the BZO:Yb^{3+} (0.5%) sample that presented the best NIR emission by using the following expression [11]:

$$I_{CL}(E) = \int I_{IR}(E')I_{IR}(E - E')dE' \qquad (3.1)$$

According to self-convolution of NIR emission of BZO:Yb^{3+} (0.5%) sample calculated in Figure 3.2.2.2.3, the cooperative emission peaks at 502 nm and 485 nm showed in VIS emission spectra are perfectly reproduced in self-convolution, indicating that either involves a two photon process. The peak at 518 nm is slightly shifted to the left in comparison with the 524 nm peak.
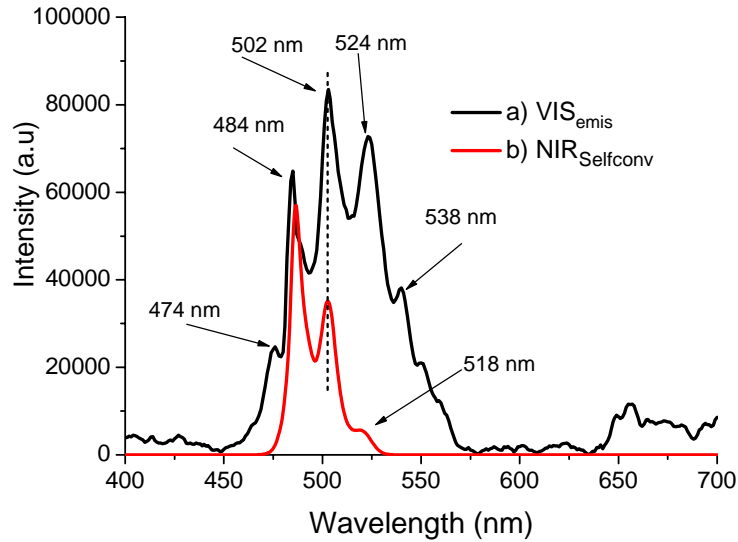
Figure 3.2.2.2.3: Emission spectra of BaZrO$_3$:Yb^{3+} (0.5%) at room temperature; (a) Cooperative luminescence spectrum, (b) self-convolution of the near-infrared emission spectrum.

The transition of the cooperative emission of Yb at 502 nm is described by the expression: $^2F_{5/2} + {}^2F_{5/2} \rightarrow {}^2F_{7/2} + {}^2F_{7/2} + h\upsilon$. The same peak of cooperative emission has been observed by Malinowski et al. in Yb doped YAG fibers [4], where the splitting of the excited and ground state are taken into account.

The observed visible luminescence is not completely originated by the cooperative emission between Yb^{3+} ions because of the presence of undesirable rare earth ions impurities in the precursor materials. Those impurities have energy levels around 20000 cm^{-1} (500 nm) that also give place to emission in the blue-green region. The most probable impurities are erbium and thulium. Thus, the emissions in the visible range may result from energy transfer transitions between Yb^{3+} and Er^{3+} or between Yb^{3+} and Tm^{3+}. Such emissions can even mask the cooperative luminescence if the impurity concentrations are high enough. We must emphasize that such impurities do not show detectable emission when we excited directly in the UV-VIS range. So it is likely that their emissions are basically due to the energy transfer from the Yb ions.

The emissions located at 522 nm, 538 nm and 550 nm (Figure 3.2.2.2.2) are characteristic of the $^{2}H_{11/2}+^{4}S_{3/2} \rightarrow ^{4}I_{15/2}$ transition of Er^{3+} ion due to the energy transfer from Yb^{3+} to Er^{3+} ion and is similar to the emission obtained in the systems ZrO_2:Yb^{3+}-Er^{3+} and $BaZrO_3$:Yb^{3+}-Er^{3+} [12,13]. The 654 nm main peak in the red band is characteristic of $^{4}F_{9/2} \rightarrow ^{4}I_{15/2}$ transition for Er^{3+}. In addition, thulium emission peak at 474 nm corresponds to the transition $^{1}G_{4} \rightarrow ^{3}H_{6}$, see Figure 3.2.2.2.4. On the other hand, it has been reported undesirable emission of Tm^{3+} at 484 nm in systems such as $Y_3Al_5O_{12}$, and GGG [14]. Therefore, we don't rule out a possible overlapping between cooperative emission of Yb and Tm emission, since it was not synthetized and characterized BZO:Tm^{3+} to found emission peaks of Tm in BZO. Because of the presence of Tm^{3+} and Er^{3+} impurities was not detected in the absorption spectra, it has to be very low concentration. The strong intensity of all peaks is interesting considering the very small concentration. This fact suggests very efficient upconversion processes involving traces of Tm^{3+} and Er^{3+} ions having the Yb^{3+} ions as sensitizers.
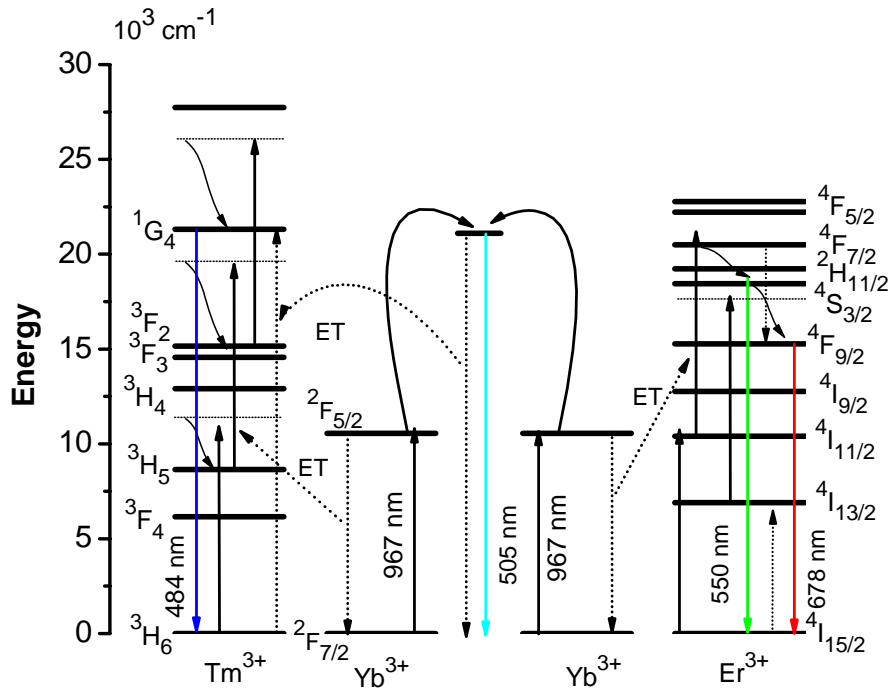
Figure 3.2.2.2.4: Energy level diagram where the proposed mechanism for up-conversion cooperative emission of Yb^{3+} and up-conversion mechanism of Er^{3+} are described [15].

In order to elucidate the mechanism of the Yb^{3+} ion to produce the cooperative emission and the upconversion emission of Er and Tm impurities, the dependence of the up-converted integrated intensity (I_{UPC}) was analyzed as function of the pumping intensity (I_{PUMP}). It is well-know that this dependence is expressed by the equation $I_{UPC} = K \cdot I_{PUMP}^n$, where n denotes the number of photons absorbed to produce upconversion emission and K is a constant.

Figure 3.2.2.2.5 shows the behavior of the emission Intensity versus the pump power for the VIS emission bands. The cooperative upconversion of the green band of Er in $BaZrO_3$:Yb^{3+} (0.5%) and $BaZrO_3$:Yb^{3+} (2.5%) are showed in Figure 3.2.2.2.5a. Considering the 0.5% doped sample, the slope was n= 1.88 indicating that a two-photon absorption process is present. However the value of n=1.33 for the 2.5 mol% sample, indicates that additional processes are present. From the energy diagram in Figure 3.2.2.2.4, it can be seen that electrons in $^4I_{11/2}$ level gain one exciting photon by ET among neighboring ions,

promoting one electron to $^4F_{7/2}$ that relaxes to the mixed level $^4H_{11/2}+^4S_{3/2}$, producing the green emission band. Part of this population decays nonradiatively to the $^4F_{9/2}$ level that in turn decays to produce the red emission band. Therefore, one can expect n to be lower than two.

The $^4F_{9/2}$ level is populated by electrons coming from de mixed $^4H_{11/2}+^4S_{3/2}$ levels, then the red emission band must also be a two photon absorption process; it means n=2. However, for the red band the values of n are 1.5 and 1.4 for dopant concentrations of 0.5%mol and 2.5%mol, respectively. These values indicate that energy loss is present, because of the non radiative transitions promote electrons from mixed $^4H_{11/2}+^4S_{3/2}$ levels to the $^4F_{9/2}$ state, which relaxes to the ground state emiting one red photon, see Figure 3.2.2.2.5b.

It has been reported that blue emission of Tm^{3+} involves three photons for upconversion as tipycally observed in systems such as oxyfluoride glasses and KYW:Yb^{3+},Tm^{3+} [16, 17]. However, Figure 3.2.2.2.5c shows that the blue emission requires the absorption of two photons. A possibility to explain this process of two photons, is the energy transfer directly between the cooperative level of Yb^{3+} pairs and the $^1G_4$ level of Tm^{3+} which are in near resonance. Finally, the number of photons for emission in samples calcined at 1000°C always is $n \approx 2$, see Figure 3.2.2.2.5d. This suggests that the CUC of Yb is the result of a two-photon process coming from Yb^{3+} ion pairs, as mentioned above.
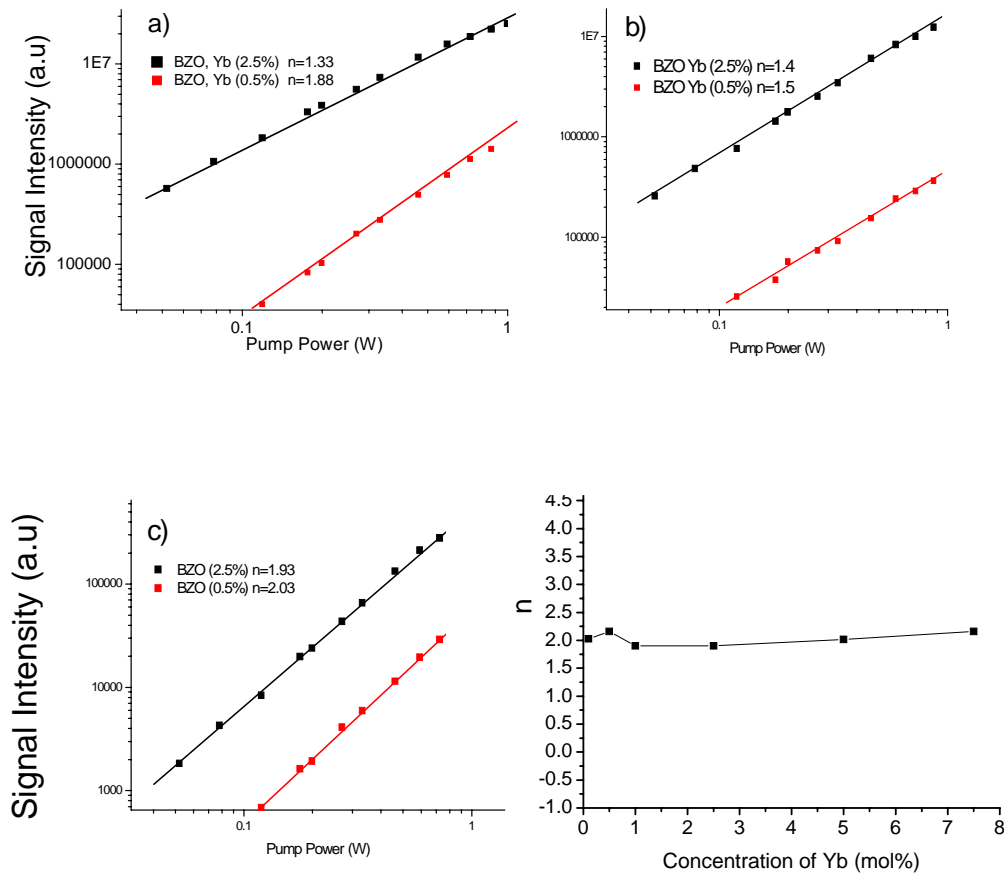
Figure 3.2.2.2.5: Dependence of the green (a), red (b), and blue (c) up-converted emissions as a function of the pumping intensity (sample annealed at 1000°C). Dependence for CUC emission is d).

3.2.3 Decay Time Measurements

Figure 3.2.3.1 shows the VIS and NIR emission decay curves for concentrations of 0.1, 0.5, 1, 2.5, 5 and 7.5 mol% of Yb^{3+} in BZO. The lifetime for VIS emission at 502 nm in nearly the half of the lifetime for the NIR single Yb ion emission. In particular, the single ion emission for $BaZrO_3$:Yb^{3+} (1%) shows a simple exponential decay with a time constant of 460 μs. The cooperative emission decay for this concentration has a time constant of 220 μs, which is nearly the half of that for the single ion emission. For most Yb concentrations, the decay curves have two components, a fast and a slow component. The contribution of each component for the decay curves varies with concentration. The fast component is associated with effects such as quenching. Indeed, we

observe that the contribution of fast component is greater than contribution of slow component for concentration above 1%mol. Hence, the presence of quenching centers affects the lifetime, as we will see later. An exponential fitting of the slow component was computed to obtain the lifetimes. Nevertheless, they are considerably smaller than lifetime reported in other host [18], since these ranges from $70\,\mu s$ to $600\,\mu s$. Maybe, the reduction of the lifetime is due the great influence of quenching centers such as OH⁻.

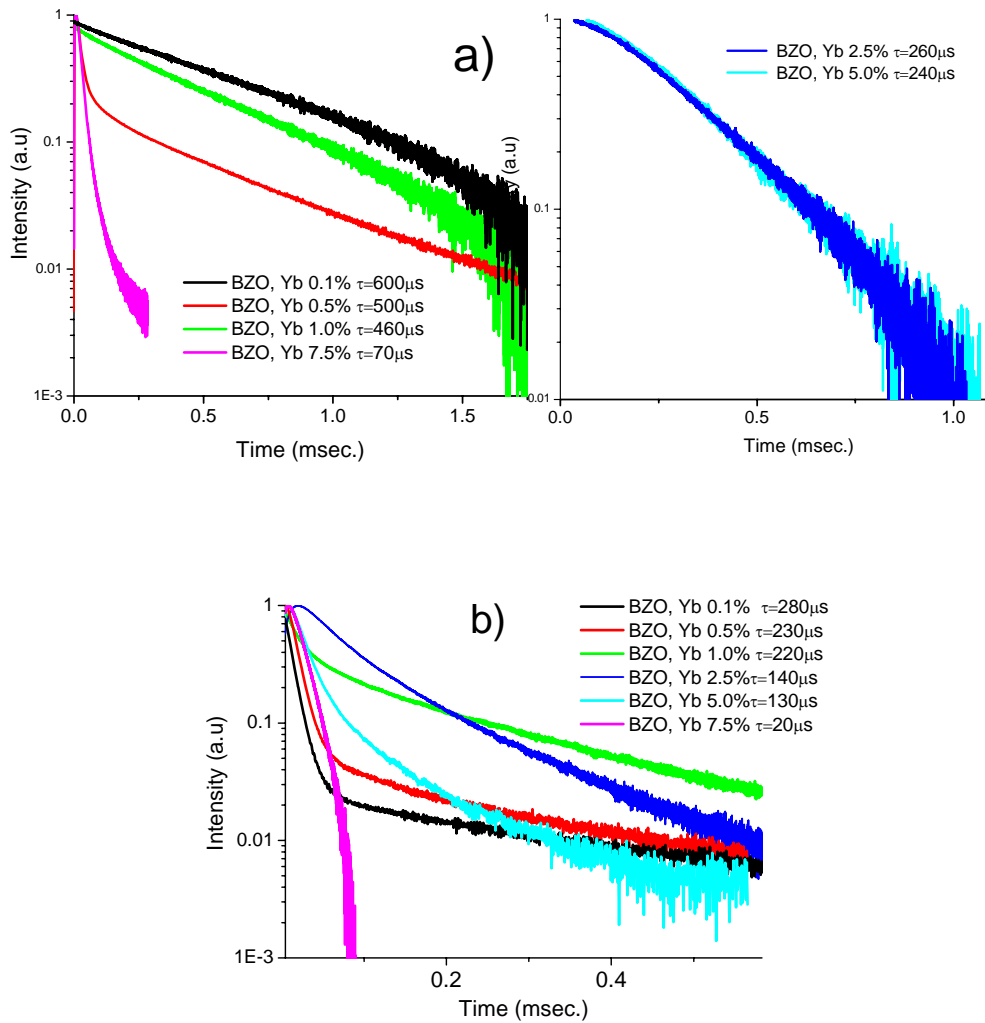*Figure 3.2.3.1: a) Fluorescence decay curves at room temperature for Yb³⁺ single ion , b) Fluorescence decay curves for cooperative luminescence of Yb³⁺ pair.*

3.2.4 Effect of Yb Concentration on Luminescence

Figure 3.2.4.1a shows the trend for NIR emission with Yb concentration. In this case, the intensity of luminescence increases with increasing Yb^{3+} doping level up to 0.5 mol%. When Yb^{3+} concentration is above 0.5 mol%, the luminescence intensity drops dramatically. Meanwhile, Figure 3.2.4.1b shows the quenching effect for emission peaking at 502 nm. We notice that quenching occurs after Yb concentrations higher than 2.5 mol% of Yb, whereas the quenching starts from 0.5 mol% for the NIR emission at 973 nm. If we want the maximal intensity for VIS emission, we would have a weak NIR luminescence.

The decrease in luminescence may be explained as follows: With the increase of Yb^{3+} concentration, the separation between Yb-Yb pairs is reduced, promoting the interaction between them and thus enhancing the cooperative up-conversion emission at 502 nm, that on time reduces the NIR emission and promotes ET form Yb^{3+} pairs to Er^{3+} and Tm^{3+}, being the net result a reduction of both NIR and VIS emissions. Thus, the dominant effect is the Yb^{3+} pairs interaction.

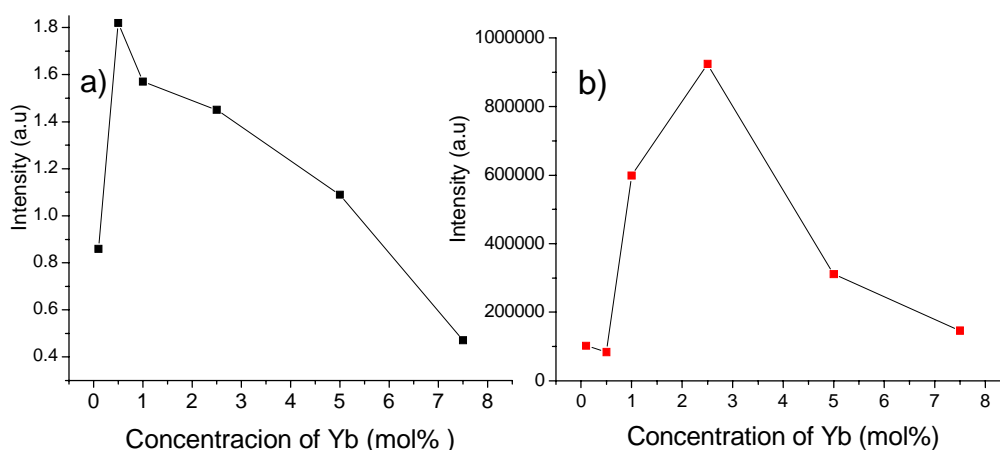*Figure 3.2.4.1: Curves of intensity versus concentration: a) NIR single ion luminescence for Yb^{3+} (emission peak in 973 nm, excitation wavelength 920 nm), b) Visible cooperative luminescence (emission peak in 502 nm, excitation wavelength 967 nm).*

On the other hand, the Yb^{3+} energy migration becomes more probable as the ion–ion separation decreases with higher dopant levels, and may reduce the

cooperative luminescence intensity due to the formation of Yb clusters.

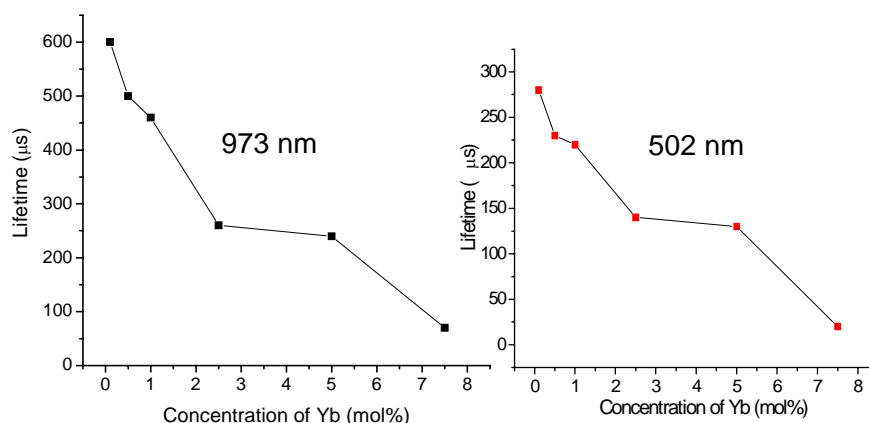## 3.2.5 Effect of Yb Concentration on Luminiscence Lifetime

Figure 3.2.5.1: Experimental lifetime of Ytterbium in Barium Zirconate matrix (wavelength excitation in 920 nm): a) emission peak at 973 nm, b) emission peak at 502 nm.

Figure 3.2.5.1 exhibits the NIR and VIS lifetimes as function of Yb[3+] concentration in BZO host. This curves are similar to the experimental curves reported by Cannibano et al. for Ytterbium doped YAG, GGG and KBM host [15]. The curve 3.2.5.1b for visible lifetime of BZO:Yb (0.1%) shows a maximum of 280 μs and the curve 3.2.5.1a of NIR shows a maximum in 600 μs, corroborating that the VIS emission is nearly the half of NIR emission. Clearly, the rest of samples with different concentrations follows the same trend.

It has been reported that the presence of OH⁻ groups affects the NIR and VIS lifetimes [19,20]. These works emphasize the high efficiency of these OH⁻ as centers of extinction of the infrared emission. The vibrational modes of OH⁻ groups are around of 3300 cm⁻¹. Therefore, only three phonons are needed for nonradiative lost energy for the Yb[3+] transition (~ 10000 cm⁻¹). Thus, The fast decrease of the fluorescence lifetime with concentration indicates that the nonradiative transitions and quenching centers such as OH radicals have a significant effect, since they decrease the lifetime.

Because of the importance of the lifetime for the performance of the BZO:Yb^{3+} system, we decide to carry out an annealing treatment to increase the lifetime. Certainly, the presence of OH^{-} impurities and residual H$_2$O was confirmed by the FTIR spectra, corroborating that the reduction in lifetime is produced by OH^{-} ions. Moreover, we will observe as the lifetime increases while the OH^{-} centers are reduced. These results are shown in the next chapter 4.

3.3 References

[1] Yongjun Dong, Jun Xu, Guoqing Zhou, Guangjun Zhao, Liangbi Su, Xiaodong Xu, Hongjun Li, JiLiang Si, Xiaobo Qian, Xiaoqing Li, and Jun Shen, *Color centers in Yb:YAG crystals grown by temperature-gradient techniques* phys. stat. sol. 203, 2496 (2006).

[2] E. De la Rosa, P. Salas, L.A. Diaz Torres, A. Martinez, C. Angeles, *Strong Visible Cooperative Up-Conversion Emisión in ZrO:Yb^{3+} Nanocrystals*, J. Nanos. and Nanotech. 5, 1480 (2005).

[3] G. Boulon, V. Lupei*, Energy transfer cooperative processes in Yb^{3+} doped cubic sesquioxide laser ceramics and crystals*, Journal of Luminescence 125, 45 (2007).

[4] M. Malinowski, M Nakielska, R. Piramidowicz, J. Sarnecki, *Energy transfer processes in Highly Rare-Earth Doped Planar YAG Waveguides*, Spectroscopy letters 40, 271, (2007).

[5] L.A. Diaz Torres, E. de la Rosa, P. salas and C. Angeles, *Concentration enhanced Red upconversion in nanocrystalline ZrO$_2$:Er^{3+} under IR excitation*, J. Physics D: Appl. Physics, 37, 2489 (2004).

[6] M.j.V Bell, W.G. Quirino, S.L. Oliveira, D.F. de Sousa, L.A.O. Nunes, *Cooperative luminescence in Yb^{3+}-doped phosphate glasses,* J. Phys. Condens. Matter. 15, 4877 (2003).

[7] M.A. Noginov, G.B. Loutts, C.S. Steward, B.D. Lucas, D. Fider, V. Peters, E. Mix, G. Huber, *Spectroscopic study of Yb doped oxide crystals for intrinsic optical bistability*, J.Lumins. 96, 129 (2002).

[8] E. Montoya, L.E. Bausá, B. Schaudel, P. Goldner, *Yb^{3+} distribution in LiNbO$_3$:(MgO) studied by cooperative luminescence,* J. Chem. Phys. 114, 3200 (2001).

[9] David W. Ball. The Basics of Spectroscopy. Spie Press, 2001.

[10] David W. Ball. Field Guide to Spectroscopy. Spie Press, 2006.

[11] E. Montoya, O. Espeso, L.E. Abusa. *Cooperative luminescence in Yb^{3+}:LiNbO$_3$*, Journal of Luminescence 87-89, 1036 (2000).

[12] P. Salas, C. Angeles-Chávez, J.A. Montoya, E. De la Rosa, L.A. Díaz-Torres, H. Desirena, A. Martínez, .A. Romero-Romo and J. Morales; *Synthesis, characterization and luminescence properties of ZrO$_2$:Yb^{3+}-Er^{3+} nanophosphor*, Opt. Mater. 27, 1295 (2005).

[13] Jose Perez Huerta, UV *To Red Upconversion Emisión From Er-Yb Codoped Barium Zirconate*, Tesis de Maestria, Centro de Investigaciones en Óptica, Mexico (2007).

[14] Elena Canibano Crespo*, Propriétés spectroscopiques de l'ion Yb^{3+} dans les familles d'oxydes de molybdates K$_5$Bi(MO$_4$)$_4$, de grenats Y$_3$Al$_5$O$_{12}$, Gd$_3$Ga$_5$O$_{12}$, Lu$_3$Al$_5$O$_{12}$ et de perovskites YAlO$_3$. Analyse de mécanismes d'extinction par concentration et évaluation de l'émission laser*. PhD thesis, Université Claude Bernaud Lyon, France (2002).

[15] E. De la Rosa, D. Solis, L.A. Diaz-Torres, P. Salas, C. Angeles-Chavez, O. Meza, *Blue-green emission in ZrO$_2$:Yb^{3+} nanocrystals* (submitted)

[16] Shiquing Xu, Dawei Fang, Zaixuan Zhang, Liyan Zhang, Shilong Zhao, Zhonghong Jiang, *Host dependent frecuency upconversion of Yb^{3+}/Tm^{3+} - codoped oxyfluoride glasses*, Material science and Engineering B 122, 236 (2005).

[17] A.A. Demicovich, A.N. Kuzmin, N.K. Nikeenko, A.N. Titov, M. Mond, S, Kueck, *Optical characterization of Yb,Tm: KYW crystal concerning laser application*, J. Alloys and Compounds 341, 124 (2002).

[18] P. Goldner, B. Schaudel, and M. Prassas, *Dependence of cooperative luminescence intensity on Yb[3+] spatial distribution in crystals and glasses,* Phys. Rev.B 65, 054103 (2002)

[19] L. Zhang, H. Hu, *The effect of OH- on IR emission of Nd[3+], Yb[3+] and Er[3+] doped tetraphosphate glasses*, J. of Phys. and Chem. of Solids 63, 575 (2002).

[20] J. K. Krebs, S. P. Feolifov, A. A. Kaplyanskii, R. I. Zakharchenya, U. Hapeek, *Nonradiative relaxation of Yb3+ in highly porous -Al$_2$O$_{3,}$* J. of Luminescence 83-84, 209 (1999).

Chapter 4: Annealing Effect

4.1 Introduction

In literature, two principal effects on the Yb^{3+} doped host have been reported, photodarkening and reduction of Yb^{3+} to Yb^{2+}, both effects produce a deleterious effect on the luminescence properties [1-4,5,6]. Photodarkening refers to any process in which an object becomes non-transparent (dark) on illumination. This phenomenon is recognized in materials presenting increased absorption. It has also been observed in systems where laser radiation interacts with an amorphous media, such as optical fibers. Therefore, photodarkening is recognized as a potentially important limiting factor on the lifetime and reliability of many Yb-doped fiber lasers and amplifiers [3]. The photodarkening process is attributed to the formation of photoinduced structural transformations (color centers) that induce excess loss in fibers, resulting in reduced output power efficiency [2-5]. Many investigations about the optical absorption and induced color centers in Yb doped crystals (YAG, $LiYF_4$, $LiLuF_4$ and PWO) after gamma irradiation, have demonstrated the formation of F-type color center, oxygen vacancies, formation of Yb^{2+} centers as an effect of recharging one of Yb^{3+} ion pairs and the destruction of color centers under thermal treatment [7-9].

On the other hand, Thermodarkening is considered as an increase in the optical absorption band induced by annealing treatment, this effect has been observed in chalcogenide glasses and $HgSe-GeSe_2$ alloys but not in oxides [10]. In this chapter, we report the optical characterization of BZO after air annealing process. It is reported an increment on the absorption properties in the UV-VIS region and an increment of both, single and Yb^{3+} pair emission as the annealing temperature increases. To the best of our knowledge, this is the first report of thermodarkening effect in oxides, particular BZO perovskite. The aim of this chapter is to present the effect of annealing on the absorption, emission and fluorescence lifetime of Yb doped Barium Zirconate and to compare it with the photodarkening process.

4.2 Annealing Procedure

Under NIR excitation at 940 nm the BaZrO$_3$:Yb(0.5%) sample presents a very good NIR emission intensity as well as a strong visible CUC emission. In order to study the annealing temperature effect, this sample was annealed at 100 °C, 500 °C, 750 °C and 1000 °C in a furnace during 14 h, with a heating rate of 5°C /min. For each temperature a sample was taken out of the furnace and was cooled down to room temperature in air.

4.3 Annealing Treatment Results

4.3.1 Structural Characterization

Figure 4.3.1.1 shows the FTIR spectrum of Yb doped samples, the spectrum reveals an intense broadband centered around 544 cm^{-1} attributed to Zr-O vibration in the perovskite structure [11, 12]. This band presents a clear increase in absorption on increasing annealing temperature. This is due to the improvement of Zr-O bonding, leading to an enhancement of crystallinity in BZO host. The peaks at 858, 1060, 1437 and 3417 cm^{-1} is related to CO_3^{2-} groups [11], stretching vibrations of C-O groups [13], to OH deformation vibrations [14], and to water and hydroxyl groups adsorbed on the surface of BZO, respectivelly [11, 15]. These bands decrease as the annealing temperature increases indicating the reduction of undesired impurities.
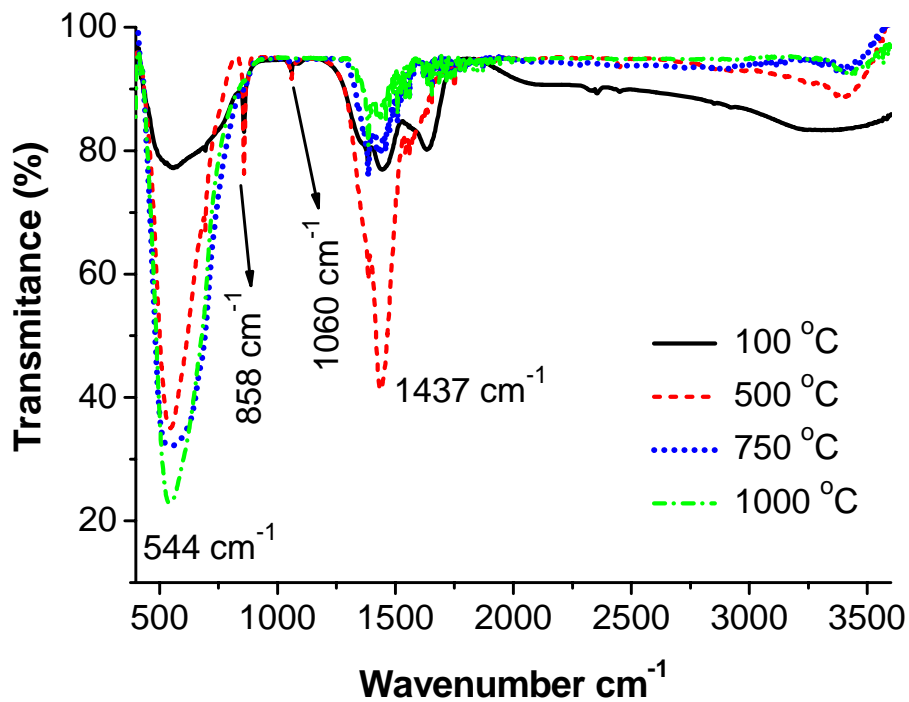
Figure 4.3.1.1: FTIR spectra of BaZrO₃:Yb at 0.5 mol% doped sample with different temperatures of annealing.

4.3.2 Absorption Spectra

The normalized absorption spectra for both, undoped and doped BaZrO:Yb^{3+}, powders annealed at 100 °C, 500 °C, 750 °C and 1000 °C, are shown in Figure 4.3.2.1. An increase in absorption in the UV-VIS range is clearly observed, suggesting the formation of defects such as color centers or oxygen vacancies. This indicates the presence of Thermodarkening. This effect is comparable to the photodarkening observed in optical fibers as mentioned above [3].

Figure 4.3.2.1: Normalized absorption spectra of, a) undoped and b) doped BZO samples. c) and d) show an enlargement of (b) for the visible and NIR region, respectively.
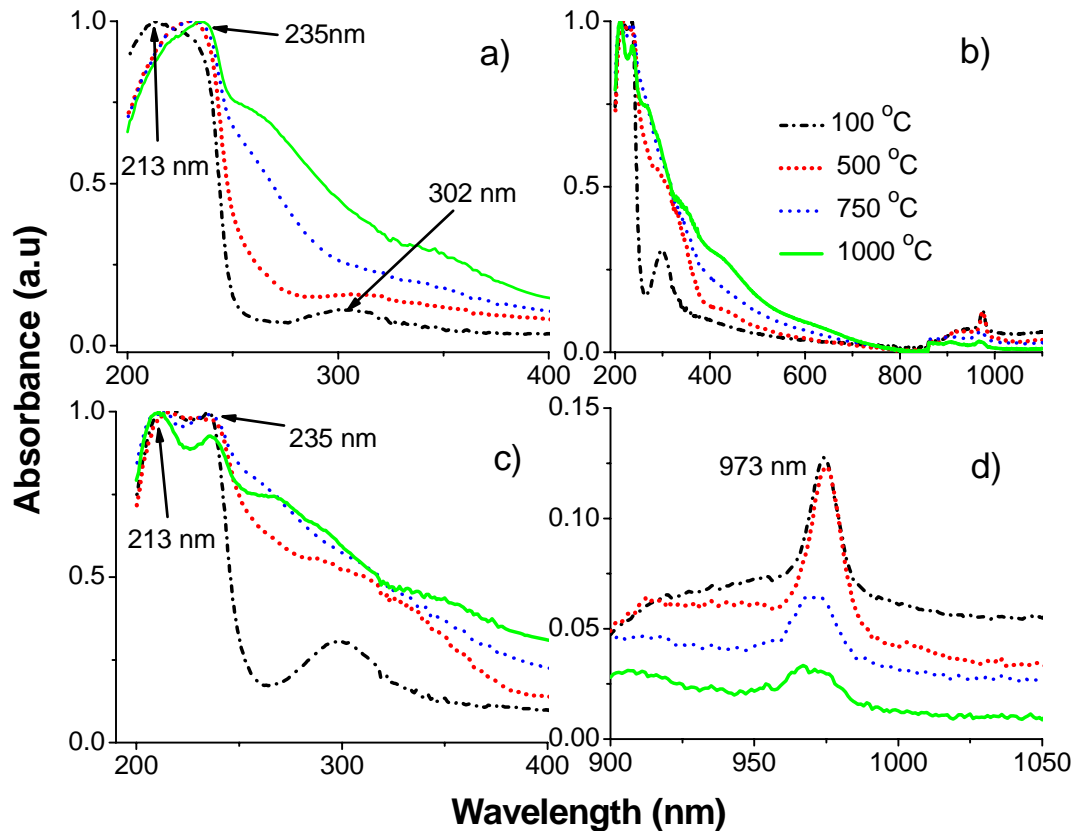
Notice the shifting of the absorption peak to longer wavelengths (from 213 nm to 235 nm) as the annealing temperature increases (Figure 4.3.2.1a). Meanwhile, for doped samples a dramatic increase in absorption in the UV-VIS band and a decrease of the characteristic NIR absorption band of Yb^{3+} were observed, see Figure 4.3.2.1b. In this case, three main effects of Ytterbium are evident: 1) The introduction of Ytterbium gives rise to an splitting of the absorption band characteristic of the host forming 213 nm and 235 nm peaks, see Figure 4.3.2.1c. These peaks were only observed separately in undoped samples annealed at 100 °C and 1000 °C respectively, see Figure 3a. Since the 235 nm peak corresponds to the band gap of ZrO_2 [16], we could associate the 213 nm absorption peak as a contribution of the presence of Ba in the BZO crystalline structure. In this way, the annealing temperature in undoped samples enhances the Zirconium effect, whereas the contribution of the Ba in the host

lattice decreases. Thus, the "shifting" of 213 nm peak means a decrease of this band. Probably, such shifting indicates the formation of $Ba^{2+} - O^{-2}$ bonds, considering that oxygen vacancies (V_O) are removed by the annealing process and that the 213 nm peak is associated with $Ba^{2+} - V_O$. For doped samples, the presence of such band suggests that V_O are not completely removed, perhaps because are forming F centers as a part of the charge compensation process. This will be explained later. 2) The presence of new absorption bands in the UV-VIS range of annealed doped samples (423 nm and 655 nm) in comparison with undoped samples. 3) The decrease of NIR absorption band of Yb[3+], see Figure 4.3.2.1d, and the change in color from white to yellow-brown in doped an undoped samples after annealing. These changes are the signature of the reduction of $Yb^{3+} \rightarrow Yb^{2+}$ ion and the formation of color centers, respectively. Such reduction has been reported by others authors in Yb doped fibers, YAG and YAP crystals [8,9].

4.3.3 The Luminescence Properties

The VIS and NIR emission spectra in Yb^{3+} doped samples for different annealing temperatures under 920 nm excitation wavelength are shown in Figure 4.3.3.1. Annealing improved the crystalline structure and eliminated quenching centers to a good extent, as is shown above in Figure 4.3.1.2. As a result, both VIS and NIR emission were enhanced as the annealing temperature increases.
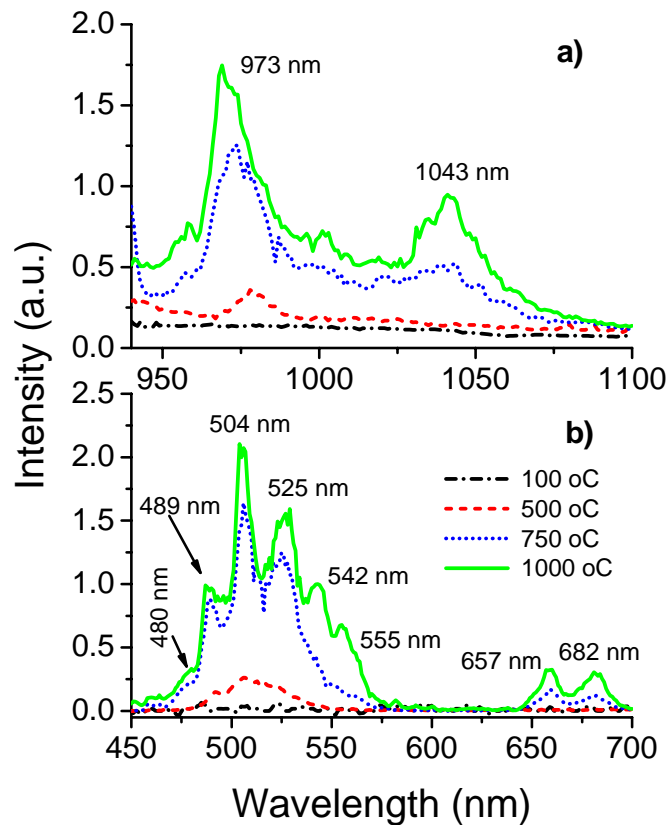
Figure 4.3.3.1: Emission spectra of $BaZrO_3:Yb^{3+}$, a) NIR emission and b) visible emission.

The transitions associated to NIR and VIS emission presented by the BZO:Yb (0.5%) annealed at 1000 °C, have been described in Chapter 3. Figure 4.3.3.2 shows the dependence of the upconverted signal intensity (I_{UPC}) as a function of the pump power (I_{PUMP}). In the case of the sample annealed at 1000 °C, n~2, n~1.9 and n~1.7 for cooperative emission, green band and red band, respectively, confirming that such emission is the result of a two-photon process.

Figure 4.3.3.2: Dependence of the signal intensity, CUC, green and red emission as function of the pump power for sample annealed at 1000 °C.

It is noticeable that the sample annealed at 100 °C does not present emission for both, VIS and NIR range. This could be because of the high content of quenchi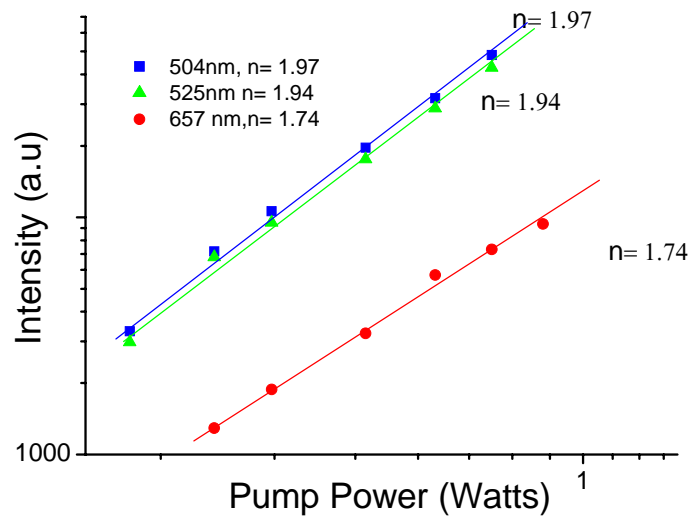ng centers. The OH$^-$ groups and residual H_2O, which are known to have a great influence on NIR and VIS emission, are present in BZO as is shown in Figure 4.3.1.2 [15,17]. Such impurities quench the fluorescence emission. When the annealing temperature increases, the residual impurities are reduced and the emission intensity increases. This reduction in quenching centers with temperature is expected to result in an increment of the fluorescence decay time in both, NIR and cooperative emission, as can be observed in Figure 4.3.3.3. The lifetime for CUC emission peak is nearly half of the lifetime characteristic of the infrared emission peak. As expected, such relation is the same for each annealing temperature, implying that CUC emission is produced by an Yb^{3+} pair, see Figure 4.3.3.3.
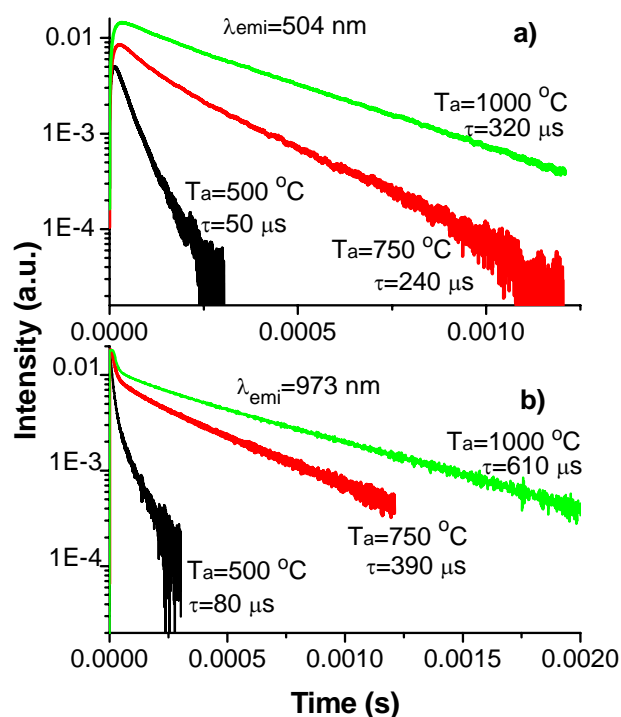
Figure 4.3.3.3: Fluorescence decay profiles of, a) CUC emission peak at 504 nm and b) 973 nm emission peak for different annealing time.

The decay profiles corresponding to the emission peak at 504 nm (CUC emission) and NIR emission at 973 nm are shown in Figure 4.3.3.3a and 4.3.3.3b, respectively. In both cases, profiles are fitted by two exponential functions. For low annealing temperature, decay time is dominated by fast decay component but for high annealing temperature, it is dominated by slow decay component. These results point out that fast decay component is associated with quenching or residual impurities centers. The lifetimes obtained by an exponential fitting of the experimental decay curves for CUC emission, range from 50 μs to 320 μs for 500 °C and 1000 °C, respectively. On the other hand, the obtained lifetime for 973 nm emission band, range from 80 μs to 610 μs for 500 °C and 1000 °C.

4.3.4 The Presence of Yb^{2+} and Color Centers

Figure 4.3.4.1 shows the difference between doped and undoped BZO absorption spectra. Two broad bands are observed, 417 nm and 655 nm. The former is directly related to cooperative absorption, as this band is in agreement with the self-convolution of the NIR absorption spectra. Furthermore, this band increases with annealing temperature confirming the formation of Yb^{3+} ions pairs thereby improving the cooperative emission, see Figure 4.3.3.1b. According to literature, the 655 nm absorption band is characteristic of Yb^{2+} and is in agreement with the decrease of absorption band of single Yb^{3+} ion [18,19,21].
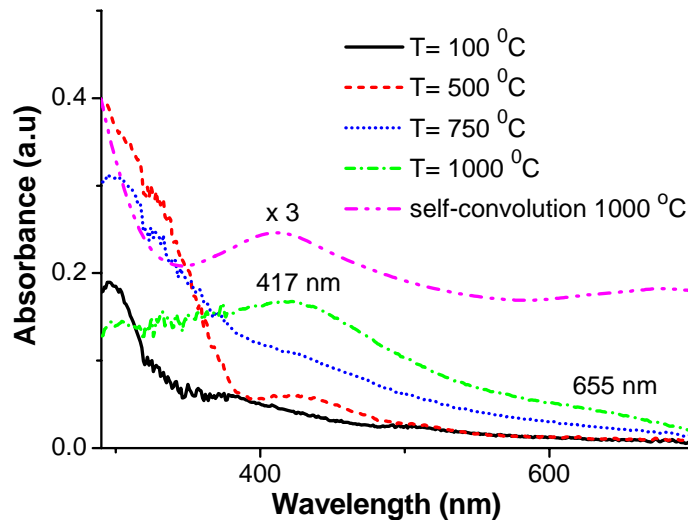
Figure 4.3.4.1: Absorbance difference between normalized doped and undoped samples, and self-convolution of NIR absorption band of single Yb^{3+} ion.

The emission of Yb^{2+} in different hosts has already been reported [20-22]. However, in our case, no fluorescence of the Yb^{2+} was observed after excitation at 655 nm. This can be explained as follows. Ahmed et al. reported that the introduction of Yb^{3+} ion in BZO host involves the substitution of Zr^{4+} at B-site positions, in consequence there is a charge compensation. Such compensation shares one electron from Yb^{3+} with oxygen vacancies (V_O) produced mainly by the synthesis process [23]. This leads to the formation of F color centers. The doped sample annealed at 100 °C in Figure 4.3.2.1b presents a broad band in

the region of 265-335 nm which corresponds to the superposition of F color centers (one or two electrons trapped in an oxygen vacancy) and Oxygen vacancies [8]. Such absorption bands increase with the annealing temperature. Since the annealing treatment is in an oxygen rich environment, oxygen enters the crystal structure reducing the Oxygen vacancies. Thus, it is reasonable to assume that the enhancement of the absorption band is produced by the formation of F color centers. The formation of these defects is confirmed by the change in color from white to yellow-brown in doped BZO. In opposite to results reported by Zeng et al. in which the air annealing after gamma irradiation destroys F color centers [24]. The increase in the absorption band in the UV-VIS region with the change from colorless to yellow on Yb^{2+} formation, has been observed in Yb doped silica performs [25]. Thus, the change in color is associated with color centers formation.

M. Henke et al. reported the absorption bands peaking at 280 nm and 660 nm and were attributed to the absorption of Yb^{2+} in $Yb^{2+}:Y_3Al_5O_{12}$ crystal [22]. Xie et al. ascribed the 284 nm and 300 nm bands to Yb^{2+} absorption in $\alpha - SiAlON$ [26]. Hence, the 265-335 nm absorption band which increases with annealing temperature can be considered as the superposition of Yb^{2+}, F color center and Oxygen vacancies. This behavior is in agreement with the decrease of the Yb^{3+} NIR absorption band (see Figure 4.3.2.1d) and suggest the formation of Yb^{2+}-F centers pairs. Such pairs formation inhibits the Yb^{2+} emission (traps for emitted photons). Several bands of F color centers accompanied by Yb^{2+} ions (Yb^{2+}-F pairs) has been reported in CaF_2 crystals [6]. In the case of undoped sample, a broad band in the 274-327 nm region is observed. Again, this band is attributed to superposition of F color centers as well as oxygen vacancies, but the increment of the UV-VIS absorption band with annealing temperature is produced only by the F centers because there is no Yb^{3+}. This is confirmed by the change in color from white to yellow-brown for undoped samples. The $Yb^{3+} \rightarrow Yb^{2+}$ reduction to form isolated Yb^{2+} ions, as suggested by the 655 nm band, is promoted by the electrons captured from F centers formed during annealing in air. Finally, it is possible that Yb^{2+} replaces the Ba^{2+} position because the ionic radii is quite similar (1.28 nm for Yb^{2+} and 1.35 nm for Ba^{2+} in eightfold coordination). They also have similar charge.

However, more studies are required to verify this hypothesis.

Figure 4.3.4.2 shows the dependence of annealing temperature with the 265-335 nm absorption band attributed to the superposition of Yb^{2+}, F color center and Oxygen vacancies. In this way, we could have a trend about the increase of the Yb^{2+}-F pairs with annealing. Thus, it can be observed almost a linear increase at the beginning, but a saturation for higher annealing temperature. Such behavior is in agreement with the drecease of the NIR band, as is shown in Figure 4.3.4.3. In these figures, it is considered that the integraded NIR band of Yb^{3+} is proportional to the Yb^{3+} concentration and the integrated UV-VIS band is proportional to the Yb^{2+}-F pairs concentration.

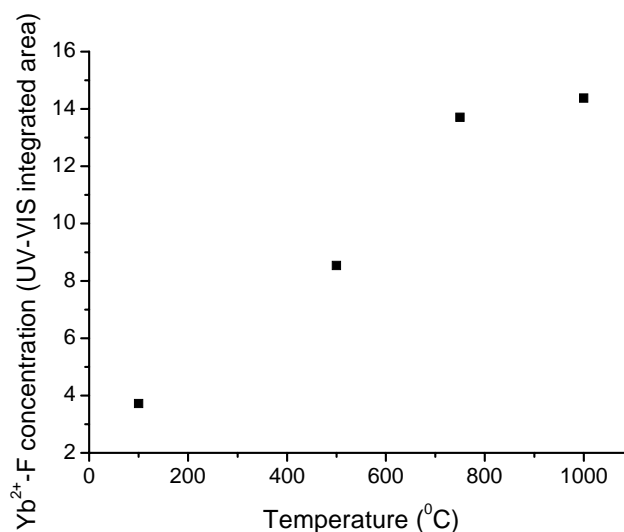

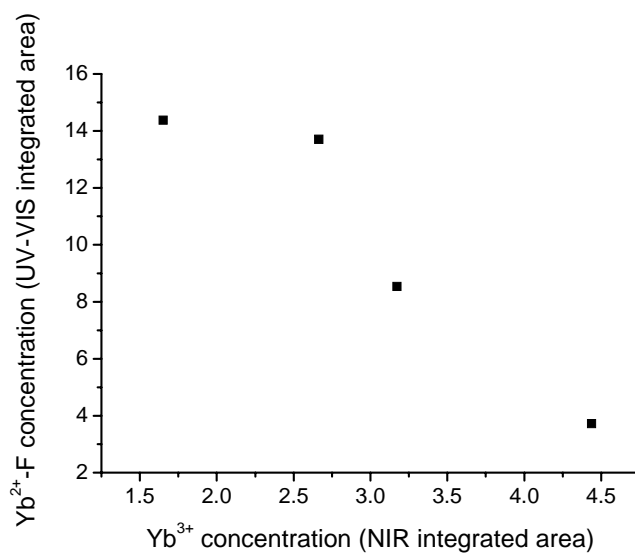*Figure 4.3.4.2: Yb^{2+}-F^+ concentration dependence with annealing temperature for $BaZrO_3$:Yb 0.5 mol% sample.*

Figure 4.3.4.3: Yb^{2+}-F^{+} concentration dependence with Yb^{3+} concentration for BaZrO$_3$:Yb 0.5 mol% sample.

4.4 References

[1] L. He, Y. Wang, H. Gao, *Characterization of the VUV excitation spectrum of BaZr(BO$_3$)$_2$:Eu,* J. Lumin. 126, 182 (2007).

[2] Y. Dong, J. Xu, G. Zhou, G. Zhao, L. Su, X. Xu, H. Li, J. Si, *Gamma-ray induced color centers in Yb:YAG crystals grown by Czochralski method*, Sol. State Commun. 141, 105 (2007).

[3] J. J. Koponen, M. J. Söderlund, H. J. Hoffman, *Measuring photodarkening from single-mode ytterbium doped silica fibers*, Opt. Express 14, 11539 (2006)

[4] M. Broer, D. M. Krol, D. J. DiGiovanni, *Highly nonlinear near-resonant photodarkening in a thuliumdoped aluminosilicate glass fiber*, Opt. Lett. 18, 799 (1993).

[5] I. Manek-Hönninger, J. Boullet, *Photodarkening and photobleaching of an ytterbium-doped silica double-clad LMA fiber*, Opt. Express 15, 1606 (2007).

[6] S. M Kaczmarek, T. Tsuboi, M. Ito, G. Boulon and G. Leniec, *Optical study of Yb^{3+}/Yb^{2+} conversion in CaF$_2$ crystals*, J. Phys. Condens. Matter 17, 3771 (2005).

[7] Y. Huang, K. Jang, H. Jin, L. Zhao, *Color Centers and Charge Transfer Luminescence in a Yb^{3+}-Doped PbWO$_4$ Single Crystal*, J. Korean Phys. Soc. 49, 227 (2006).

[8] Y. Dong, J. Xu, G. Zhou, G. Zhao, L. Su, X. Xu, H. Li, J. Si, X. Qian, X. Li, *Color centers in Yb:YAG crystals grown by temperature-gradient techniques*, J. Shen, Phys. stat. sol. 203, 2496 (2006)

[9] Y. Dong, G. Zhou, J. Xu, G. Zhao, F. Su, L. SU, H. Li, J. Si, X. Qian, X. Li, J. Shen, *Color centers and charge state recharge in c-irradiated Yb:YAP*, Opt. Mat. 28, 1377 (2006).

[10] V.V. Halyan, V.V. Bozhko, *Relaxation and thermoinduced processes in glassy HgSe$_{(x)}$-GeSe$_{2(1-x)}$ alloys*, Semiconductor physics, quantum electronics and optoelectronics 6, 73 (2003).

[11] F. Boschini, B. Robertz, A. Rulmont, R. Cloots, Preparation of nanosized barium zirconate powder by thermal decomposition of urea in an aqueous solution containing barium and zirconium, and by calcination of the precipitate, J. European Ceram. Soc. 23, 3035 (2003).

[12] A. A. Athawale, A. J. Chandwadkar, P. Karandikar, R. Pasricha, M. S. Bapat, *Radiation assisted synthesis of nanosized barium zirconate*, Rad. Phys. and Chem. 75, 755 (2006).

[13] Georges Socrates, *Infrared Characteristic Group Frequencies*, Second Edition, Wiley and Sons (1998).

[14] R. B. Cervera, Y. Oyama, S. Yamaguchi, *Low temperature synthesis of nanocrystalline proton conducting BaZr$_{0.8}$Y$_{0.2}$O$_3$ − δ by sol–gel*, Sol. Stat. Ionics 178, 569 (2007).

[15] H. P. Kumara, C. Vijayakumar, C. N. George, S. Solomon, R. Jose, J.K. Thomasa, J. Koshya, *Characterization and sintering of BaZrO$_3$ nanoparticles synthesized through a single-step combustion process*, J. Alloys and Comp. *In Press* (2007).

[16] K.G. Kanade a, J.O. Baeg b, S.K. Apte c, T.L. Prakash c, B.B. Kale, *Synthesis and characterization of nanocrystallined zirconia by hydrothermal method*, Mat. Research Bull. 43, 723 (2007).

[17] G. Taglieri, M. Tersigni, P.L. Villa, C. Mondelli, *Synthesis by the citrate route and characterisation of BaZrO$_3$, a high tech ceramic oxide: preliminary results*, Int. J. Inorganic mat. 1, 103 (1999).

[18] X. Xu, Z. Zhao, G. Zhao, P. X. Song, J. Xu, P. Deng, *Comparison of Yb:YAG crystals grown by CZ and TGT method*, J. Crystal Growth 257, 297 (2003).

[19] D. Fagundes-Peters, N. Martynyuc, K. Lunstedt, V. Peters, *High quantum efficiency YbAG Crystals*, J. Lumin. 125, 238 (2007).

[20] S. Lizzo, E.P. Klein Nagelvoort, R. Erens, A. Meijerink, G. Blasse, *On The Quenching of the Yb^{2+} luminiscence in differents Host Lattices*, J. phys. Chem. Solids 58, 963 (1997).

[21] M. Nikl, A. Bensalah, E. Mihokova, J. Hybler, H. Sato, T. Fukuda, G. Boulon, *Luminescence and decay kinetics of Yb^{2+} in $LiCaAlF_6$ single crystal host*, Opt. Mat. 24, 191 (2003)

[22] M. Henke, J. Perbon, S. KuK, *Preparation and spectroscopy of Yb^{2+}-doped $Y_3Al_5O_{12}$, $YAlO_3$, and $LiBaF_3$,* , J. Lumin. 87-89, 1049 (2000).

[23] I. Ahmed, S.G. Eriksson, E. Ahlberg, C.S. Knee, H. Götlind, L.G. Johansson, M. Karlsson, A. Matic, L. Börjesson, *Study and proton conductivity in Yb-doped $BaZrO_3$*, Sol. Stat. Ionics 178, 515 (2007).

[24] X. Zeng, X. Xu, X. Wang, Z. Zhao, G. Zhao, J. Xu, *Effects of gamma-irradiation and air annealing on Yb-doped $Y_3Al_5O_{12}$ single crystal*, Spectrochimica Acta Part A 69, 860 (2007).

[25] J. Kirchhof, S. Unger, A. Schwuchow, S. Grimm, V. Reichel, *Materials for high-power fiber lasers*, J. Non-Crystalline Solids 352, 2399 (2006).

[26] R.J. Xie, N. Hirosaki, M. Mitomo, K. Uheda, T. Suehiro, X. Xu, Y. Yamamoto, *Strong Green Emission from $\alpha-SiAlON$ Activated by Divalent Yterbium under Blue Light Irradiation*, J. Phys. Chem B 109, 9490 (2005).

CHAPTER 5: Conclusions and Perspectives

5.1 Conclusions

Barium Zirconate samples with different concentrations of Yb were synthetized by hydrothermal process at 100°C. XRD difraction patterns show that BZO presents cubic phase. There is no change in phase with annealing at 1000°C for samples with concentration lower than 5 mol%. However, in Yb doped samples with concentrations above 7.5 mol%, segregation of phase occurs. FTIR analysis show the presence of impurities as hydroxil groups and residual H_2O. Also, an intense broadband centered around 544 cm^{-1} was attributed to Zr-O vibration and a maximum phonon mode of 590 cm^{-1} was observed.

The energy band gap of 5.18eV for BZO was determined from absorption spectra of undoped host. The visible luminescence is ascribed to Yb^{3+} cooperative emission and the presence of rare earth impurity ions. Because of the presence of Tm^{3+} and Er^{3+} impurities was not detected in the absorption spectra, it is suggested that the impurity concentration is on the level of traces. It is noticeable the strong emission of impurities, considering that its concentration is probably of traces. This fact suggests very efficient upconversion processes involving traces of Tm^{3+} and Er^{3+} ions having the Yb^{3+} ions as sensitizers. Also, the lifetime of visible emission at 502 nm is nearly the half of the lifetime of the NIR single Yb ion emission for all concentrations. Moreover, the dependence of the upconverted signal intensity as a function of the pump power suggests that the upconversion emission involves a two photon process, corroborating the presence of cooperative emission. The dependence of NIR Emission Intensity with Yb^{3+} concentration shows that the optimum concentration of Yb to obtain the best NIR emission and strong visible CUC emision is 0.5 mol%. Nevertheless, the dependence of the luminiscence Lifetime with concentration for NIR and VIS emission shows that quenching occurs.

On the other hand, we presented the annealing effect on 0.5 mol% Yb^{3+} doped and undoped BaZrO$_3$. Annealing process played a very important role removing to some extent both, oxygen vacancies and undesired impurities (OH, residual H$_2$O and C-O groups). For doped samples, F color centers were formed as a result of the combination of charge compensation and the presence of oxygen vacancies. In turn, these centers promote the reduction from Yb^{3+} to Yb^{2+}. The result is an increment in the UV-VIS absorption band for doped and undoped samples indicating the presence of the thermodarkening. The overall result is a remarkable increment of both, visible and NIR, luminescence emission. These results demonstrate that the decrease of quenching centers with annealing temperature is the dominant process regardless of the formation of F color centers and the $Yb^{3+} \rightarrow Yb^{2+}$ reduction, that are detrimental for emission. However, the absence of Yb^{2+} emission confirms the formation of Yb^{2+}-F type color centers pairs that inhibit the emission.

5.2 Perspectives

The development of new sources for Visible light is very important for innovation of devices such as displays, LED's and lasers. Because of the Yb doped Barium Zirconate presented strong Blue emission, this could be considered as a promising material to develop high efficient luminiscents phosphors. Further investigations are necessary with other Rare Earth ions. Perhaps Eu^{3+}, Ce^{3+} and Ho^{3+} to generate Red, yellow and green emission, respectively. By the way, Barium Zirconate produces Second harmonic Generation (SHG), which is important for solid state lasers. SHG was observed in laboratory with less intensity that cooperative emission. Hence, another branch of research should be explored.

Appendix A

Annealing Effect on the Luminescence Properties of BaZrO$_3$:Yb^{3+} microcrystals
J. Oliva, E. De la Rosa, L.A. Diaz-Torres, P. Salas and C. Ángeles-Chavez.
Accepted for publication in Journal of Applied Physics, May 2008.

Annealing Effect on the Luminescence Properties of BaZrO$_3$:Yb^{3+} microcrystals

J. Oliva,[1] E. De la Rosa,[1,*] L.A. Diaz-Torres,[1] P. Salas[2] and C. Ángeles-Chavez[3]

[1] Centro de Investigaciones en Optica, A. P. 1-948, León Gto. 37160 México

[2] Centro de Física Aplicada y Tecnología Avanzada, Universidad Nacional Autónoma de México, A.P. 1-1010, 76000 Querétaro, México

[3] Instituto Mexicano del Petróleo, Cd. de México, D.F. 07730 México

* Corresponding author: elder@cio.mx

Abstract

Yb doped Barium Zirconate (BaZrO$_3$:Yb^{3+}) was synthesized by a hydrothermal method at 100 °C. It present a cubic perovskite crystalline phase which is stable between 100 °C and 1000 °C. On increasing the annealing temperature two major changes are observed: 1) The near infrared (NIR) absorption band of Yb^{3+} decreases and an enhancement of both, NIR emission of Yb^{3+} single ion and visible (VIS) emission of Yb^{3+} pairs, occurs. This is attributed to the reduction of impurities. 2) Annealing process induces new absorption bands in the UV-VIS region that increases as annealing temperature increases. These results suggest that reduction of Yb^{3+} to Yb^{2+} is taking place. The visible emission is considered to be a cooperative emission from Yb^{3+} pairs. Under UV and VIS excitation no emission of Yb^{2+} ions was observed. This suggests that the broad band absorption in the UV-VIS region might be related to F color centers which are responsible for the inhibition of the Yb^{2+} ion emission.

1. Introduction

In recent years, several investigations about Yb-doped materials have revealed potential applications for these systems since they can be used to design tunable lasers in the near infrared range from 920 nm to 1060 nm as well as visible cooperative emission at around 500 nm.[1-3] There are only two manifolds in Yb^{3+} energy level diagram, the $^2F_{7/2}$ ground state and $^2F_{5/2}$ excited state around 10000 cm^{-1} in the NIR spectral region (978 nm). Such condition is important to avoid unfavorable processes like excited state absorption or cross-relaxation that are detrimental in lasers systems. Cooperative upconversion (CUC) luminescence is a very unusual upconversion processes in which two ions of Yb^{3+} are excited and decay simultaneously, emitting one photon at twice the energy of the single ion transition. Upconverted cooperative emission of Yb^{3+} has been reported in nonlinear materials like LiNbO$_3$ which are used in optoelectronic applications, YAG planar epitaxial waveguides, YAP crystals for diode pumped solid state lasers, as well as YAG and ZrO$_2$ nanocrystals which present strong visible emission.[2-7] Even though cooperative luminescence is a detrimental factor for infrared lasers, this is an alternate way to produce visible emission that can find many applications. Barium Zirconate (BaZrO$_3$, BZO) is a promising refractory ceramic material with a high melting point (1600 °C) and a low chemical reactivity towards corrosive compounds. It belongs to perovskite family of the type A^{2+} B^{4+} O$_3$. BZO is a cubic oxide perovskite that does not follow phase transition in the range of 4 K and 1600 K.[8] Because of this, BZO has been used in high temperature superconductor, electroceramic and protonic applications.[9] In addition, the BZO matrix shows a great potential for a variety of technological applications in electro-optic, waveguides and second

harmonic generation.[10,11] There are only a few reported studies about the electronic and optical properties of bulk, micro and nanosized BZO. Zhang et al. have studied europium doped $BaZrO_3$ prepared by Pechini-type complex sol-gel method and reported weak orange luminescence of Eu^{3+} under UV excitation.[12] Whereas L. He et al. shows strong red luminescence of $BaZr(BO_3)_2$:Eu,Si synthesized by sol-gel reaction where the Si^{4+} acts as sensitizer of luminescence.[13] To our knowledge, no report of the luminescence properties of $BaZrO_3$:Yb^{3+} has been done up to now.

Two principal effects on the Yb^{3+} doped host have been reported, photodarkening and reduction of Yb^{3+} to Yb^{2+}. Both effects produce a deleterious effect on the luminescence properties.[13-16, 22, 26] Photodarkening refers to any process in which an object becomes non-transparent (dark) on illumination. This phenomenon is recognized in materials presenting increased absorption. It has also been observed in systems where laser radiation interacts with an amorphous media, such as optical fibers. Therefore, photodarkening is recognized as a potentially important limiting factor on the lifetime and reliability of many Yb-doped fiber lasers and amplifiers.[15] Photodarkening is attributed to the formation of photoinduced structural transformations (color centers) that induce excess loss in fibers, resulting in reduced output power efficiency.[14-22] Many investigations about the optical absorption and induced color centers in Yb doped crystals (YAG, $LiYF_4$, $LiLuF_4$ and PWO) after gamma irradiation, have demonstrated the formation of F-type color center, oxygen vacancies, formation of Yb^{2+} centers as an effect of recharging one of Yb^{3+} ion pairs and the destruction of color centers after thermal treatment.[23-25] In the case of CaF_2

crystals, annealing treatment in H_2 atmosphere causes the reduction of $Yb^{3+} \rightarrow Yb^{2+}$.[26] Likewise, thermodarkening is considered as an increase in the optical absorption band induced by annealing treatment. This effect has been observed in chalcogenide glasses and $HgSe$-$GeSe_2$ alloys but not in oxides.[27] In this work, we report the optical characterization of BZO after annealing in air. An increment of the absorption band in the UV-VIS region and an increment of both, single and Yb^{3+} pair emission is observed as the annealing temperature increases. To the best of our knowledge, this is the first report of thermodarkening effect in oxides, particular BZO perovskite. The aim of this work is to present the effect of annealing on the absorption, emission and fluorescence lifetime of Yb doped Barium Zirconate and to compare it with the photodarkening process.

2. Experimental Details

2.1 Synthesis of BaZrO$_3$

Microcrystalline Barium Zirconate doped with 0.5 mol% Yb^{3+} was synthesized by hydrothermal process. All reagents were analytical grade and used without further purification. Barium nitrate $Ba(NO_3)_3$, zirconyl chloride octahydrate $ZrOCl_8 \cdot 8H_2O$ and ytterbium nitrate $Yb(NO_3)_3 \cdot 5H_2O$ were used as the precursors materials. Sodium hydroxide (NaOH) was used as the precipitating agent. Cetyltrimethylammonium bromide (CTAB, $CH_3(CH_2)_{15}N(CH_3)_3Br$) was the surfactant and ethanol was the co-surfactant. In a typical preparation, barium nitrate, zirconyl chloride, ytterbium nitrate and CTAB (0.8 wt%) were dissolved in a solution of ethanol-water (20 vol% for ethanol) at room temperature applying vigorous stirring for 1 h. Under strong stirring, sodium

hydroxide was added and stirred again for 1 h at room temperature. The hydrothermal reactions were carried out in a stainless steel autoclave (Teflon jacketed with 250 ml of total capacity) under autogenous pressure at 100 °C for 24 h. The precipitate was then washed with distilled water and dried in a furnace at 100°C for 24 h.

2.2 Crystalline Structure and morphology

In order to investigate the crystalline structure of the sample, X-Ray Diffraction (XRD) was obtained with a SIEMENS D-500 diffractometer equipment provided with a Cu-K tube with α radiation at 1.5426 Å, scanning in the interval from 20° to 80° for 2θ with increments of 0.02° and swept time of 2 seconds. All observed peaks were indexed in correspondence with JCPDS 6-0399 standard for cubic phase. The morphology of nanocrystals was investigated by Scanning electron Microscopy (SEM) with a JEOL XL30 microscope.

2.3 Annealing Procedure

Under NIR excitation at 940 nm the $BaZrO_3$:Yb(0.5%) sample presents a very good NIR emission intensity as well as a strong visible CUC emission. In order to study the annealing temperature effect, this sample was annealed at 100 °C, 500 °C, 750 °C and 1000 °C in a furnace during 14 h, with a heating rate of 5°C /min. For each temperature a sample was taken out of the furnace and was cooled down to room temperature in air.

2.4 Optical characterization

In order to minimize the absorption of humidity, all optical measurements were carried out promptly within 1 h of the annealing process. The optical absorption spectra (reflectance mode) were measured with a Perkin-Elmer UV-VIS-NIR Lambda 900 spectrophotometer using a 1.5 in. integrating sphere (Labsphere Co). The measured wavelength ranged from 200 nm to 2000 nm. The emission spectra were obtained under 940 nm excitation with a 10 ns pulsed tunable Optical Parametric Oscillator (MOPO from Spectra Physics) pumped by the third harmonic of YAG:Nd pulsed laser. The fluorescence emission was analyzed with an Acton Pro 500i monochromator, a R955 Hamamatsu photomultiplier tube for visible emission and InGaAs photodetector for NIR emission connected to SR830 (Stanford Research Systems) mode-locking amplifier. The decay time curves were obtained using a Lecroy oscilloscope. All photoluminescence measurements were done at room temperature. The Infrared spectra (FTIR) of samples were recorded in the range 350–4000 cm^{-1} on a Perkin Elmer Spectrum BX System Spectrometer using the KBr pellet method.

3.- Results and discussions

3.1 Structural characterization

X-ray diffraction pattern of 0.5 mol% Yb^{3+} doped $BaZrO_3$ obtained after annealing at 1000°C is shown in Figure 1a. The main diffraction peaks are in agreement with JCPDS 6-0399 for pure cubic perovskite $BaZrO_3$ with a lattice constant of 4.18 Å. No changes were observed between XRD patterns for the sample annealed at 100 °C (not showed here) and that annealed at 1000 °C.

No phase segregation was observed, confirming the high structural stability of the cubic phase. SEM image of the sample annealed at 1000 °C is shown in Figure 1b. A well-defined micron sized BZO crystallites with cubic morphology is observed. Detailed analysis of each single cube indicates the presence of single crystals and crystals composed of several primary particles. This mixture suggests that the growth mechanism is based on the coalescence of individual nanocrystals. The average lateral side length of the particles is 1.5 μm.

Figure 2 shows the FTIR spectrum of Yb doped samples, the spectrum reveals an intense broadband centered around 544 cm^{-1} attributed to Zr-O vibration in the perovskite structure.[28, 29] This band presents a clear increase in absorption on increasing annealing temperature. This is due to the improvement of Zr-O bonding, leading to an enhancement of crystallinity in BZO host. The peaks at 858, 1060, 1437 and 3417 cm^{-1} is related to CO_3^{2-} groups,[28] stretching vibrations of C-O groups,[30] to OH deformation vibrations,[31] and to water and hydroxyl groups adsorbed on the surface of BZO, respectivelly.[28,32] These bands decrease as the annealing temperature increases indicating the reduction of undesired impurities.

3.2 Absorption spectra

The normalized absorption spectra for both, undoped and doped BaZrO:Yb^{3+}, powders annealed at 100 °C, 500 °C, 750 °C and 1000 °C, are shown in Figure 3. An increase in absorption in the UV-VIS range is clearly observed, suggesting the formation of defects such as color centers or oxygen vacancies. This indicates the presence of Thermodarkening. This effect is comparable to

the photodarkening observed in optical fibers as mentioned above.[15] Notice the shifting of the absorption peak to longer wavelengths (from 213 nm to 235 nm) as the annealing temperature increases (Figure 3a). Meanwhile, for doped samples a dramatic increase in absorption in the UV-VIS band and a decrease of the characteristic NIR absorption band of Yb^{3+} were observed, see Figure 3b. In this case, three main effects of Ytterbium are evident: 1) The introduction of Ytterbium gives rise to an splitting of the absorption band characteristic of the host forming 213 nm and 235 nm peaks, see Figure 3c. These peaks were only observed separately in undoped samples annealed at 100 °C and 1000 °C respectively, see Figure 3a. Since the 235 nm peak corresponds to the band gap of ZrO_2,[33] we could associate the 213 nm absorption peak as a contribution of the presence of Ba in the BZO crystalline structure. In this way, the annealing temperature in undoped samples enhances the Zirconium effect, whereas the contribution of the Ba in the host lattice decreases. Thus, the "shifting" of 213 nm peak means a decrease of this band. Probably, such shifting indicates the formation of $Ba^{2+} - O^{-2}$ bonds, considering that oxygen vacancies (V_O) are removed by the annealing process and that the 213 nm peak is associated with $Ba^{2+} - V_O$. For doped samples, the presence of such band suggests that V_O are not completely removed, perhaps because are forming F centers as a part of the charge compensation process. This will be explained later. 2) The presence of new absorption bands in the UV-VIS range of annealed doped samples (423 nm and 655 nm) in comparison with undoped samples. 3) The decrease of NIR absorption band of Yb^{3+}, see Figure 3d, and the change in color from white to yellow-brown in doped an undoped samples after annealing. These changes are the signature of the reduction of $Yb^{3+} \rightarrow Yb^{2+}$ ion and the formation of color

centers, respectively. Such reduction has been reported by others authors in Yb doped fibers, YAG and YAP crystals.[24,25]

3.3 The luminescence properties

The VIS and NIR emission spectra in Yb^{3+} doped samples for different annealing temperatures under 940 nm excitation wavelength for are shown in Figure 4. Annealing improved the crystalline structure and eliminated quenching centers to a good extent. As a result, both VIS and NIR emission were enhanced as is shown above in Figure 2. Characteristic emission of single Yb^{3+} ion centered at 973 nm and 1042 nm are associated with $^2F_{7/2} \rightarrow {}^2F_{5/2}$ transition, see Figure 4a. The emission lines located at 525 nm, 542 nm and 555 nm (Figure 4b) are characteristic of $^2H_{11/2} + {}^4S_{3/2} \rightarrow {}^4I_{15/2}$ transition and the 657 nm emission band is characteristic of $^4F_{9/2} \rightarrow {}^4I_{15/2}$ transition, both of Er^{3+} ion. These emissions bands are the result of the energy transfer from Yb^{3+} to Er^{3+} ion and are similar to the emission obtained in Y_2O_3:Yb,Er and ZrO_2:Yb,Er nanocrystals.[34, 35] In addition, peaks centered at 480 nm and 489 nm correspond to $^1G_4 \rightarrow {}^3H_6$ transition of Tm^{3+}, and result from the energy transfer from Yb^{3+} to Tm^{3+}. Since the presence of Tm^{3+} and Er^{3+} impurities was not detected in the absorption spectra it has to be very low concentration. The strong intensity of all peaks is interesting considering the very small concentration. This fact suggests very efficient upconversion processes involving traces of Tm^{3+} and Er^{3+} ions having the Yb^{3+} ions as sensitizers. The emission band centered at 504 nm is twice the energy of the normal luminescence of a single ion, suggesting that it is the result of the radiative relaxation of an excited Yb^{3+}-Yb^{3+} pair. Such emission band is named

cooperative emission and is described by the expression $^2F_{5/2} + {}^2F_{5/2} \rightarrow {}^2F_{7/2} + {}^2F_{7/2} + h\nu$. Figure 5 shows the dependence of the upconverted signal intensity (I_{UPC}) as a function of the pump power (I_{PUMP}). It is well-known that this dependence can be expressed by the equation $I_{UPC} = K I_{PUMP}^n$, where n denotes the number of photons absorbed to produce such upconverted emission and k is a constant. In the case of the sample annealed at 1000 °C, n~2, n~1.9 and n~1.7 for cooperative emission, green band and red band, respectively, confirming that such emission is the result of a two-photon process.

It is noticeable that the sample annealed at 100 °C does not present emission for both, VIS and NIR range. This could be because of the high content of quenching centers. The OH⁻ groups and residual H_2O, which are known to have a great influence on NIR and VIS emission, are present in BZO as is shown in Fig. 2.[32,36] Such impurities quench the fluorescence emission. When the annealing temperature increases, the residual impurities are reduced and the emission intensity increases. This reduction in quenching centers with temperature is expected to result in an increment of the fluorescence decay time in both, NIR and cooperative emission, as can be observed in Figure 6. The lifetime for CUC emission peak is nearly half of the lifetime characteristic of the infrared emission peak. As expected, such relation is the same for each annealing temperature, implying that CUC emission is produced by an Yb^{3+} pair, see Figure 6. The decay profiles corresponding to the emission peak at 504 nm (CUC emission) and NIR emission at 973 nm are shown in Figure 6a and 6b, respectively. In both cases, profiles are fitted by two exponential

functions. For low annealing temperature, decay time is dominated by fast decay component but for high annealing temperature, it is dominated by slow decay component. These results point out that fast decay component is associated with quenching or residual impurities centers. The lifetimes obtained by an exponential fitting of the experimental decay curves for CUC emission, range from $50\,\mu s$ to $320\,\mu s$ for 500 °C and 1000 °C, respectively. On the other hand, the obtained lifetime for 973 nm emission band, range from $80\,\mu s$ to $610\,\mu s$ for 500 °C and 1000 °C.

3.4 The presence of Yb^{2+} and Color Centers

Figure 7 shows the difference between doped and undoped BZO absorption spectra. Two broad bands are observed, 417 nm and 655 nm. The former is directly related to cooperative absorption, as this band is in agreement with the self-convolution of the NIR absorption spectra. Furthermore, this band increases with annealing temperature confirming the formation of Yb^{3+} ions pairs thereby improving the cooperative emission, see Figure 4b. According to literature, the 655 nm absorption band is characteristic of Yb^{2+} and is in agreement with the decrease of absorption band of single Yb^{3+} ion.[37, 38, 40] The emission of Yb^{2+} in different hosts has already been reported.[39-41] However, in our case, no fluorescence of the Yb^{2+} was observed after excitation at 655 nm. This can be explained as follows. Ahmed et al. reported that the introduction of Yb^{3+} ion in BZO host involves the substitution of Zr^{4+} at B-site positions, in consequence there is a charge compensation. Such compensation shares one electron from Yb^{3+} with oxygen vacancies (V_O) produced mainly by the synthesis process.[9] This leads to the formation of F color centers. The doped

sample annealed at 100 °C in Figure 3b presents a broad band in the region of 265-335 nm which corresponds to the superposition of F color centers (one or two electrons trapped in an oxygen vacancy) and Oxygen vacancies.[24] Such absorption bands increase with the annealing temperature. Since the annealing treatment is in an oxygen rich environment, oxygen enters the crystal structure reducing the Oxygen vacancies. Thus, it is reasonable to assume that the enhancement of the absorption band is produced by the formation of F color centers. The formation of these defects is confirmed by the change in color from white to yellow-brown in doped BZO. In opposite to results reported by Zeng et al. in which the air annealing after gamma irradiation destroys F color centers.[42] The increase in the absorption band in the UV-VIS region with the change from colorless to yellow on Yb^{2+} formation, has been observed in Yb doped silica performs.[43] In the present work, the change in color is associated with color centers formation.

M. Henke et al. reported the absorption bands peaking at 280 nm and 660 nm and were attributed to the absorption of Yb^{2+} in $Yb^{2+}:Y_3Al_5O_{12}$ crystal.[40] Xie et al. ascribed the 284 nm and 300 nm bands to Yb^{2+} absorption in $\alpha - SiAlON$.[44] Hence, the 265-335 nm absorption band which increases with annealing temperature can be considered as the superposition of Yb^{2+}, F color center and Oxygen vacancies. This behavior is in agreement with the decrease of the Yb^{3+} NIR absorption band (see Figure 4d) and suggest the formation of Yb^{2+}-F centers pairs. Such pairs formation inhibits the Yb^{2+} emission (traps for emitted photons). Several bands of F color centers accompanied by Yb^{2+} ions (Yb^{2+}-F pairs) has been reported in CaF_2 crystals.[26] In the case of undoped sample, a

broad band in the 274-327 nm region is observed. Again, this band is attributed to superposition of F color centers as well as oxygen vacancies, but the increment of the UV-VIS absorption band with annealing temperature is produced only by the F centers because there is no Yb^{3+}. This is confirmed by the change in color from white to yellow-brown for undoped samples. The $Yb^{3+} \rightarrow Yb^{2+}$ reduction to form isolated Yb^{2+} ions, as suggested by the 655 nm band, is promoted by the electrons captured from F centers formed during annealing in air. Finally, it is possible that Yb^{2+} replaces the Ba^{2+} position because the ionic radii is quite similar (1.28 nm for Yb^{2+} and 1.35 nm for Ba^{2+} in eightfold coordination). They also have similar charge. However, more studies are required to verify this hypothesis.

4. Conclusions

Yb doped BZO microcrystals were prepared by hydrothermal method at 100 ^{o}C and the luminescent properties were analyzed as a function of the annealing temperature. Annealing process play an important role in removing both oxygen vacancies and undesired impurities (OH, residual H_2O and C-O groups). For doped samples, F color centers were formed as a result of the combination of charge compensation and the presence of oxygen vacancies. In turn, these centers promote the reduction from Yb^{3+} to Yb^{2+}. The result is an increment in the UV-VIS absorption band for doped and undoped samples indicating the presence of the thermodarkening phenomena. The overall result is a remarkable increment of both, visible and NIR, luminescence emission. These results demonstrate that the decrease of quenching centers with annealing temperature is the dominant process regardless of the formation of F color

centers and the $Yb^{3+} \rightarrow Yb^{2+}$ reduction, that are detrimental for emission. However, the absence of Yb^{2+} emission confirms the formation of Yb^{2+}-F type color centers pairs that inhibit emission.

References

[1] T. Kushida, J. Phys. Soc. Jap. **34**, 1318 (1973).

[2] L.A Diaz-Torres, E. De la Rosa, P.Salas, H. Desirena, Opt. Mat. **27**, 1305 (2005).

[3] A. Kiryanov, Yuri Barmenkov, Itzel Martinez, Opt. Express **14**, 9 (2006).

[4] E. Montoya, O. Espeso, L.E. Bausá, J. Lumin. **87**, 1036 (2000).

[5] M. Malinowski, M.Kaczkan, R. Piramidowicz, Z. Frukacz, J. Sarnecki, J. lumin. **94-95**, 29 (2001).

[6] Y. Dong, G. Zhou, J. Xu, G. Zhao, F. Su, J. Crystal Growth **289**, 676 (2006).

[7] E. De la Rosa, P. Salas, L.A. Diaz-Torres, A. Angeles Chavez, J. Nanos. and Nanotech. **5**, 1480 (2005).

[8] P. G. Sundell, M. Bjorketun, and G. Wahnstrom, Phys. Rev. B **73**, 104 (2006).

[9] I. Ahmed, S.G. Eriksson, E. Ahlberg, C.S. Knee, H. Götlind, L.G. Johansson, M. Karlsson, A. Matic, L. Börjesson, Sol. Stat. Ionics **178**, 515 (2007).

[10] V.E. Henrick, P.A. Cox, The Surface Science of Metal Oxides, Cambridge University Press, New York, 1994.

[11] O. Auciello, J.F. Scott, R. Ramesh, Phys. Today **51**, 22 (1998).

[12] H. Zhang , X. Fu, S. Niu, Q. Xin, J. Lumin. *In Press* (2007).

[13] L. He, Y. Wang, H. Gao, J. Lumin. **126**, 182 (2007).

[14] Y. Dong, J. Xu, G. Zhou, G. Zhao, L. Su, X. Xu, H. Li, J. Si, Sol. State Commun. **141**, 105 (2007).

[15] J. J. Koponen, M. J. Söderlund, H. J. Hoffman, Opt. Express **14**, 11539 (2006)

[16] M. Broer, D. M. Krol, D. J. DiGiovanni, Opt. Lett. **18**, 799 (1993).

[17] G. R. Atkins, A. L. G. Carter, Opt. Lett. **19**, 1874 (1994).

[18] P. Laperle, A. Chandonnet, R. Vallée, Opt. Lett. **20**, 2484 (1995).

[19] M.M. Broer, R.L. Cone, J.R. Sompson, Opt. Lett. **16**, 1391 (1991).

[20] E.G. Behrens, R.C. Powell, J. Opt. Soc. Am. B **7**, 1437 (1990).

[21] L. B. Glebov, Glass Sci. Technol. **75**, C2 (2002).

[22 I. Manek-Hönninger, J. Boullet, Opt. Express **15**, 1606 (2007).

[23] Y. Huang, K. Jang, H. Jin, L. Zhao, J. Korean Phys. Soc. **49**, 227 (2006).

[24] Y. Dong, J. Xu, G. Zhou, G. Zhao, L. Su, X. Xu, H. Li, J. Si, X. Qian, X. Li, J. Shen, Phys. stat. sol. **203**, 2496 (2006)

[25] Y. Dong, G. Zhou, J. Xu, G. Zhao, F. Su, L. SU, H. Li, J. Si, X. Qian, X. Li, J. Shen, Opt. Mat. **28**, 1377 (2006).

[26] S. M Kaczmarek, T. Tsuboi, M. Ito, G. Boulon and G. Leniec, J. Phys. Condens. Matter **17**, 3771 (2005).

[27] V.V. Halyan, V.V. Bozhko, Semiconductor physics, quantum electronics and optoelectronics **6**, 73 (2003)

[28] F. Boschini, B. Robertz, A. Rulmont, R. Cloots, J. European Ceram. Soc. **23**, 3035 (2003).

[29] A. A. Athawale, A. J. Chandwadkar, P. Karandikar, R. Pasricha, M. S. Bapat, Rad. Phys. and Chem. **75**, 755 (2006).

[30] Georges Socrates, Infrared Characteristic Group Frequencies, Second Edition, Wiley and Sons (1998).

[31] R. B. Cervera, Y. Oyama, S. Yamaguchi, Sol. Stat. Ionics **178**, 569 (2007).

[32] H. P. Kumara, C. Vijayakumar, C. N. George, S. Solomon, R. Jose, J.K. Thomasa, J. Koshya, J. Alloys and Comp. *In Press* (2007).

[33] K.G. Kanade a, J.O. Baeg b, S.K. Apte c, T.L. Prakash c, B.B. Kale, Mat. Research Bull. **43**, 723 (2007).

[34] G. Boulon, V.Lupei, J. Lumin. **125**, 45 (2006).

[35] P. Salas, C. Angeles Chaves, J.A Montoya, E. De la Rosa, L.A. Diaz-Torres, H. Desirena, A. Martinez, M.A. Romero, J. Morales, Opt. Mat. **27**, 1295 (2004).

[36] G. Taglieri, M. Tersigni, P.L. Villa, C. Mondelli, Int. J. Inorganic mat. **1**, 103 (1999).

[37] X. Xu, Z. Zhao, G. Zhao, P. X. Song, J. Xu, P. Deng, J. Crystal Growth **257**, 297 (2003).

[38] D. Fagundes-Peters, N. Martynyuc, K. Lunstedt, V. Peters, J. Lumin. **125**, 238 (2007).

[39] S. Lizzo, E.P. Klein Nagelvoort, R. Erens, A. Meijerink, G. Blasse, J. phys. Chem. Solids **58**, 963 (1997).

[40] M. Nikl, A. Bensalah, E. Mihokova, J. Hybler, H. Sato, T. Fukuda, G. Boulon, Opt. Mat. **24**, 191 (2003)

[41] M. Henke, J. Perbon, S. KuK, J. Lumin. **87-89**, 1049 (2000).

[42] X. Zenga, X. Xu, X. Wang, Z. Zhao, G. Zhao, J. Xu, Spectrochimica Acta Part A **69**, 860 (2007).

[43] J. Kirchhof, S. Unger, A. Schwuchow, S. Grimm, V. Reichel, J. Non-Crystalline Solids **352**, 2399 (2006).

[44] R.J. Xie, N. Hirosaki, M. Mitomo, K. Uheda, T. Suehiro, X. Xu, Y. Yamamoto, J. Phys. Chem B **109**, 9490 (2005).

Figure caption
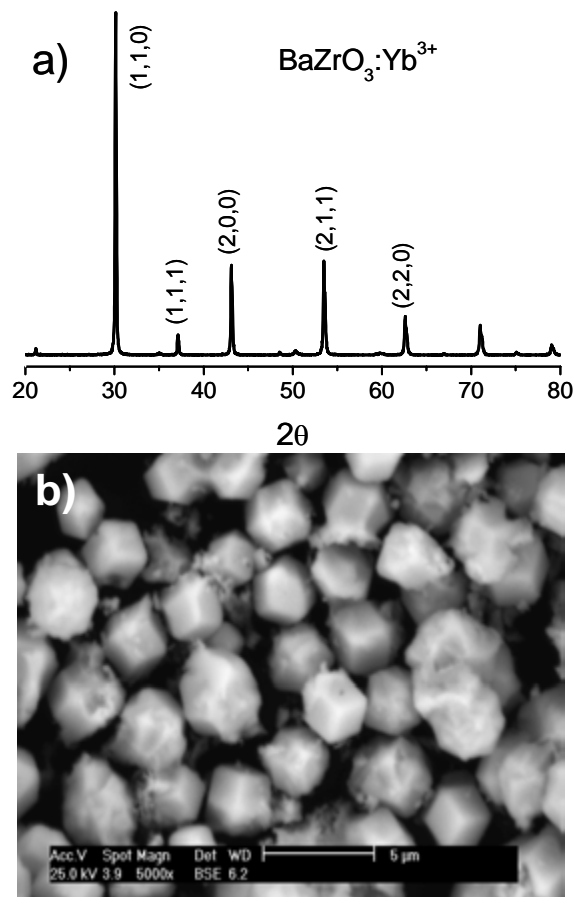
Figure 1. a) XRD pattern of $BaZrO_3:Yb^{3+}$ for 0.5 mol% dopant concentration annealed at 1000°C, b) SEM image of BZO microcrystals.
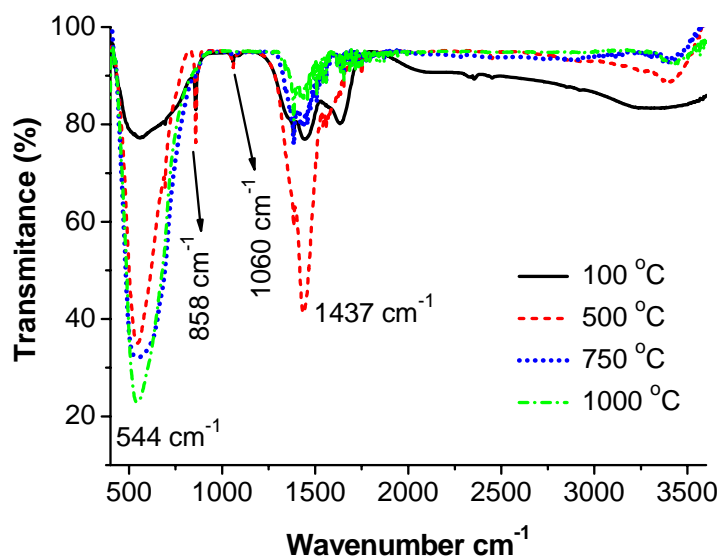
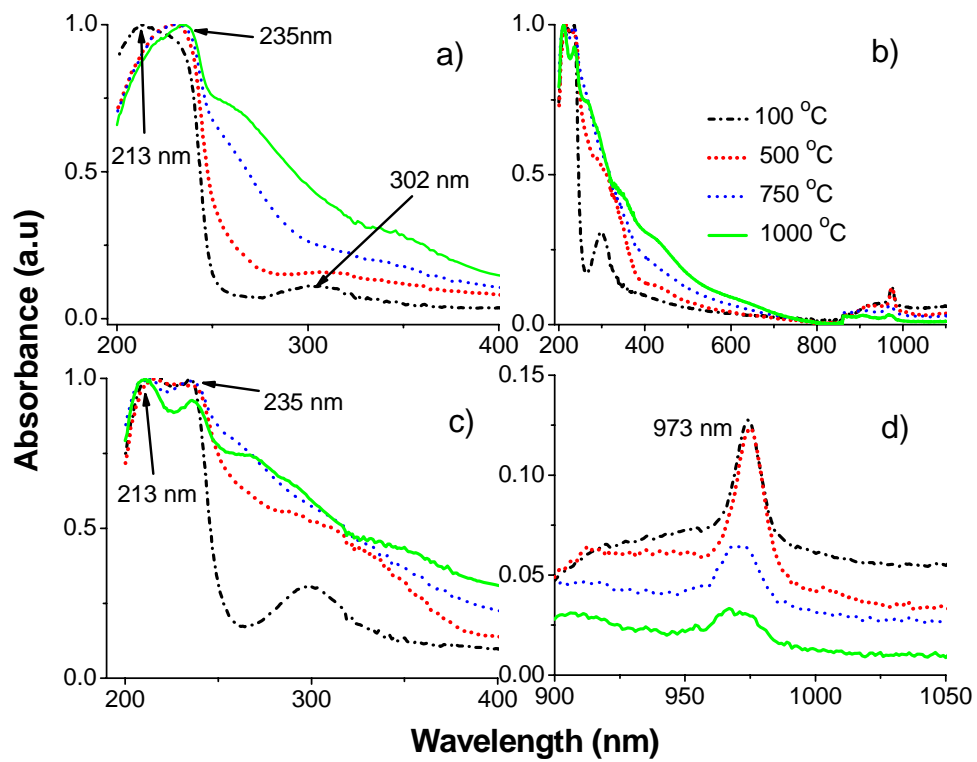Figure 2. FTIR spectra of $BaZrO_3:Yb$ at 0.5 mol% doped sample with different annealing temperatures.

Figure 3. Normalized absorption spectra of, a) undoped and b) doped BZO samples. c) and d) show an enlargement of (b) for the visible and NIR region, respectively.
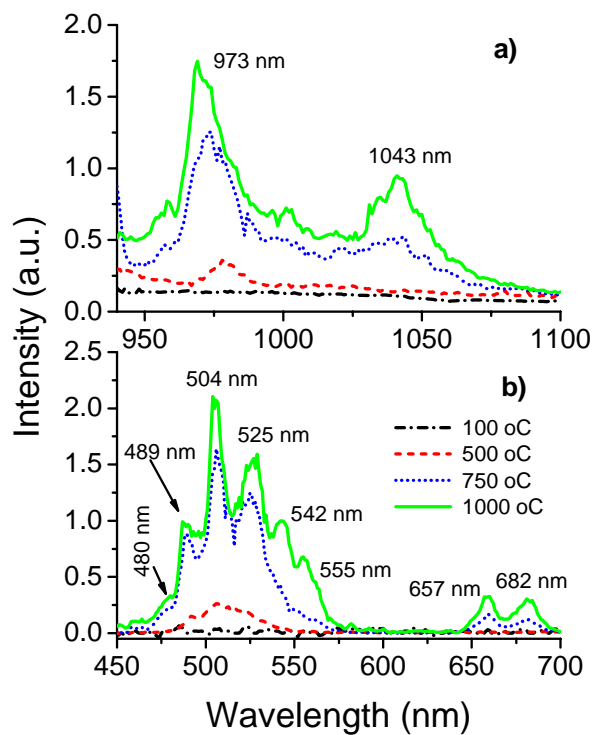
Figure 4. Emission spectra of $BaZrO_3:Yb^{3+}$, a) NIR emission and b) visible emission.
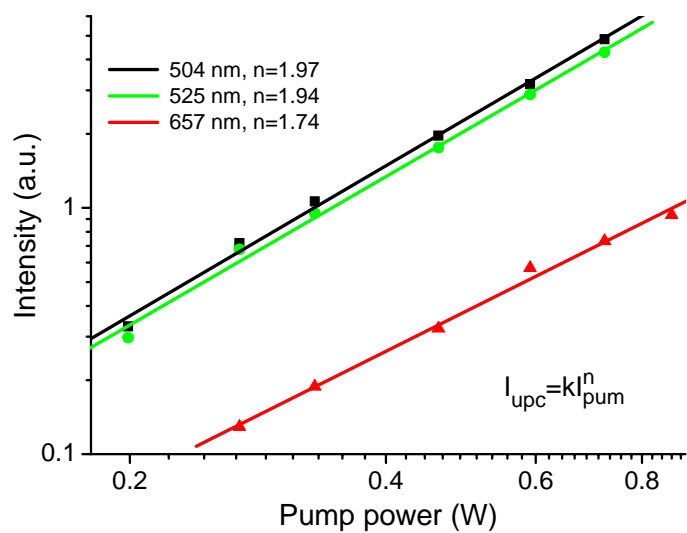
Figure 5. Dependence of the signal intensity, CUC, green and red emission as function of the pump power for sample annealed at 1000 °C.

Figure 6. Fluorescence decay profiles of, a) CUC emission peak at 504 nm and b) 973 nm emission peak for different annealing time.

Figure 7. Absorbance difference between normalized doped and undoped samples, and self-convolution of NIR absorption band of single Yb^{3+} ion.

Figure 1. a) XRD pattern of BaZrO$_3$:Yb^{3+} for 0.5 mol% dopant concentration annealed at 1000°C, b) SEM image of BZO microcrystals.

Figure 2. FTIR spectra of BaZrO$_3$:Yb at 0.5 mol% doped sample with different annealing temperatures.

Figure 3. Normalized absorption spectra of, a) undoped and b) doped BZO samples. c) and d) show an enlargement of (b) for the visible and NIR region, respectively.

Figure 4. Emission spectra of $BaZrO_3:Yb^{3+}$, a) NIR emission and b) visible emission.

Figure 5. Dependence of the signal intensity, CUC, green and red emission as function of the pump power for sample annealed at 1000 °C.
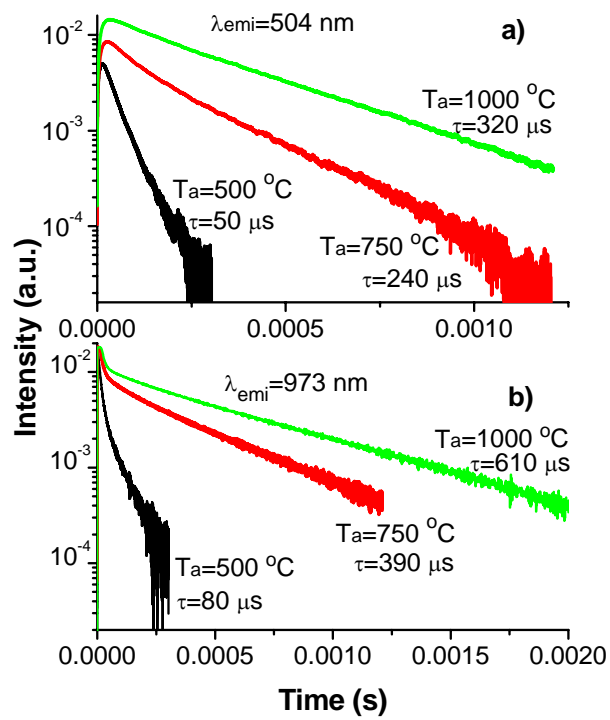
Figure 6. Fluorescence decay profiles of, a) CUC emission peak at 504 nm and b) 973 nm emission peak for different annealing time.
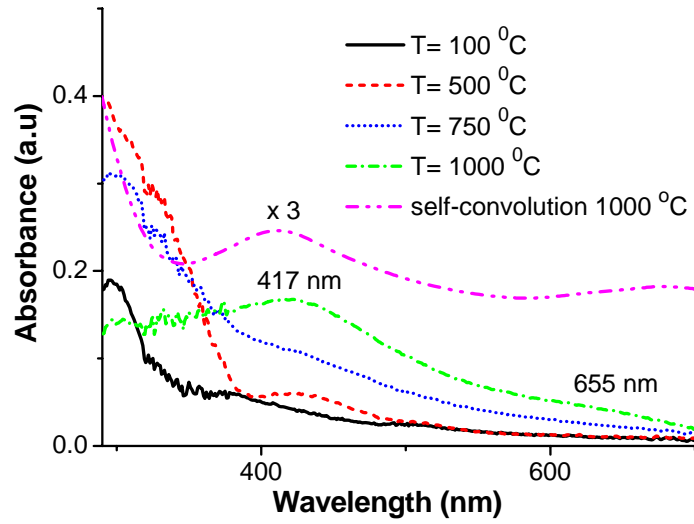
Figure 7. Absorbance difference between normalized doped and undoped samples, and self-convolution of NIR absorption band of single Yb^{3+} ion.

Appendix B

Green upconversion emission in sub micrometer phosphor BaZrO$_3$:Yb^{3+}

L.A. Diaz-Torres, J. Oliva, P. Salas, E. De la Rosa.